UNIVERSITY OF OKLAHOMA

GRADUATE COLLEGE

STUDY OF HOT CARRIER DYNAMICS AND RELAXATION IN METAL HALIDE PEROVSKITES

A DISSERTATION

SUBMITTED TO THE GRADUATE FACULTY

in partial fulfillment of the requirements for the

Degree of

DOCTOR OF PHILOSOPHY

By

SHASHI SOURABH
Norman, Oklahoma
2023

Downloaded from SHAREOK. Persistent Handle URL: https://hdl.handle.net/11244/337551

STUDY OF HOT CARRIER DYNAMICS AND RELAXATION IN METAL HALIDE PEROVSKITES

A DISSERTATION APPROVED FOR THE HOMER L. DODGE DEPARTMENT OF PHYSICS AND ASTRONOMY

BY THE COMMITTEE CONSISTING OF

Dr. Ian R. Sellers, Chair

Dr. Bin Wang

Dr. Bruce Mason

Dr. Kieran Mullen

Dr. Lloyd A. Bumm

© Copyright by SHASHI SOURABH 2023
All Rights Reserved.

To my family, this thesis is dedicated as a token of showing faith in me.

List of Publication

1. **S. Sourabh**, V. R. Whiteside, I. R. Sellers, M.C Beard, "Hot carrier redistribution, electron-phonon interaction, and their role in carrier relaxation in thin-film metal-halide perovskites", Physical Review M 5, 095402, 2021.

2. **S. Sourabh**, H. Afshari, V.R. Whiteside, G.E Eperon, R. A. Schiedt, M. C. Beard, J.M. Luther, I.R sellers, "Evidence of hot carrier extraction in metal halide perovskite solar cells, (Physical Review X, under review)".

3. **S. Sourabh**, V. Mopara, T. Creslyr, M. Furis, B. Saparov, I.R Sellers, "Dark exciton carrier dynamics and super long lived high energy states in $(EPEA)_2PbI_4$" (In preparation)

4. H. Afshari, **S. Sourabh**, S. Chacon, V. Whiteside, R. Penner, B. Rout, A. Kirmani, J. Luther, G. Eperon, I.R. Sellers, "FACsPb Triple Halide Perovskite Solar Cells with Thermal Operation over 200 °C", ACS Energy Lett. (2023).

5. H. Esmaielpour, V.R. Whiteside, **S. Sourabh**, G.E. Eperon, J.T. Pretch, M.C. Beard, H. lu, B.K. Durant, I.R. Sellers, "Role of Exciton Binding Energy on LO Phonon Broadening and Polaron Formation in $(BA)_2PbI_4$ Ruddlesden–Popper Films", Journal of Physical Chemistry C., 124, 9496 (2020).

6. B.K. Durant, H. Afshari, **S. Sourabh**, I.R. Sellers, "Radiation stability of mixed tin-lead halide perovskites: Implications for space applications. Solar

Energy Materials Solar Cells", 230, 111232 (2021).

7. H. Afshari, **S. Sourabh**, S. Chacon, V.R. Whiteside, R. Penner; B. Rout, A. Kirmani, J. Luther, G. Eperon, I.R. Sellers, "Proton radiation tolerance and self-healing of FACsPb Triple Halide Perovskite Solar Cells", (In preparation).

List of Presentation

This list includes the presentation talk and posters presented at various conferences.

1. **S. Sourabh**, H. Afshari, V. R. Whiteside, I. R. Sellers, "Evidence of Hot Carrier Extraction in Metal Halide Perovskite Solar Cells", SPIE Photonics West 2023, *Talk*, San Francisco, CA.

2. **S. Sourabh**, V. R. Whiteside, Y. Zhai, K. Wang, D. Y. Kim, M. C. Beard, and I. R. Sellers "Hot carrier redistribution, electron-phonon interaction, and their role in carrier relaxation in thin-film halide perovskites." SPIE Photonics West 2022, *Talk*, San Francisco, CA.

3. **S. Sourabh**, M. Sharma, V. R. Whiteside, H. Esmaeilpour, B. K. Durant, G. E. Eperon, M. C. Beard, and I. R. Sellers, "Carrier dynamics and carrier interaction in BA_2PbI_4 2D Ruddlesden popper thin film perovskite", *Talk*, APS March meeting 2021 (virtual).

4. **S. Sourabh**, H. Afshari, V. R. Whiteside, I. R. Sellers, "Evidence of Hot Carrier Extraction in Metal Halide Perovskite Solar Cells", Graduate Research Poster Session (GRPS), Homer L. Dodge Department of Physics and Astronomy, OU, Norman, *Poster*, 2022.

5. **S. Sourabh**, H. Afshari, V. R. Whiteside, I. R. Sellers, "Evidence of hot carrier effects in metal halide perovskite solar cells", *Poster*, OKPVRI-2022, Norman, 2022

6. **S. Sourabh**, H. Afshari, V. R. Whiteside, I. R. Sellers, "Evidence of hot carrier effects in metal halide perovskite solar cells", CQRT workshop/symposium, *Poster*, University of Oklahoma (OU), Norman, 2022.

Acknowledgements

During my time as a graduate student, I was incredibly fortunate to have had the support and guidance of an exceptional group of mentors, collaborators, and colleagues who have helped shape my academic and research journey. At the forefront of this group is Prof. Ian R. Sellers, who served as my advisor and provided invaluable direction and mentorship. I am immensely grateful for the countless conversations and feedback he offered, which have been pivotal in my growth as a researcher.

Dr. Vincent Whiteside has also played a crucial role in my research career, offering his expertise and skills to support the group and help me develop my own experimental expertise. His support and encouragement have been invaluable to me throughout my graduate studies.

I would also like to extend my gratitude to my committee members, Dr. K. Mullen, Dr. L. Bumm, Dr. B. Mason, and Dr. B. Wang, for their unwavering support, collaboration, and guidance throughout my graduate studies.

Working with the talented and collaborative members of Prof. Sellers' lab has been a highlight of my academic experience. I am especially grateful to Dr. Hamidreza Esmaielpour, who helped me get started with my Ph.D. and provided guidance during my initial years. Dr. Hadi Afshari has been a constant source of improvement, offering valuable feedback and discussion throughout my journey. I would also like to express my appreciation to Jugal Talukdar, Ajit Kumar, Dr. Geo Jose, Gaurav Nirala, Dr. Varun, Dr. Sumit, and all my friends who supported

me in any way during my Ph.D. journey. I am also grateful for the contributions and support from the undergraduate students who worked with me.

I am thankful for the fruitful collaborations I have had during my time at OU and beyond. I would like to express my appreciation to Dr. Bayram Saparov, Dr. Madalina Furis, and Dr. Joseph Tischler at OU, Dr. Matt Beard at NREL, and Dr. Giles Eperon at Swift Solar for their invaluable insights, feedback, and collaborations.

Lastly, I owe an immense debt of gratitude to my parents and my wife, who have been my unwavering pillars of support throughout my academic journey. Their love, encouragement, and faith in me have been a constant source of inspiration and motivation.

Thank you all for your contributions to my academic and research journey. I am deeply grateful for your support, and I could not have achieved this milestone without you.

Table of Contents

List of Publication iv

List of Presentation vi

List of Tables xii

List of Figures xvii

Abstract xviii

1 Introduction 1
- 1.1 Photovoltaics and Hot Carrier Solar Cells . . . 1
  - 1.1.1 Motivation . . . 1
  - 1.1.2 Energy Loss in Solar Cell . . . 3
  - 1.1.3 Hot Carrier Solar Cell . . . 7
- 1.2 Material System . . . 10
  - 1.2.1 Introduction . . . 10
  - 1.2.2 Material Structure . . . 12
- 1.3 References . . . 15

2 Experimental Methods and Setups 22
- 2.1 Introduction . . . 22
- 2.2 Current Density - Voltage Measurements . . . 22
- 2.3 Reflectance . . . 27
- 2.4 Absorption . . . 30
  - 2.4.1 Absorption: Theory . . . 30
  - 2.4.2 Absorption: Experimental setup . . . 33
  - 2.4.3 Photoluminescence . . . 35
  - 2.4.4 Photoluminescence Experimental Setup . . . 37
- 2.5 Ultrafast Transient Absorption . . . 39
- 2.6 References . . . 42

3 Hot Carrier Dynamics in Thin Film Metal Halide Perovskites 46
- 3.1 Introduction . . . 46
- 3.2 Temperature Dependent Photoluminescence . . . 48
- 3.3 Linewidth Analysis of Temperature Dependent Photoluminescence . . . 54
- 3.4 Transmission . . . 58
- 3.5 Conclusion . . . 64
- 3.6 References . . . 66

4 Ultrafast Transient Absorption: Thin film metal halide perovskites 74
- 4.1 Introduction . . . 74
- 4.2 Experimental Result and Discussion . . . 77
- 4.3 Conclusion . . . 90
- 4.4 References . . . 91

5 Evidence of Hot Carriers in Metal Halide Perovskite Solar Cells 96
5.1 Introduction 96
5.2 Result and Discussions 98
5.3 References 123

6 Dark Exciton Carrier Dynamics and Super Long Lived High Energy States in $(EPEA)_2PbI_4$ 131
6.1 Introduction 131
6.2 Experimental Results and Analysis 134
6.3 Discussion and Conclusion 146
6.4 References 149

7 Conclusion 155
7.1 Summary 155
7.2 Future Works 157

List of Tables

3.1 Extracted broadening parameters from the TDPL shown in Figure 3.1 for the following perovskites: 56

List of Figures

1.1 Silicon panels in the fields make up approximately 95% of installed solar power capacity. However, their efficiency is limited, typically ranging from 15% to 22% for commercial panels [6] 2
1.2 Schematic representation of a p-n junction illustrating key loss mechanisms: (1) transmission loss, (2) thermalization loss, (3) non-radiative recombination, and (4) radiative recombination. Adapted from: [9]. . . 4
1.3 Power conversion efficiency and various fundamental loss processes plotted as a function of the solar cell absorber bandgap. Adapted from: [11]. . . 6
1.4 (a) Time progression of hot carriers from generation to radiative recombination. Adapted from: [1]. 7
1.5 The schematic of a hot carrier solar cell, featuring a hot carrier absorber and energy selective contacts, is presented. Adapted from [21]. 9
1.6 Perovskite Structure: ABX_3; A: organic/inorganic cation, B: metal cation, X: halide anion. Adapted from: [45]. 12

2.1 Current density(J)-Voltage(V) characteristics of a perovskite solar cell with $FA_{0.8}Cs_{0.2}PbI_{2.4}Br_{0.6}Cl_{0.02}$ absorber layer, showing the critical parameters for a solar cell. 23
2.2 The normalized J-V characteristics for a $(FA_{0.8}Cs_{0.2})Pb(I_{2.4}Br_{0.6}Cl_{0.02})$ perovskite solar cell as a function of power, illustrating the presence of hot carriers at higher powers, as evidenced by changes in the J-V curve (see Chapter 5 for details). [11] 26
2.3 Schematic of a reflectivity measurement setup used to analyze the wavelength dependence of the bandstructure of a material or device, and/or the presence of stop bands in distributive Bragg reflectors (DBRs). . . . 28
2.4 (a) Reflectance (black) and photoluminescence (magenta) spectra of a material obtained using the reflectivity setup; (b) Schematic representation of a microcavity fabricated using SiO_2/Si_3N_4 Distributive Bragg reflectors as mirrors on both sides with $MAPbBr_3$ as the absorber material assessed by the author. 29
2.5 Schematic representation of Beer-Lambert Law depicting the absorption of incident light as it passes through a material [1]. 31
2.6 Absorption spectra of $FAPbBr_3$ (solid lines) and the fitted line using the Elliot fit absorption model (dotted lines) with a convoluted Voigt function. 32
2.7 Schematic diagram of the absorption setup used in the study. The custom-made setup broadly includes a light source, a sample holder, and a detection unit to measure the absorption of the sample. 34
2.8 Schematic illustration of the photoluminescence process in a semiconductor, from excitation to relaxation, as represented by a band diagram. The process involves the absorption of photons, followed by the creation of electron-hole pairs, which then relax to the band edge and recombine and emit light. 36
2.9 Schematic representation of the experimental arrangement for photoluminescence measurement. 38

2.10 (a) Schematic of the ultrafast transient absorption spectroscopy (TA) experiment is shown, which involves using a pump pulse to excite the sample and a probe pulse to study the carrier dynamics. (b) shows the time-dependent ultrafast transient absorption spectra of $(EPEA)_2PbI_4$ obtained using a 442 nm pump pulse from a Helios Ultrafast system. The observed kinetics of states or features in the TA spectra as time evolves provides critical information on the energy state dynamics of the sample. [3,4] 39

3.1 Temperature dependent PL from 4.2 to 295 K (color coded offset format) for (a) $FAMAPbSnI_3$, (b) $FAPbI_3$, (c) $FAMAPbI_3$, and (d) $FAPbBr_3$, respectively. Low-temperature features are labeled across all plots. . . . 49
3.2 (a) Full-Width at Half Maximum (FWHM) values between 4.2 K to 295 K for the four different perovskite thin films: (a) $FAPbBr_3$, (b) $FAMAPbI_3$, (c) $FAPbI_3$, and (d) $FAMAPbSnI_3$. The solid purple line represents the fit to the data, while the contributions of various coupling parameters described in Eq. (3.1) are shown in red for $\Gamma_0 + \Gamma_{LA}$, green for $\Gamma_0 + \Gamma_{LO}$, and blue for $\Gamma_0 + \Gamma_{imp.}$. 55
3.3 Comparison of peak PL energy gap (black circles) and energy from transmission spectra (red circles) for four perovskite thin films: $FAPbBr_3$, $FAMAPbI_3$, $FAPbI_3$, and $FAMAPbSnI_3$, from 4.2 to 295 K. Insets show PL (black) and absorbance (red) spectra at 4 K (upper) and 295 K (lower). 59

4.1 Typical Normalized TA spectra of $CH_3NH_3PbI_3$ excited with a 2.25 eV pump pulse. Inset: Cooling rates were determined using a global fit of the high-energy tail (between E = 1.7 and 1.85 eV) of each timeslice to a Boltzmann distribution.[2] 75
4.2 The transient absorption measurement of ΔA as a function of energy at room temperature for delay times ranging from 0.2/0.5 to 100 ps (color coded) for four types of perovskite thin films: (a) $FAMAPbSnI_3$, (b) $FAPbI_3$, (c) $FAMAPbI_3$, and (d) $FAPbBr_3$. [32] 77
4.3 Hot carrier extraction in PbSn sample. The high-energy tails of TA curves at different time delays are analyzed using equation 4.1 to determine the hot carrier temperature. 80
4.4 Variation of T_c with delay time at room temperature for three different perovskite thin films, namely $FAPbBr_3$ (black), $FAMAPbI_3$ (red), and $FAPbI_3$ (green). 81
4.5 Schematic of various phonon decay channels: (a), (b), and (c) have been reproduced from [33]. (a,b) showcases the decay of the LO phonon through the Klemens route into 2 LA phonons. (c) illustrates both the Ridley (TA+LO) and Klemens routes of the LO phonon decay channel. Additionally, (d) presents a schematic representation of the phonon bottleneck effect resulting from the low thermal conductivity in the perovskite proposed here. 83

4.6 (a) $FAMAPbSnI_3$ transient absorption spectra of ΔA as a function of energy at room temperature for delay times ranging from 2 to 50 ps. (b) Carrier density dependence of $FAMAPbSnI_3$ room temperature transient absorption spectra for a delay time of 2 ps. (c) Room temperature CW carrier density dependence for $FAMAPbSnI_3$. (d) Cooling rate curves for carrier densities of 2 and 32 $\times$ 10^{14} cm^{-2} for $FAMAPbSnI_3$. 85
4.7 Carrier cooling rate curves for carrier densities of 2 and 32 $\times$ 10^{14} cm^{-2} for $FAMAPbSnI_3$. 88

5.1 Schematic of the band offsets (left) and device structure (right) for the double cation/triple halide perovskite solar cell investigated in this work [55]. 98
5.2 Temperature-dependent J-V plots under 1 sun AM 1.5G illumination between 80 K and 300 K. At lower temperatures, a loss of FF is evident due to limited carrier extraction. 99
5.3 (a) Normalized waterfall plot of temperature dependent photoluminescence from 4 K to 295 K. (b) Comparison of the low power (1-sun AM 1.5G equivalent) monochromatic (532 nm excitation) current density – voltage responses at 100 K (purple), 200 K (green), and 295 K (gray) along with their respective (c) dark JVs (same color code). 100
5.4 (a) Arrhenius analysis and the (b) FWHM extracted from the temperature-dependent photoluminescence, and (c) a comparison of the temperature-dependent PL peak energy and the absorption edge observed in transmission spectroscopy used to determine the Stokes shift in these systems. The insets to (c) show the temperature-dependent emission and absorption at 4 K (upper inset) and 295 K (lower inset). 101
5.5 Monochromatic J-V plot from 4 K to 295 K, under 532 nm laser excitation at 1-sun AM 1.5G equivalence. The lower temperature shows s-shape behavior due to parasitic barriers existing at the heterojunction interfaces as also illustrated in Figure 5.3 (b). 104
5.6 The PD PL spectra at 100 K, 200 K and 295 K, labeled as (a), (b), and (c), respectively and a comparison between T_c (solid black squares) and the peak energy (open red circles) are presented in (d), (e), and (f) at same three temperatures, respectively. The shaded regions represent the region of equilibrium (yellow), non-equilibrium (red), and the regime in which decomposition begins to occur (gray). 105
5.7 (a) The EQE of the device, with increasing bandgap as a function of temperature. The trend do not show any indication of phase transition; (b) Power-dependent PL heat map, indicating a non-abrupt shift and the existence of two peaks (dotted line) after 50 suns, indicating possible phase segregation rather than phase transition. 109
5.8 Comparison of the temperature dependence of the peak PL energy with the shift in PL energy as a function of laser irradiance at the 100 K (open red circles) and 200 K (open green circles). 111

5.9 Power-dependent J-V curves at various temperatures (a) 100 K, (c) 200 K, and (e) 295 K under incident light intensities from 0.2 to 67-80 Suns. Corresponding Normalized J-V curves with respect to J_{sc} - in (b), (d), and (f), emphasizing J-V behavior changes with fluence. Ohmic like J-V characteristics across all 3 temperatures imply that the behavior is not merely due to lattice heating, as the differences between the heated system at $\sim$ 210 K (dotted line) and lattice-heated sample $\sim$ 210 K (cyan solid) indicated in (b). 113
5.10 Schematic of (a) Equilibrium (Teq, blue) and hot carrier (T_c, red) distributions excited at a power of 4700 mW/cm^2 ($\approx$ 47x suns) at 100 K with $T_c \approx$ 200 K. The parasitic barrier is depicted at V = 0 (solid) and V $<$ 0 (dashed). Thermionic emission is illustrated by a solid black arrow, and tunneling is represented by a dotted green arrow. (b) The same mechanisms are shown for T_{eq} = 200 K. 115
5.11 Comparison of peak energy and intensity from power-dependent PL (a-c) with V_{oc} and J_{sc} from power-dependent JV characteristics measurements (d-f) as a function of laser fluence. Regions corresponding to equilibrium (yellow), hot carrier (red), and phase segregation (grey) are highlighted, showcasing the variations in J_{sc}, V_{oc}, intensity, and peak energy in each region 119

6.1 Normalized waterfall plot showing (a) the temperature-dependent photoluminescence (PL) emission and (b) absorption spectra for different temperatures, with all the features labeled properly. Features A and B in the absorption spectrum correspond to super long-lived dark energy states, C corresponds to bandgap absorption, while the 'D' in the PL spectrum corresponds to excitonic emission, and E possibly indicates a defect state. 133
6.2 Peak intensity (open red circles) and peak energy (open black circles) extracted from temperature-dependent photoluminescence (PL) of the sample. The blue region corresponds to temperatures below 30 K, where the intensity decreases with increasing temperature due to the effect of a low-energy dark exciton. The red region corresponds to temperatures above 30 K, where thermal energy activates non-radiative channels that transfer charge to main excitonic state (radiative), which increases the integrated PL intensity. The white region corresponds to temperatures above 130 K, where the intensity decreases due to increasing electron-phonon coupling. 135
6.3 (a) Absorption (295 K) and PL spectra (4 K) are compared with the observed features (labeled) seen in TA shown in the lower panel (b). TA spectra (295 K) are presented for 11 ps and different powers (7 μW - 60 μW). 138

6.4 The proposed photophysical model effectively describes the results obtained from photoluminescence, absorption, and ultrafast TA measurements. The model includes both radiative (solid lines) and non-radiative pathways (dotted lines), with the activation of charge transfer confirmed by changes in the photoluminescence integrated intensity beyond a certain temperature. This model provides a comprehensive understanding of the photophysical behavior of the system under investigation. 140
6.5 Heat map of transient spectra at low power (7 μW) and high power (60 μW) along with their respective transient spectra at different delay times. 143
6.6 The absorption (295 K) and photoluminescence spectra for 4 K, which are used to compare with the observed effects in transient absorption shown in the lower panel. The transient absorption (TA) spectra are presented for 11 ps and different powers. 144
6.7 Peak fitting analysis using Gaussian distribution for the photoinduced absorption (PIA) of transient absorption (TA) spectra, recorded at 11 ps time under an irradiance of 60 μW (10^7 mW/cm^2). Y-axis is arbitrary positive ΔA. The fitting shows the presence of two distinct peaks at $\sim$ 533 nm (green)(LBE) and $\sim$ 538 nm (blue)(DE). The peak at 533 nm (LBE) is also detected in the photoluminescence (PL) spectrum. The PIA data suggests the existence of two closely spaced peaks. 145
6.8 Heat map (left) of the $(EPEA)_2PbI_4$ and the transient absorption spectra (right) at 11 ps, measured again after 6 months. 147

Abstract

Metal halide perovskites are a promising class of solution-based semiconductors with significant potential for optoelectronic devices, including hot carrier solar cells that are proposed to achieve higher efficiency than conventional solar cells. These materials possess high light absorption coefficients, long carrier diffusion lengths, and high defect tolerance, which leads to high power conversion efficiencies in solar cells. However, the intrinsic material instability of perovskite-based solar cells limits their performance. Understanding the carrier dynamics and stability of the material is critical to the development of solar cell physics, particularly in the case of hot carrier solar cells, as excited carriers with energy greater than the bandgap energy can potentially generate higher voltage and current than traditional solar cells. Unfortunately, these hot carriers also tend to rapidly lose their energy through carrier-phonon scattering, resulting in poor energy conversion.

Perovskites have shown significant potential for hot carrier solar cells in recent years due to their slow carrier cooling rate. However, a better understanding of carrier dynamics is critical for developing efficient perovskite-based solar cells. The effect of changing the different components of perovskite compounds was studied in a series of metal halide perovskites with varying optical properties using temperature-dependent photoluminescence, power-dependent photoluminescence, and ultrafast transient absorption techniques to investigate the carrier dynamics. The results suggest that the slow cooling of carriers in metal-halide

perovskites results from the intrinsic low thermal conductivity of all metal-halide perovskites. This finding indicates that the phonon energy, exciton binding energy, and interaction strength have little effect on the cooling of carriers. This study provides valuable insights into the fundamental understanding of carrier dynamics in perovskite-based solar cells, which can guide the development of more efficient and stable devices.

In addition we also studied the presence of hot carriers in a stable metal halide perovskite system under steady-state conditions. The results showed clear evidence of hot carriers in the device, but their behavior was strongly dependent on temperature and competition with photo-induced halide segregation. These findings provide valuable insights into the behavior of hot carriers in metal halide perovskite devices for the development of more efficient and stable hot carrier solar cells.

Finally, our study on the 2D Ruddlesden-Popper perovskite $(EPEA)_2PbI_4$ using temperature and power dependent photoluminescence and transient absorption spectroscopy showed the presence of multiple excitonic complexes and carrier redistribution mediated by power and/or temperature. Moreover, we observed extremely long-lived dark states in transient absorption, which play a significant role in the photoluminescence and absorption dynamics of $(EPEA)_2PbI_4$. These findings contribute to our understanding of perovskite material behavior and could aid in the development of more efficient optoelectronic devices.

Chapter 1

Introduction

1.1 Photovoltaics and Hot Carrier Solar Cells

1.1.1 Motivation

The demand for clean and green energy has never been higher as the world faces increasing concerns over climate change and the need to reduce dependence on finite fossil fuels. The development of clean and green energy sources is a crucial goal in the fight against climate change and the transition to a sustainable energy future. In order to meet this demand, the development of efficient and sustainable sources of renewable energy has become a critical priority. One of the most promising renewable energy sources is solar power, which has the potential to provide clean, abundant energy for generations to come. Solar energy, with its vast potential, will play a critical role in the energy demand of the future generation.

To realize this potential, it is essential to continue to improve the technology behind solar cells, the devices (Figure 1.1) that convert the sun's energy into usable electricity. In recent years, there has been a great deal of research into new and improved solar cell designs, including the use of new materials and advanced manufacturing techniques. One interesting concept in this field is the concept of hot carrier solar cells [2], which aims to increase the efficiency of solar cells by utilizing the hot carriers generated during photo-excitation [12]. This approach



Figure 1.1: Silicon panels in the fields make up approximately 95% of installed solar power capacity. However, their efficiency is limited, typically ranging from 15% to 22% for commercial panels [6]

seeks to overcome the limitations posed by the single-gap limit (Figure 1), which restricts the maximum theoretical efficiency of conventional solar cells to $< \sim$ 33 % [9], thus justifying the need for further advancements in solar cell technologies.

The ongoing research into the concept of hot carrier solar cells is an important part of this effort and requires a deep understanding of the fundamental physics behind the operation of such devices [15]. This includes understanding the dynamics of charge carrier generation and recombination, as well as the properties of materials and their interactions with light. By gaining a deeper understanding of these processes, the design and performance of hot carrier solar cells can be optimized, making them more efficient and cost-effective.

1.1.2 Energy Loss in Solar Cell

The functionality of a device is greatly dependent on its efficiency, and this is also applicable to solar cells, which are affected by several intrinsic energy loss mechanisms. A schematic representation of these mechanisms in a semiconductor is shown in Figure 1.2 [9]. The major loss channels can be broadly classified into two mechanisms. One of the dominant mechanisms is transmission loss (Process (1) in Figure 1.2), which occurs when low-energy photons are not absorbed by the system due to photon energy lower than the absorber's band gap.

The second dominant mechanism is thermalization (Process (2) in Figure 1.2), which occurs when high-energy photons are absorbed in the semiconductor, generating carriers with extra kinetic energy above the material's band gap. These hot carriers quickly lose their excess kinetic energy through interactions with phonons, resulting in their relaxation to the fundamental band edge of the absorber material.

An other common loss mechanism associated with a solar cell device is recombination loss, which can be further divided into two categories - non-radiative (Process (3) in Figure 1.2)) and radiative recombination (Process (4) in Figure 1.2)). Radiative recombination is a fundamental property of a material and is the reciprocal of the absorption process [8,9]. Energy loss in radiative recombination occurs through photon emission, while in non-radiative processes, energy loss occurs through carrier interaction with lattice-phonons. Both recombination

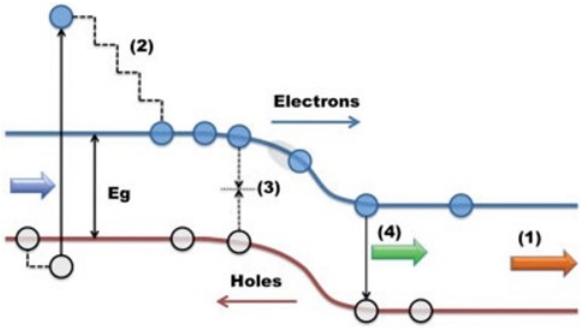


Figure 1.2: Schematic representation of a p-n junction illustrating key loss mechanisms: (1) transmission loss, (2) thermalization loss, (3) non-radiative recombination, and (4) radiative recombination. Adapted from: [9].

methods limit the current that can be extracted from the system, thus reducing the efficiency of a solar cell.

For a solar cell to be efficient, it also needs to absorb light very well as light absorption depends on photo-excited charge carrier generation. Generally, the absorption of light by a solar cell can be increased by employing a semiconductor with a lower band gap, however, this results in a higher degree of thermalization loss. On the other hand, if a wider band gap material is used in order to minimize the thermalization loss then that results in poor light absorption. Therefore, finding an appropriate balance between these opposing factors, according to the energy detailed balance principle, is crucial for optimizing the power conversion efficiency of a single-junction solar cell. The detailed balance principle says that in order to have a constant concentration of electrons in a steady state, the emission must match the absorption of photons [7].

Shockley and Queisser proposed a model in 1961 to determine the highest achievable power conversion efficiency for a single-junction solar cell [10]. The model suggests that all photogenerated carriers above the band gap of the solar cell relax down and occupy energy levels at the semiconductor's band edge in both the valence and conduction bands. This means the extracted energy is equal to the semiconductor band gap energy. By maximizing the extracted power, the conversion efficiency for a single junction solar cell (without concentration) can be optimized, with a maximum achievable efficiency of approximately 33% for an absorber with a band gap of 1.4 eV. This limit, derived from the energy detailed balance principle, is known as the Shockley-Queisser limit and serves as the upper limit for power conversion efficiency in a single-junction solar cell [10].

The more detailed contribution of loss channels in a solar cell are shown in Figure 1.3 [11]. The impact of different energy loss mechanisms in a solar cell can be evaluated over a range of band gap energies, as seen in Figure 1.3. These mechanisms are inherent to single-gap solar cells assuming the mismatch in their absorption and the solar spectrum, and are not affected by the quality of the material, operating conditions, or parasitic resistances in the system. The dark blue region in Figure 1.2 represents the area where usable power can be produced by a single-junction solar cell. The other colored regions, excluding blue, represent various loss mechanisms in the system. The two main losses occur due to the transmission of low-energy photons (shown in magenta) and thermalization

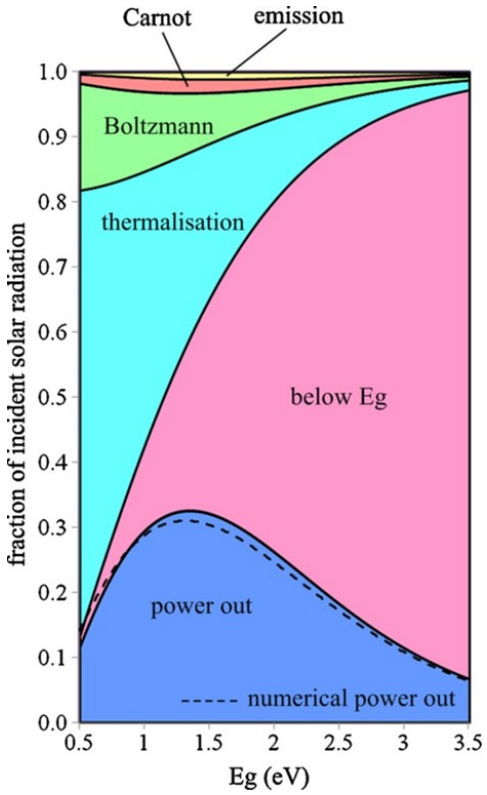


Figure 1.3: Power conversion efficiency and various fundamental loss processes plotted as a function of the solar cell absorber bandgap. Adapted from: [11].

(shown in cyan), which were discussed earlier. The Boltzmann loss, shown in green, occurs due to the mismatch between the light absorption and emission angle, which leads to an increase in entropy. However, this entropic loss can be reduced by concentrating light on the cell, thereby reducing its impact [11]. The Carnot loss is a thermodynamic limitation that restricts the amount of power conversion for engines operating between hot and cold reservoirs. The emission loss is discussed earlier and is related to energy loss through phonon or photon interaction.

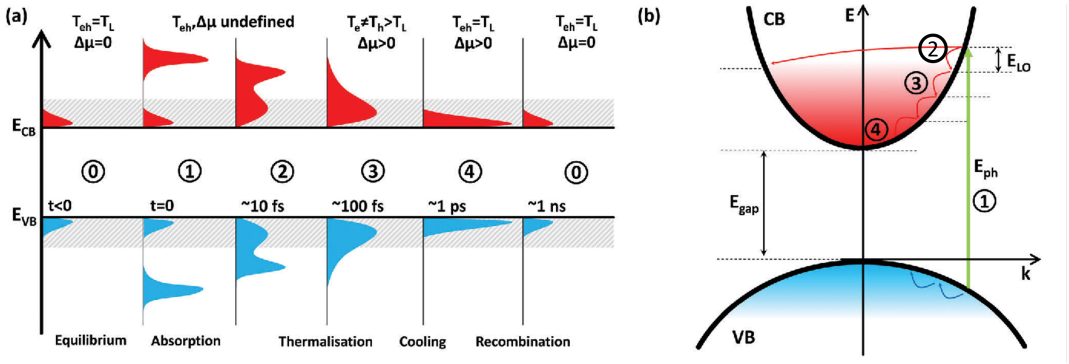


Figure 1.4: (a) Time progression of hot carriers from generation to radiative recombination. Adapted from: [1].

1.1.3 Hot Carrier Solar Cell

When a photon with energy above the band gap in a semiconductor is absorbed, it creates carriers with extra kinetic energy (above the band gap) referred to as hot carriers. Figure 1.4 illustrates the process of these hot carriers from generation to recombination (full thermalization). Figure 1.4 (a) shows the time progression of hot carriers, and Figure 1.4 (b) shows the corresponding process in the semiconductor band diagram picture. The process in both Figure 1.4 (a) and (b) are numbered chronologically. [1,8]

Before absorption (Region 0 in the figure), the electrons and holes are in equilibrium with the lattice; right after absorption (t = 0 s, Region 1), the photogenerated carriers occupy narrow energy levels. Within a sub-picosecond timescale carrier-carrier scattering occurs, and the photogenerated carriers redistribute their energy (Regions 2 and 3 in Figure 1.4). This elastic process results in the photogenerated carrier population achieving a global non-thermal

"hot carrier" distribution in the conduction and valence band, respectively, with a carrier temperature that is higher than the equilibrium temperature of the lattice, the so-called hot carrier regime. However, after a few picoseconds, the photogenerated "hot" carriers interact with phonons and dissipate energy via several processes [1], which thermalizes the system and reduces the carrier energy and temperature (Region 4 and 0 again). Finally, the thermalized electrons and holes recombine, and the system returns to its original equilibrium state. The loss of energy and heat generated during this process cannot be harnessed in a solar cell and contributes to a significant parasitic loss process.

Generally, with the increasing excitation power, the photoexcited carrier density increases. Under these conditions, a steady-state hot carrier distribution can be formed if the photo-excitation rate is higher than the cooling rate and lower than the carrier-scattering rate [13]. This results in an increase in the density of photogenerated hot carriers and a decrease in the efficiency of electron-phonon interactions, creating a 'phonon bottleneck' effect [13,14]. However, to effectively enhance power conversion efficiency, it is crucial to extract the photogenerated hot carriers on an ultrafast timescale before they dissipate their excess kinetic energy via electron-phonon interactions [15-18].

The idea of hot carrier solar cells was first proposed by Ross and Nozik in 1982 [12]. However, despite their suggestion over three decades ago, there have been no practical demonstrations of such solar cells to date. The two main challenges in

this context that needs to be overcome are: 1) designing a hot carrier absorber that significantly inhibits hot carrier thermalization and 2) adiabatically extracting hot carriers before thermalization.

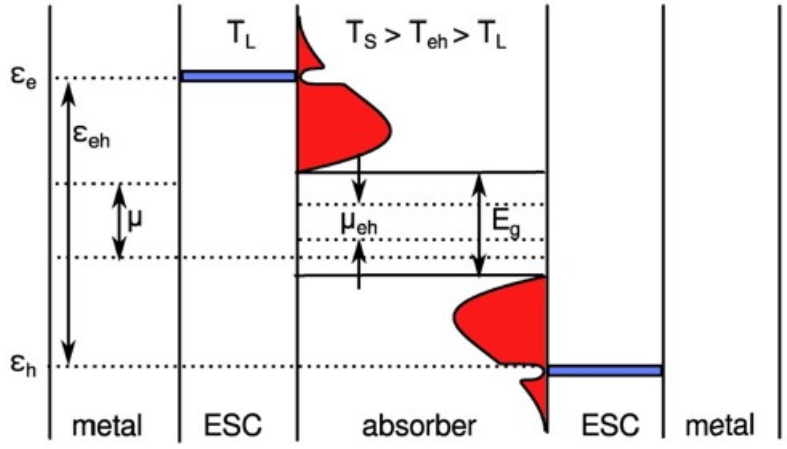


Figure 1.5: The schematic of a hot carrier solar cell, featuring a hot carrier absorber and energy selective contacts, is presented. Adapted from [21].

The design for a proposed hot carrier solar cell is shown in Figure 1.5 [21]. It has two main parts: (1) the hot carrier absorber, which creates a stable number of hot carriers by minimizing the interaction of carriers with phonons [19] and (2) the energy-selective contacts, which are used to extract either electrons or holes adiabatically from the hot carrier population in absorber layer [20]. These contacts are carefully made so that hot carriers-phonon interaction is minimized, which helps keep the non-equilibrium carriers hot [15,16,21].

The hot carriers are extracted through special/selective contacts that allow

only a narrow range of energy to pass. This process converts the hot carriers' extra energy into potential energy. Both electrons and holes are taken out, and the difference in their energy levels determines the amount of energy that is extracted, which is higher than the energy gap in the absorber. The final output voltage for these solar cells can be calculated using an equation [21,22]:

$$qV = (1 - \frac{T_L}{T_{eh}})E_{eh} + \Delta\mu(\frac{T_L}{T_{eh}}) \tag{1.1}$$

Where T_L, T_{eh}, E_{eh}, and $\Delta\mu$ represent the lattice temperature, carrier temperature, extraction energy, and quasi-Fermi level splitting, respectively.

1.2 Material System

1.2.1 Introduction

The unique optoelectronic properties of perovskite semiconductors, including their high absorption coefficient, strong photoluminescence, long carrier diffusion lengths, and high carrier mobility, make them attractive for various applications [3-5]. Metal halide perovskites are an especially interesting class of semiconductors with the potential to revolutionize the optoelectronic semiconductor industry, motivating research into their use for photovoltaic applications [46]. Before delving into the structural properties of this material, it is worth briefly revisiting the history of perovskites.

Perovskites, a group of materials with a chemical formula of ABX_3, have gained significant attention in the scientific community due to their remarkable properties. Gustave Rose, a German mineralogist, first discovered the mineral

structure of calcium titanium oxide in 1839, and it was later characterized by the Russian mineralogist Lev A. Perovski, who was the first to report its crystalline structure. This structure is what gave the material its name and led to the development of the perovskite family.

Metal-oxide perovskites (X=O) were the first to be studied due to their unique ferroelectric and magnetic properties, as well as their potential to be used as superconductive materials [23]. However, interest in metal halide perovskites (X=Halide) has risen in recent years. The first hybrid metal-halide perovskite structure was published in 1884, based on gold and chloride [24]. In 1958, Møller reported the first lead-halide based perovskite, investigating the photoconductive properties of CsPbX3 perovskite [25]. The first hybrid organic-inorganic lead-halide perovskite structure was published in 1978 by Weber and Naturforsch [26]. These advancements have paved the way for further research into metal halide perovskites and their potential applications in various fields.

At the end of the 20th century, perovskites were employed in electronic devices as semiconductors. Kagan and Mitzi demonstrated the possibility of using layered organic-inorganic halide perovskites as the active phase in thin film transistors and light-emitting diodes [27-29]. The photovoltaic (PV) application of hybrid perovskites began in 2006 when Miyasaka and coworkers employed methylammonium lead bromide as a sensitizer in a liquid electrolyte-based dye-sensitized solar cell architecture, achieving a power conversion efficiency (PCE)

of 2.2% [30]. Over the next few years, perovskite-based solar cells saw rapid improvements in efficiency and device stability. The combination of high charge carrier mobility, large spectrally tunable absorption coefficient, low-cost solution-process deposition, and strong defect tolerance is what makes the metal-halide perovskites a promising candidate for a new affordable photovoltaic technology.

1.2.2 Material Structure

This section offers a concise overview of the key structural properties of hybrid lead-halide perovskite crystals, sufficient for understanding their structure. The A site in the hybrid perovskite crystal is filled by an organic cation, with methylammonium (MA) being the most commonly used in photovoltaics, but formamidinium (FA) has also been utilized. Mixing the two cations in different ratios is also proposed to tune the bandgap and enhance low-energy solar spectrum absorption [32-34]. Cs is the most prevalent inorganic cation employed, as its small

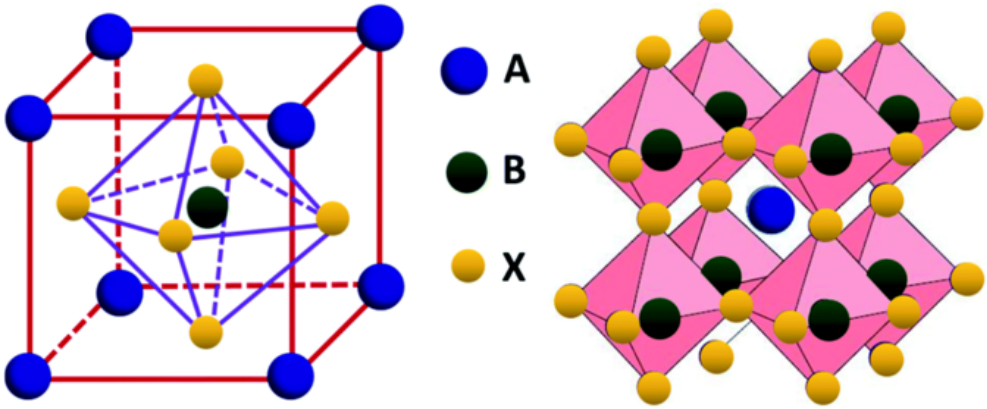


Figure 1.6: Perovskite Structure: ABX_3; A: organic/inorganic cation, B: metal cation, X: halide anion. Adapted from: [45].

size and lack of intrinsic dipole moment make it ideal for studying the impact of the A cation [31] on the material's overall optoelectronic properties. The use of Cs and FA together is also a recent trend. Figure 1.6 shows the chemical structure of a perovskite. The B site is filled by a divalent metal cation from group IVA (Pb^{2+}, Sn^{2+}, Ge^{2+}). In this thesis, we will mostly focus on the lead-based hybrid perovskite with few exceptions, as lead has proven to be superior in performance and stability compared to tin and germanium.

The X site is occupied by a halide anion. The halide anion is considered to be the most effective component for modifying the optical and electronic properties of perovskite material. The exchange of halide anion from I→Br→Cl, and its effect on the perovskite's absorption and emission properties, are briefly discussed below.

The bandgap of metal halide perovskites (MHPs) varies with the size of the halide ion [18]. Since the ionic radius follows the order I>Br>Cl, iodine-based MHPs possess the smallest bandgap, followed by those based on bromine and chlorine. Iodine-based perovskite solar cells exhibit the highest efficiency among halide perovskites, primarily attributed to their lower bandgap. However, their moisture sensitivity negatively impacts the devices' long-term stability [35-41].

Conversely, mixing bromine with iodine can produce perovskite solar cells with tunable bandgaps, enabling precise control over the material's bandgap [43] and enhanced long-term stability [44] due to reduced moisture sensitivity.

Bromine-based perovskites have a higher bandgap and are not optimized for photovoltaic applications on their own.

Cl-based MHPs possess an even higher bandgap, making them unsuitable for standalone photovoltaic applications. However, incorporating small amounts of chlorine into iodine-based perovskites can improve carrier diffusion length, photoluminescence lifetime, and device stability without affecting the bandgap [42].

Alternatively, combining all three halides may result in mixed-halide perovskites with potentially improved performance and stability. However, the precise mixture and proportions of these halides must be precisely controlled to attain the desired enhancements in long-term stability and bandgap tunability. Chapter 5 explores the photovoltaic properties of a solar cell device based on mixed halide composition.

1.3 References

1. S. Kahmann, M. A. Loi, "Hot carrier solar cells and the potential of perovskites for breaking the Shockley–Queisser limit", J. Mater. Chem. C, vol. 7, pp. 2471-2486, 2019. https://doi.org/10.1039/c8tc04641g.

2. K. F. David, R. W. Vincent, R. S. Ian, "Pathways to hot carrier solar cells", J. Photonics for Energy, vol. 12, no. 2, 022204, 2022.

3. J. G. Feng , C. Gong , H. F. Gao , W. Wen , Y. J. Gong , X. Y. Jiang , B. Zhang , Y. C. Wu , Y. S. Wu , H. B. Fu , L. Jiang and X. Zhang , Nat. Electron., 2018, 1 , 404 —410.

4. F. R. Cao , L. X. Meng , M. Wang , W. Tian and L. Li , Adv. Mater., 2019, 31 , 7.

5. W. A. S. Weibin Chu , J. Zhao and O. V. Prezhdo , Angew. Chem., Int. Ed., 2020, 132 , 6497 —6503.

6. R. F. Service, "To amp up solar cells, scientists ditch silicon: New perovskite tandem cell promises to be cheaper than conventional ones, and almost as efficient", Science, 2019. https://doi.org/10.1126/science.aax7477.

7. J. Nelson, "The Physics of Solar Cells", World Scientific Publishing Company, 2003.

8. M. A. Green, "Third generation photovoltaics: advanced solar energy conversion", Physics Today, vol. 57, no. 12, pp. 71-72, 2004.

9. G. F. Brown, J. Wu, "Third generation photovoltaics", Laser Photonics Reviews, vol. 3, no. 4, pp. 394-405, 2009.

10. W. Shockley, H. J. Queisser, "Detailed balance limit of efficiency of p- n junction solar cells", Journal of Applied Physics, vol. 32, no. 3, pp. 510-519, 1961.

11. L. C. Hirst, N. J. Ekins-Daukes, "Fundamental losses in solar cells", Progress in Photovoltaics: Research and Applications, vol. 19, no. 3, pp. 286-293, 2011.

12. R. T. Ross, A. J. Nozik, "Efficiency of hot-carrier solar energy converters", Journal of Applied Physics, vol. 53, no. 5, pp. 3813-3818, 1982.

13. A. J. Nozik, G. Conibeer, M. C. Beard (Eds.), "Advanced Concepts in Photovoltaics", Royal Society of Chemistry, 2014.

14. A. Le Bris, "Feasibility study of a hot carrier photovoltaic device", PhD dissertation, Ecole Centrale Paris, 2011.

15. G. Conibeer, N. Ekins-Daukes, J.-F. Guillemoles, D. Kőnig, E.-C. Cho, C.-W. Jiang, S. Shrestha, M. Green, "Progress on hot carrier cells", Solar Energy Materials and Solar Cells, vol. 93, no. 6-7, pp. 713-719, 2009.

16. A. Le Bris, L. Lombez, S. Laribi, G. Boissier, P. Christol, J.-F. Guillemoles, "Thermalisation rate study of GaSb-based heterostructures by continuous wave photoluminescence and their potential as hot carrier solar cell ab-

sorbers", Energy Environmental Science, vol. 5, no. 3, pp. 6225-6232, 2012.

17. H. Esmaielpour, V. R. Whiteside, H. P. Piyathilaka, S. Vijeyaragunathan, B. Wang, E. Adcock-Smith, K. P. Roberts et al., "Enhanced hot electron lifetimes in quantum wells with inhibited phonon coupling", Scientific Reports, vol. 8, no. 1, 12473, 2018.

18. H. Esmaielpour, V. R. Whiteside, J. Tang, S. Vijeyaragunathan, T. D. Mishima, S. Cairns, M. B. Santos, B. Wang, I. R. Sellers, "Suppression of phonon-mediated hot carrier relaxation in type-II InAs/AlAsxSb1-x quantum wells: a practical route to hot carrier solar cells", Progress in Photovoltaics: Research and Applications, vol. 24, no. 5, pp. 591-599, 2016.

19. G. Conibeer, S. Shrestha, S. Huang, R. Patterson, H. Xia, Y. Feng, P. Zhang et al., "Hot carrier solar cell absorber prerequisites and 33 candidate material systems", Solar Energy Materials and Solar Cells, vol. 135, pp. 124-129, 2015.

20. G. J. Conibeer, C-W. Jiang, D. König, S. Shrestha, T. Walsh, M. A. Green, "Selective energy contacts for hot carrier solar cells", Thin Solid Films, vol. 516, no. 20, pp. 6968-6973, 2008.

21. L. C. Hirst, H. Fujii, Y. Wang, M. Sugiyama, N. J. Ekins-Daukes, "Hot carriers in quantum wells for photovoltaic efficiency enhancement", IEEE Journal of Photovoltaics, vol. 4, no. 1, pp. 244-252, 2014.

22. P. Würfel, A. S. Brown, T. E. Humphrey, M. A. Green, "Particle conservation in the hot-carrier solar cell", Progress in Photovoltaics: Research and Applications, vol. 13, no. 4, pp. 277-285, 2005.

23. M. a. Peña and J. L G Fierro. Chemical structures and performance of perovskite oxides. Chemical Reviews, 101(7):1981–2017, 2001.

24. H. Topsøe, A. Arzruni, and G. Bath. XVI.Auszüge. Zeitschrift für Kristallographie – Crystalline Materials, 8(1-6):246–320, nov 1884.

25. Chr. Kn. Møller. Crystal Structure and Photoconductivity of Caesium Plumbohalides. Nature, 182(4647):1436, nov 1958.

26. D. Weber. CH3NH3PbX3, a Pb(II)-System with Cubic Perovskite Structure. Zeitschrift für Naturforschung, 33b(August 1978):1443–1445, 1978.

27. D. B. Mitzi. Synthesis, Structure, and Properties of Organic-Inorganic Perovskites and Related Materials, pages 1–121. John Wiley & Sons, Inc., 2007.

28. C. R. Kagan. Organic-Inorganic Hybrid Materials as Semiconducting Channels in Thin-Film Field-Effect Transistors. Science, 286(5441):945–947, oct 1999.

29. K. Chondroudis, D. B. Mitzi, "Electroluminescence from an Organic-Inorganic Perovskite Incorporating a Quaterthiophene Dye within Lead Halide Perovskite Layers", Chemistry of Materials, vol. 11, no. 11, pp. 3028-3030, Nov 1999.

30. A. Kojima, K. Teshima, T. Miyasaka, Y. Shirai, "Under the spotlight: The organic–inorganic hybrid halide perovskite for optoelectronic applications", Proceedings 210th ECS Meeting, 2006.

31. Q. Chen, N. De Marco, Y. (Michael) Yang, T.-B. Song, C.-C. Chen, H. Zhao, Z. Hong, H. Zhou, Y. Yang, "Under the spotlight: The organic–inorganic hybrid halide perovskite for optoelectronic applications", Nano Today, vol. 10, no. 3, pp. 355–396, 2015.

32. S. Pang, H. Hu, J. Zhang, S. Lv, Y. Yu, F. Wei, T. Qin, H. Xu, Z. Liu, G. Cui, "NH2CH=NH2PbI3: An alternative organolead iodide perovskite sensitizer for mesoscopic solar cells", Chemistry of Materials, vol. 26, no. 3, pp. 1485-1491, 2014.

33. G. E. Eperon, S. D. Stranks, C. Menelaou, M. B. Johnston, L. M. Herz, H. J. Snaith, "Formamidinium lead trihalide: a broadly tunable perovskite for efficient planar heterojunction solar cells", Energy Environmental Science, vol. 7, no. 3, pp. 982, 2014.

34. J.-W. Lee, D.-J. Seol, A.-N. Cho, N.-G. Park, "High-Efficiency Perovskite Solar Cells Based on the Black Polymorph of HC(NH2)2PbI3", Advanced Materials, vol. 26, no. 29, pp. 4991-4998, 2014.

35. K. K. Bass, R. E. McAnally, S. Zhou, P. I. Djurovich, M. E. Thompson, B. C. Melot, "Influence of moisture on the preparation, crystal structure, and photophysical properties of organohalide perovskites", Chem. Commun.,

vol. 50, no. 99, pp. 15819-15822, 2014.

36. G. E. Eperon, S. N. Habisreutinger, T. Leijtens, B. J. Bruijnaers, J. J. van Franeker, D. W. DeQuilettes, S. Pathak, R. J. Sutton, G. Grancini, D. S. Ginger, R. A. J. Janssen, A. Petrozza, H. J. Snaith, "The Importance of Moisture in Hybrid Lead Halide Perovskite Thin Film Fabrication", ACS Nano, vol. 9, no. 9, pp. 9380-9393, Sep. 2015.

37. G. Grancini, V. D'Innocenzo, E. R. Dohner, N. Martino, A. R. Srimath Kandada, E. Mosconi, F. De Angelis, H. I. Karunadasa, E. T. Hoke, A. Petrozza, "CH3NH3PbI3 Perovskite Single Crystals: Surface Photophysics and its Interaction with the Environment", Chem. Sci., vol. 6, pp. 1-6, 2015.

38. S. Stranks, H. J. Snaith, "Metal-halide perovskites for photovoltaic and light-emitting devices", Nature Nanotechnology, vol. 10, no. 5, pp. 391-402, 2015.

39. T. Leijtens, G. E. Eperon, N. K. Noel, S. N. Habisreutinger, A. Petrozza, H. J. Snaith, "Stability of Metal Halide Perovskite Solar Cells", Advanced Energy Materials, 2015.

40. H. Gao, C. Bao, F. Li, T. Yu, J. Yang, W. Zhu, X. Zhou, G. Fu, Z. Zou, "Nucleation and Crystal Growth of Organic-Inorganic Lead Halide Perovskites under Different Relative Humidity", ACS Applied Materials & Interfaces, vol. 7, no. 17, pp. 9110-9117, 2015.

41. S. D. Stranks, P. K. Nayak, W. Zhang, T. Stergiopoulos, H. J. Snaith, "Formation of Thin Films of Organic-Inorganic Perovskites for High-Efficiency Solar Cells", Angewandte Chemie International Edition, 2015.

42. P. Docampo, F. Hanusch, S. D. Stranks, M. Döblinger, J. M. Feckl, M. Ehrensperger, N. K. Minar, M. B. Johnston, H. J. Snaith, T. Bein, "Solution Deposition-Conversion for Planar Heterojunction Mixed Halide Perovskite Solar Cells", Advanced Energy Materials, vol. 4, no. 14, pp. 1-6, May 2014.

43. E. Mosconi, A. Amat, Md. K. Nazeeruddin, M. Grätzel, F. De Angelis, "First-Principles Modeling of Mixed Halide Organometal Perovskites for Photovoltaic Applications", The Journal of Physical Chemistry C, vol. 117, no. 27, pp. 13902-13913, Jul. 2013.

44. J. H. Noh, S. H. Im, J. H. Heo, T. N. Mandal, S. I. Seok, "Chemical management for colorful, efficient, and stable inorganic-organic hybrid nanostructured solar cells", Nano Letters, vol. 13, no. 4, pp. 1764-1769, Apr. 2013.

45. Z. Yi, et al., "Will organic–inorganic hybrid halide lead perovskites be eliminated from optoelectronic applications?", Nanoscale Advances, vol. 1, no. 4, pp. 1276-1289, 2019.

46. W. Zhang, G. E. Eperon, and H. J. Snaith, "Metal halide perovskites for energy applications", Nat Energy, vol. 1, pp. 16048, 2016.

Chapter 2

Experimental Methods and Setups

2.1 Introduction

In this chapter, the methods and characterization techniques utilized in our study are presented, with a focus on investigating the dynamics of materials and devices for solar cell applications. The electrical characterization approaches, which involved current density-voltage (J-V) measurements, are also detailed. Subsequently, we provide a comprehensive overview of our custom-built optical characterization setup, which was utilized for photoluminescence, absorption, and reflectance spectroscopy measurements. The working principle of this setup is also outlined. Finally, the setup utilized for Ultrafast transient spectroscopy, which was employed to investigate carrier dynamics in metal halide perovskites is discussed in detail.

2.2 Current Density - Voltage Measurements

Solar cells are devices that convert sunlight into electricity. The efficiency of a solar cell (η) is a key factor in determining its viability as a source of renewable energy. Current density-voltage (J-V) measurements are a powerful tool for evaluating the performance of solar cells. The J-V curve provides a quantitative characterization of the current-voltage relationship of a solar cell, providing important information about the device's key parameters, including open-circuit voltage (V_{oc}), short-

circuit current (I_{sc}), and fill factor (FF). Figure 2.1 shows a J-V curve for a perovskite solar cell with $FA_{0.8}Cs_{0.2}PbI_{2.4}Br_{0.6}Cl_{0.02}$ as the absorber layer. The figure is labeled with all the important parameters.

The open-circuit voltage (V_{oc}) is the voltage at which the current through the

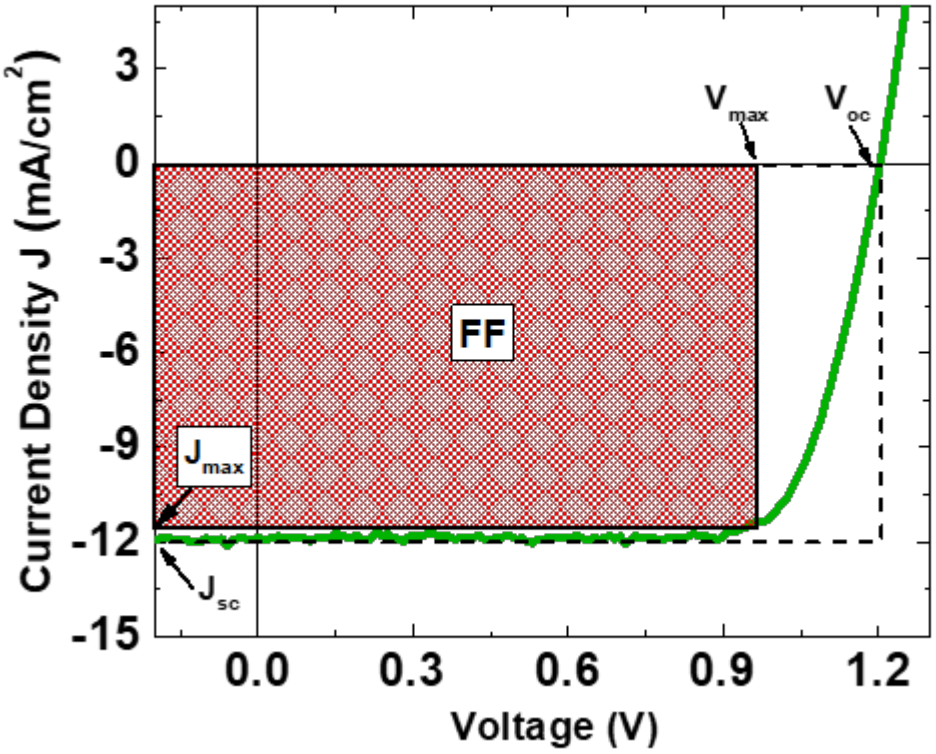


Figure 2.1: Current density(J)-Voltage(V) characteristics of a perovskite solar cell with $FA_{0.8}Cs_{0.2}PbI_{2.4}Br_{0.6}Cl_{0.02}$ absorber layer, showing the critical parameters for a solar cell.

solar cell is zero ($J = 0$), while the short-circuit current (J_{sc}) is the current that flows when the voltage across the cell is zero ($V = 0$). The fill factor is a measure of the ideality of the solar cell in converting light into electricity, and is determined

by the ratio of the maximum power output of the solar cell to the product of the open-circuit voltage and short-circuit current:

$$FF = \frac{P_{max}}{V_{oc} \cdot J_{sc}}$$

Hence, the power conversion efficiency for a solar cell can be defined as:

$$\eta = \frac{P_{max}}{P_{in}} = \frac{J_{max} \cdot V_{max}}{P_{in}} = \frac{V_{oc} \cdot J_{sc} \cdot FF}{P_{in}}$$

Where, P_{in} is the input power and J_{max} is the maximum current extracted and V_{max} is the maximum operating voltage [5].

J-V measurements are commonly used to evaluate the efficiency of different solar cells, and to compare the performance of various devices. The analysis of the J-V curves of solar cells enables one to deduce the underlying physics of the device and any parasitics in performance and identifies areas for optimization and improvement.

In the absence of light, a solar cell behaves as a normal p-n diode. This means that we can use the ideal diode equation to determine the J-V characteristics of a solar cell when it is not illuminated, denoted as $J_{dark}(V)$. The ideal diode equation describes the relationship between the current and voltage in a diode. The equation is given as:

$$J_{dark}(V) = J_0 \left[exp\left(\frac{qV}{mk_BT}\right) - 1 \right]$$

In this equation, J_0, q, k_B, m, and T represent the dark saturation current

density, the charge of a single electron, the Boltzmann constant, the diode ideality factor, and the lattice temperature, respectively [5].

When a solar cell is exposed to light, its behavior changes. We can express the way it behaves mathematically by adding two parts. The first part is a constant electric current produced by the solar cell's exposure to light, and we call it the short-circuit current (J_{sc}). The second part is the ideal diode equation that represents the cell's behavior without light. This equation is used to determine the electric current (J_{dark}) that is generated when the cell is not exposed to light. When we add the two parts, we get a new equation to describe the solar cell's behavior under light, given by [5]:

$$J(V) = J_{dark}(V) - J_{sc} = J_0 \left[exp\left(\frac{qV}{mk_BT}\right) - 1 \right] - J_{sc}$$

This equation or superposition explains how a solar cell behaves under different lighting conditions.

To understand the properties of solar cells in the laboratory at OU under the AM1.5 (or AM0) solar spectrum, a Newport Oriel Sol2A solar simulator is used. The test solar cells are supplied with an applied bias through a Keithley 2400 multimeter that measures the extracted current from the device. This system allows the determination of the current density-voltage characteristics of solar cells in the temperature range of 77 K to 350 K using a Linkam THMS600E cryostat connected to a Linkam LNP95 cooling system.

Moreover, mono-wavelength J-V measurements are also common in the labora-

tory and are conducted using a single wavelength ("mono") laser source (typically 552 nm), which is used to excite the sample in the Janis cryostat enabling temperature and power-dependent J-V measurements. In our lab, we specialize in performing simultaneous PL and J-V measurements at different temperatures and powers. This enables us to have a better understanding of the photophysics of a solar cell than just using optical or electrical measurements alone.

Figure 2.2 shows a flipped normalized power-dependent photoluminescence plot

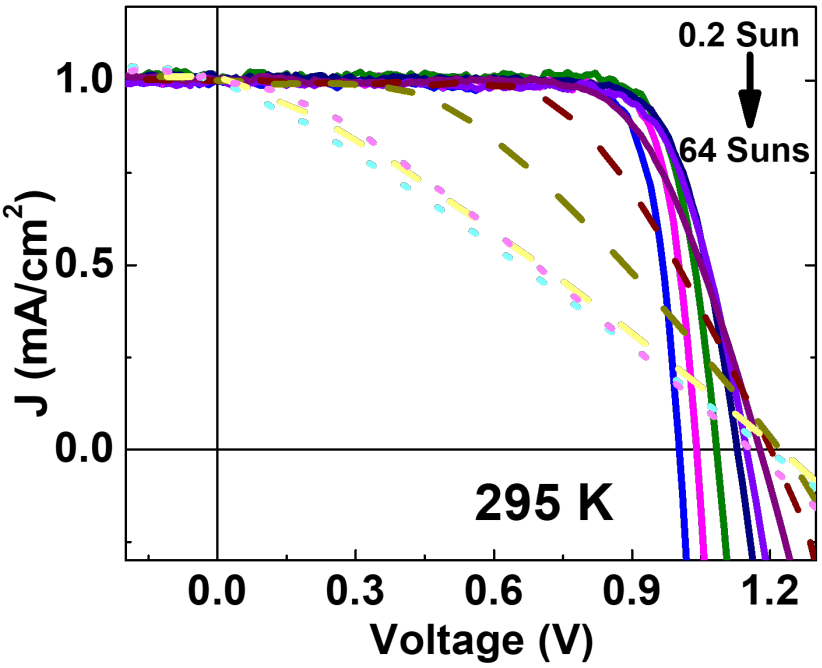


Figure 2.2: The normalized J-V characteristics for a $(FA_{0.8}Cs_{0.2})Pb(I_{2.4}Br_{0.6}Cl_{0.02})$ perovskite solar cell as a function of power, illustrating the presence of hot carriers at higher powers, as evidenced by changes in the J-V curve (see Chapter 5 for details). [11]

for a $(FA_{0.8}Cs_{0.2})Pb(I_{2.4}Br_{0.6}Cl_{0.02})$ solar cell, normalized with respect to the short circuit current (J_{sc}), which is a commonly used representation in the photovoltaic community to investigate the behavior of the J-V curve with respect to power. The power density is shown as a suns equivalent power density in AM1.5G conditions, where 1 sun represents 100 mW/cm^2. Here, the simultaneous J-V and PL technique was employed to understand the nature of charge carriers, where the rectification loss in the J-V indicates the presence of hot carriers, a result which is supported by the photoluminescence spectra. The details of these findings are discussed in Chapter 5 [11].

2.3 Reflectance

Reflectance is a technique used for material characterization and study, and it provides valuable information about the optical properties of a material. When light interacts with a material, some of it is absorbed, some of it is transmitted through the material, and some of it is reflected back. The reflectance measurement method measures the amount of light that is reflected from the structure of a material as a function of the wavelength of the incident light and provides information about the absorption of a material and its bandgap and/or properties related to photonic stop bands and system designed to reflect specific wavelengths by design such as distributive Bragg reflectors (DBRs).

The OU laboratory employs an Oriel Cornerstone 260 monochromator and an

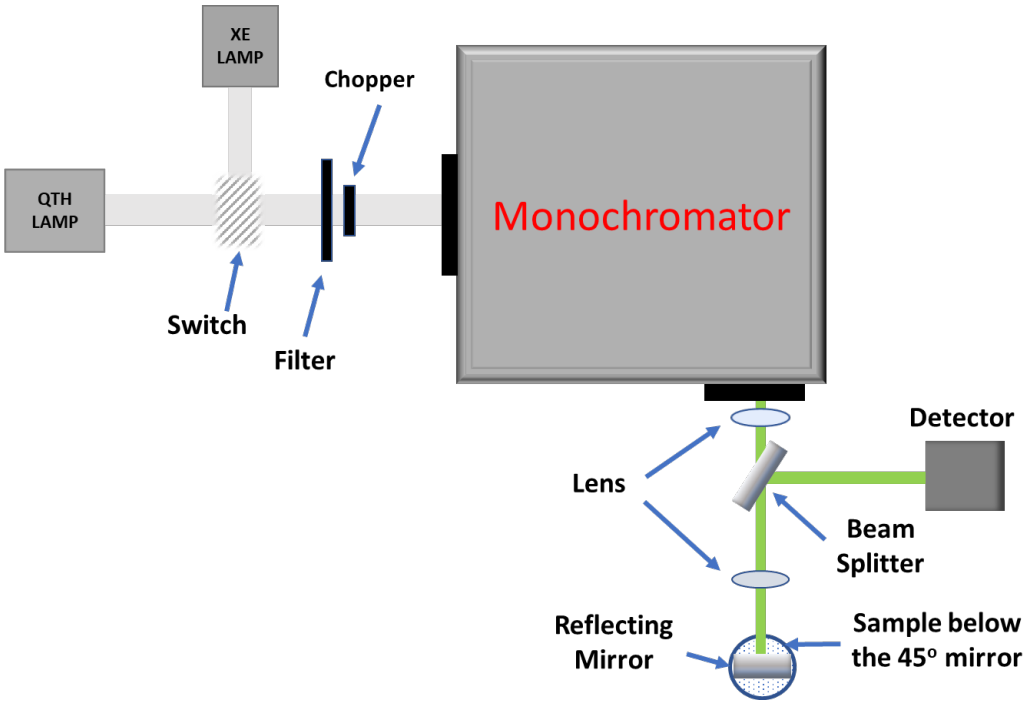


Figure 2.3: Schematic of a reflectivity measurement setup used to analyze the wavelength dependence of the bandstructure of a material or device, and/or the presence of stop bands in distributive Bragg reflectors (DBRs).

Oriel Merlin digital lock-in amplifier radiometry system to measure reflectance. A schematic of the reflectance setup is shown in Figure 2.3. The light sources are used for characterizing reflectance are either a quartz tungsten halogen (QTH) bulb or xenon (Xe) lamp. These lamps emit light across the ultraviolet (UV) to infrared (IR) (including the solar) spectrum. A silicon (Si) detector or a germanium (Ge) detector is used to measure the incident light intensity between 300 nm to 1100 nm or 700 nm to 1800 nm, respectively. Additionally, the temperature dependence of reflectance can be studied using the Linkam cryostat over a range of 77 K to 350 K.

The light from the source is directed into the monochromator, which disperses the white light into separate wavelengths and performs a wavelength sweep. Each wavelength in the sweep is directed onto the sample using optical lenses. The reflected light is collected using a mirror and optics and directed to the detector using a beam splitter. By measuring the reflectance of a material at different wavelengths, it is possible to determine its optical properties, such as the stopband for a microcavity. This property can then be used to design and optimize the microcavity to study polariton physics, for example.

Figure 2.4 (a) shows the reflectance spectra of a SiO_2/Si_3N_4 DBR microcavity.

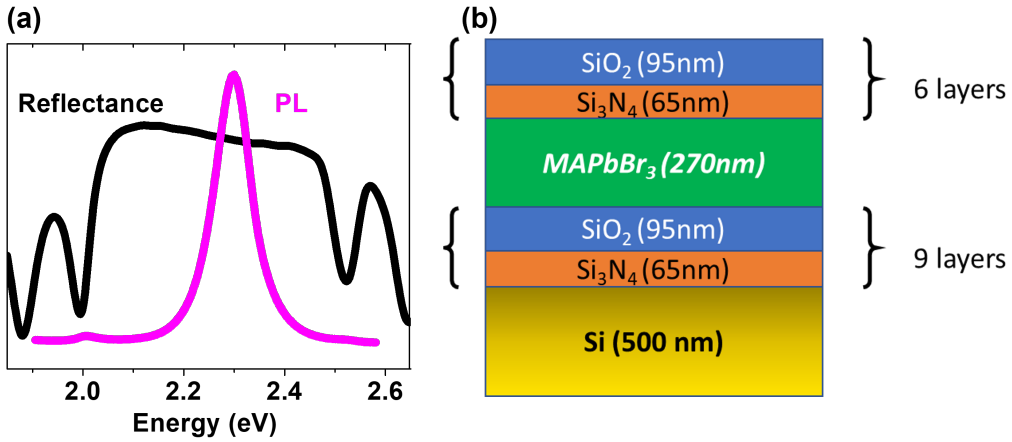


Figure 2.4: (a) Reflectance (black) and photoluminescence (magenta) spectra of a material obtained using the reflectivity setup; (b) Schematic representation of a microcavity fabricated using SiO_2/Si_3N_4 Distributive Bragg reflectors as mirrors on both sides with $MAPbBr_3$ as the absorber material assessed by the author.

The microcavity consists of multiple DBR mirrors (both sides) encapsulating an absorber design to be of a specific optical thickness. In Figure 2.4 (b), the absorber

is the perovskite material ($MAPbBr_3$), which has large exciton binding energy and a large absorption coefficient such that it interacts strongly with light [8-10]. As light of the targeted wavelengths enters the cavity, it is trapped within the cavity by the total internal reflection and propagates within the cavity, resulting in standing waves of light. This confinement of light within the cavity leads to an enhanced interaction between the light and the material (matter) within either the strong or weak coupling regime. This interaction in the former case results in the formation of new states of matter known as polaritons [6]. These polaritons are of interest for a potential application in a new generation of optical devices and quantum technologies.

2.4 Absorption

2.4.1 Absorption: Theory

The interaction of photons with electrons in a semiconductor results in optical absorption, where the electrons are excited from the valence band to the conduction band. This is known as an optical transition. The amount of light absorbed is dependent on the density of free carriers in the conduction band and holes in the valence band. When the carrier density in a semiconductor increases, the absorption of light increases as well, resulting in a higher optical transition rate. This relationship is described by the Beer-Lambert Law, which states that the transmittance (T) of a material is proportional to the exponential of the product

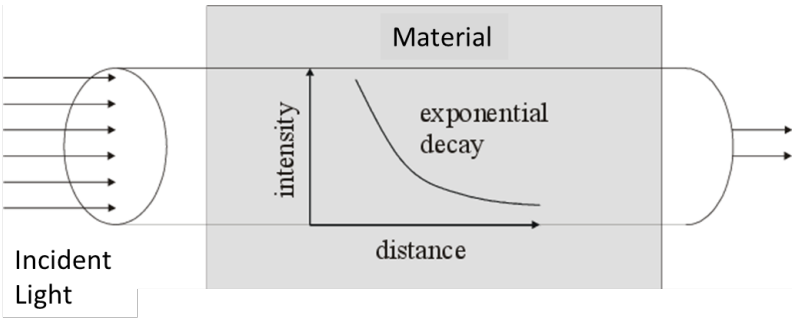


Figure 2.5: Schematic representation of Beer-Lambert Law depicting the absorption of incident light as it passes through a material [1].

of the molar absorption coefficient (ϵ) of the material, the concentration (c) of absorbing species, and the path length (l) of the light through the material, and can be expressed as the following equation:

$$T = exp\left(-\epsilon \cdot c \cdot l\right)$$

or

$$T = exp\left(-\alpha \cdot l\right)$$

Where, α is the Naperian absorption coefficient and equals the product $\epsilon \cdot c$ Therefore, a higher number of free carriers in a semiconductor means more light will be absorbed, leading to a lower transmittance and a greater optical transition rate [12]. This is very important parameter for solar cells where controlling light absorption is essential for efficient energy conversion.

Figure 2.5 shows the Beer-Lambert law in action and explains how the intensity of light changes (decays) as it passes through a medium. The law assumes that the absorbing species are homogeneously distributed in the material.

However, for a comprehensive analysis of absorption spectra, especially in which excitonic process perturbed the absorption from the continuum especially at the band edge, the Elliot model is often preferred [6]. The Elliot equation is a more comprehensive and theoretical approach to studying light absorption in solids, taking into account the intricate electronic structure of the material and correcting for non-uniform absorption and multiple scattering of light. Hence, for a more precise and accurate examination of the absorption spectra of a material, especially in the case of materials such as semiconductors, the Elliot equation is a more appropriate model.

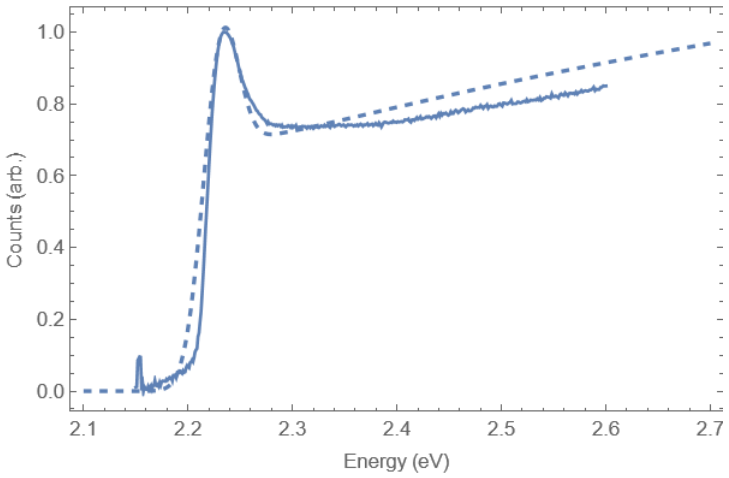


Figure 2.6: Absorption spectra of $FAPbBr_3$ (solid lines) and the fitted line using the Elliot fit absorption model (dotted lines) with a convoluted Voigt function.

The Elliot model defines the equation for the absorption coefficient as [6,13]:

$$\alpha(\nu) = \alpha_0^{3D} \sum_{n=1}^{\infty} \frac{4\pi}{n^3} E_b^{3/2} \delta\left(h\nu - E_g + \frac{E_b}{n^2}\right) + \frac{2\pi\sqrt{E_b}}{1 - e^{-2\pi\sqrt{\left(\frac{Eb}{h\nu - E_g}\right)}}} \theta(h\nu - E_g) \quad (2.1)$$

Where the first term is associated with exciton and the second term is associated with continuum [6].

Figure 2.6 presents the absorption spectra of the $FAPbBr_3$ perovskite, represented by the solid lines, which are fitted by the author using the Elliot model of absorption, represented by the dotted lines. To obtain the fitting, a Voigt function is convoluted with Equation 2.1. The Elliot model of absorption is used to analyze the optical properties of the material, providing information about its band gap, the binding energy of the exciton, and the broadening of the excitonic contribution, among other properties [13].

2.4.2 Absorption: Experimental setup

Absorption is a fundamental property of a material that characterizes how it interacts with light. In the context of material characterization, absorption is used to understand details of the band structure and the interaction strength of light with the material (matter) and is often used as a function of temperature to study the nature of the bandgap and the effects of intrinsic and extrinsic excitons, for example, Figure 2.7 illustrate a custom-built continuous wave absorption setup. A white light source (QTH/Xe lamp) is used to transmit through the sample in a cryostat (Janis closed-cycle helium system). As the light passes through the

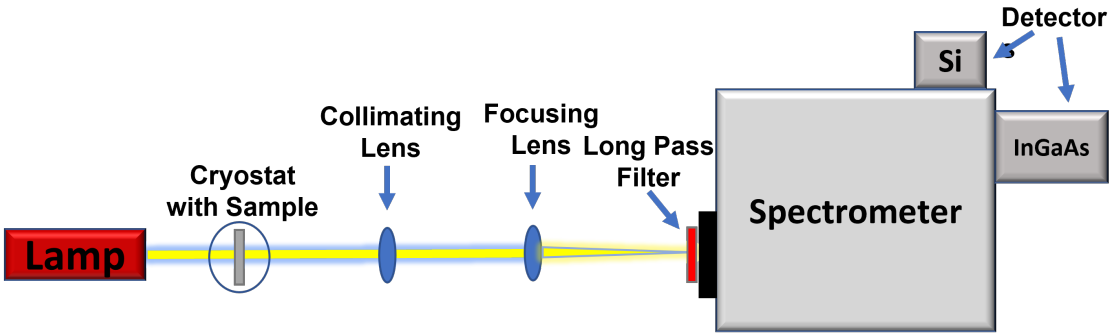


Figure 2.7: Schematic diagram of the absorption setup used in the study. The custom-made setup broadly includes a light source, a sample holder, and a detection unit to measure the absorption of the sample.

sample, it interacts with the material, and some of the light is absorbed. The transmitted light that passes through the sample is then collected and focused using optical lens and directed into the Princeton Instrument Acton SP2500 spectrometer, which separates the light into its component wavelengths and measures the intensity of each wavelength and detects the strength of the signal with either an air-cooled-Si charge-coupled device (2-dimensional CCD array) for shorter wavelengths (300 nm - 100 nm) or a liquid N_2 cooled InGaAs linear array for longer wavelengths (750 nm to 1600 nm).

The recorded spectrum then provides physical information about the absorption properties of the material at the wavelength of interest. The amount of light absorbed by the sample is dependent on the material properties and the thickness of the sample, among other factors.

Winspec © software is used as data acquisition software to analyze the spectra for different temperatures. By measuring the absorption spectra of a material as a function of temperature, it is therefore possible to study changes in the material's electronic structure and related optical properties with respect to temperature.

2.4.3 Photoluminescence

Photoluminescence (PL) is a phenomenon in which a material re-emits light after absorbing light via a high energy optical excitation source (such as a laser). This is an important phenomenon in the field of optoelectronics, where it is used for a variety of applications such as lighting [7], displays [16,17], and sensing [18]. Figure 2.8 shows a schematic model of photoluminescence. Photoluminescence occurs when an electron in the material is excited by an external light source ($\hbar\omega'$) (1) returning to its original energy state via the emission of phonons, relaxing to the bottom of the conduction band (2) before radiatively recombining with a photogenerated hole in the valence band releasing a photon ($\hbar\omega$) (3). This process results in the emission of light that is of lower energy (color) or intensity than the light that was absorbed.

Photoluminescence is commonly used in semiconductors to study the properties of the material, such as its bandgap, exciton binding energy, and the presence of non-radiative process (via quenching of the emission). This can also (in metal

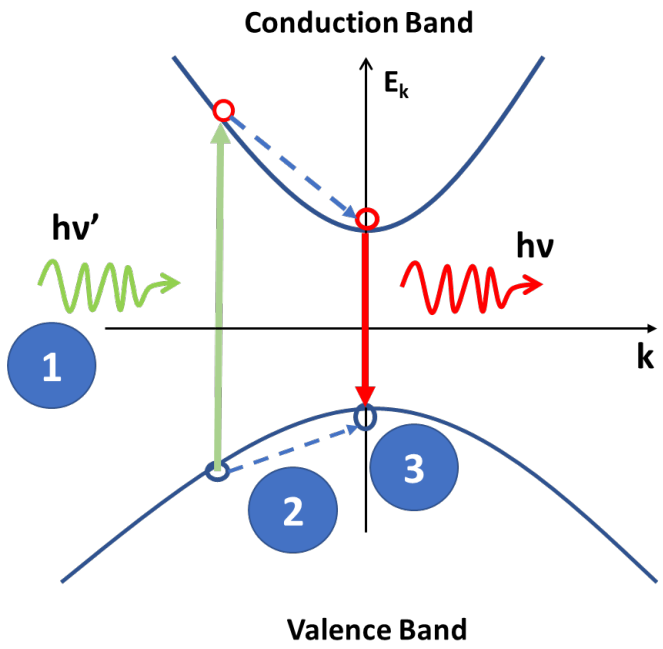


Figure 2.8: Schematic illustration of the photoluminescence process in a semiconductor, from excitation to relaxation, as represented by a band diagram. The process involves the absorption of photons, followed by the creation of electron-hole pairs, which then relax to the band edge and recombine and emit light.

halide perovskites) provide information of structural phase transitions [2,14]. The intensity and wavelength of the light emitted can provide insight into the electronic structure of the material and its interactions with other materials (barriers in devices or heterostructures, for example).

When a semiconductor material is photo-excited, it undergoes various relaxation processes that bring it back to its ground state. These processes can be separated into two categories: radiative and non-radiative. Radiative recombina-

tion encompasses both spontaneous and stimulated photon emission, the former of which is an intrinsic property of the material. Non-radiative recombination, however, can arise from both intrinsic and extrinsic causes. Auger recombination is an intrinsic process involving carrier-carrier interactions [6], while carrier trapping due to impurities and defects in the crystal structure is extrinsic and caused by non-idealities such as in materials growth and/or via device processing [6].

2.4.4 Photoluminescence Experimental Setup

Photoluminescence is a non-destructive technique that uses a monochromatic light source, such as a laser, to excite the material. The excitation can be achieved using different lasers such as (in this work) a He-Ne red laser (632.8 nm), a solid state green laser (532 nm), an IR Laser source (1064 nm), and/or blue laser excitation (442 nm). The selection of the laser source depends on the bandgap of the material being studied. The photoluminescence setup, as shown in Figure 2.9 [2], typically includes optics that allow for different laser sources to be switched back and forth to study different samples. The laser excites the sample using collimation and focusing optics shown in Figure 2.9 that focuses the excitation source upon the sample under investigation, which is mounted in a closed cycle cryostat allowing the investigation of both temperature and (excitation) power dependent PL measurements.

The excited spectrum is then collected by a collimating lens and passed to a

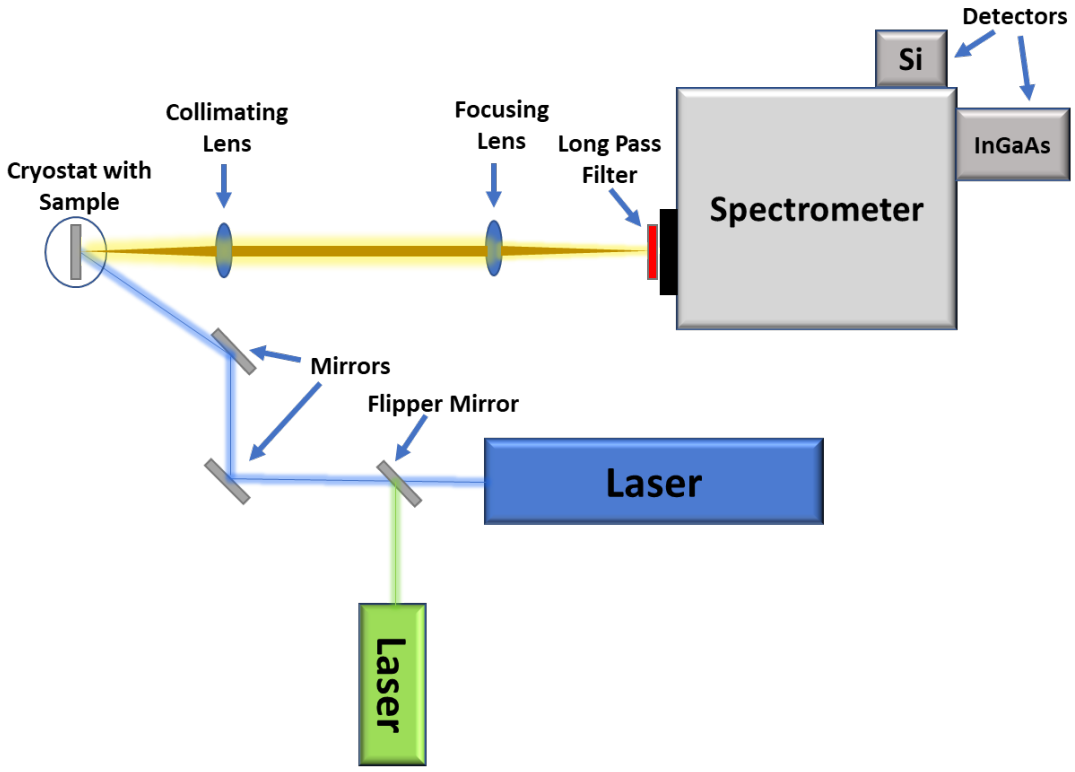


Figure 2.9: Schematic representation of the experimental arrangement for photoluminescence measurement.

focusing lens. The focused beam then passes through a long pass filter to remove any reflected or stray laser light from entering the spectrometer such that only the PL from the samples is collected/detected. The detected PL signal is then recorded by a suitable detector, depending on the material's bandgap and the laser source, and the resulting data is plotted using a computer. For instance, detectors such as Si or InGaAs may be utilized. The spectral characteristics and intensity of the emitted light provide valuable insight into the electronic and optical properties of the materials.

2.5 Ultrafast Transient Absorption

Ultrafast transient absorption (TA) is a powerful spectroscopic technique that is widely used in the study of organic-inorganic metal halide perovskites [15]. This technique allows the study of the photophysical processes and the changes in the electronic and structural properties that occur in these materials in the ultrafast regime. TA is performed by measuring the absorption of light by a sample as a function of time after the initial excitation. By monitoring changes in absorption, the decay kinetics of excited states can be studied in the material.

Figure 2.10 (a) illustrates the schematic of an ultrafast experiment, which involves

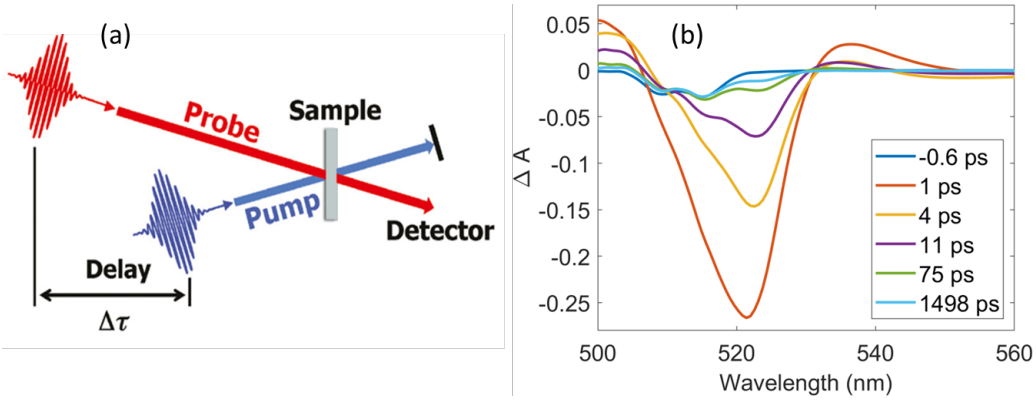


Figure 2.10: (a) Schematic of the ultrafast transient absorption spectroscopy (TA) experiment is shown, which involves using a pump pulse to excite the sample and a probe pulse to study the carrier dynamics. (b) shows the time-dependent ultrafast transient absorption spectra of $(EPEA)_2PbI_4$ obtained using a 442 nm pump pulse from a Helios Ultrafast system. The observed kinetics of states or features in the TA spectra as time evolves provides critical information on the energy state dynamics of the sample. [3,4]

ultrafast transient absorption (TA) - a pump-probe technique in which a sample is excited with a short pulse of light from a laser (pump pulse). The duration of the pulse is typically on the order of femtoseconds, which enables excitation of the sample before any significant relaxation or decay takes place. Subsequently, a second pulse of light (probe pulse) is used to probe the sample. The probe pulse is absorbed by the sample, leading to changes in its absorption spectrum. By varying the time delay between the pump and probe pulses using a mechanical stage that adjusts the optical path length, information about the kinetics of the energy states in the sample as a function of time is obtained.

Figure 2.10 (b) shows a TA spectrum of $(EPEA)_2PbI_4$ at various time delays, providing information on the energy state dynamics within the sample. A comprehensive discussion of these results is provided in Chapter 6. Further details on the methodology and analysis of TA spectrum can be found in Chapters 4 and 6.

One of the key advantages of TA is its ability to provide ultrafast time-resolved information. Organic-inorganic metal halide perovskites are highly dynamic materials, with photogenerated carriers that rapidly thermalize and recombine, and can form new excitonic species. The TA measurement is fast enough to capture these events in real-time, allowing the deconvolution of the complex dynamics in these (and many other) materials

In the case of organic-inorganic metal halide perovskites, TA has been used

to study the fast recombination processes that occur between photogenerated carriers and the formation of defects in the material [20]. For example, the fast decay of excitons and the formation of charge-transfer states in these materials has been studied using to probe the energy transfer dynamics between different components of organic-inorganic hybrid material [19-21].

2.6 References

1. S. Welzel et al, "J. Phys.: Conf. Ser.", vol. 86, 012012, 2007.

2. S. Sourabh, V. R. Whiteside, I. R. Sellers, Y. Zhai, K. Wang, M. C. Beard, V. Yeddu, M. T. Bamidele, and D. Y. Kim, Phys. Rev. Mater. 5, 095402 (2021).

3. J. Lauth, S. Kinge, and L. D. Siebbeles, Zeitschrift fu¨r Physikalische Chemie 231, 107 (2017).

4. R. Berera, R. van Grondelle, and J. T. M. Kennis, Photosynthesis Research 101, 105 (2009).

5. J. Nelson, The physics of solar cells (Imperial College Press, 2003).

6. J. I. Pankove, "Optical Processes in Semiconductors," Dover Publications, Inc., New York, 1975. (Unabridged republication of the work originally published by Prentice-Hall, Inc., 1971).

7. A. Jorio, G. Dresselhaus, M. S. Dresselhaus, "Carbon Nanotubes: Advanced Topics in the Synthesis, Structure, Properties and Applications", Springer Science & Business Media, 2007, ISBN 978-3-540-72865-8.

8. J. Wang, et al., "Transient Lasing Behaviors in MAPbBr3 Perovskite Microcavities", The Journal of Physical Chemistry C, vol. 126, no. 35, pp. 14922-14930, 2022.

9. S. Ghosh, R. Su, J. Zhao, A. Fieramosca, J. Wu, T. Li, Q. Zhang, F. Li, Z. Chen, T. Liew, D. Sanvitto, Q. Xiong, "Microcavity exciton polaritons at room temperature", Photonics Insights, vol. 1, no. 1, R04, 2022.

10. K. Zheng, et al., "Exciton Binding Energy and the Nature of Emissive States in Organometal Halide Perovskites", The Journal of Physical Chemistry Letters, vol. 6, no. 15, pp. 2969-2975, 2015.

11. S. Sourabh, H. Afshari, V. R. Whiteside, and M.C. Beard, I. R. Sellers " Evidence of Hot Carrier Extraction in Metal Halide Perovskite Solar Cells ", Physical Review X (under review).

12. T. G. Mayerhöfer, S. Pahlow, J. Popp, ChemPhysChem 2020, 21, 2029.

13. V. D'Innocenzo, "Photophysics of 3D lead halide perovskite semiconductors: Light absorption and Luminescence", Ph.D. thesis, Politecnico di Milano, Dipartimento di Fisica, 2015.

14. K. Schötz, A. M. Askar, A. Köhler, K. Shankar, F. Panzer, "Investigating the Tetragonal-to-Orthorhombic Phase Transition of Methylammonium Lead Iodide Single Crystals by Detailed Photoluminescence Analysis", Adv. Optical Mater. 8, 2000455 (2020). https://doi.org/10.1002/adom.202000455

15. R. Berera, R. van Grondelle, J.T.M. Kennis, "Ultrafast transient absorption spectroscopy: principles and application to photosynthetic systems", Photosynthesis Research, vol. 101, no. 2, pp. 105-118, 2009.

16. W. A. Crossland, I. D. Springle, R. D. King, P. A. Bayley, A. B. Davey, B. Needham, "Photoluminescent liquid crystal displays and a new approach to large screen video applications", *Proc. SPIE* 3955, Liquid Crystal Materials, Devices, and Flat Panel Displays, 17 March 2000, DOI: https://doi.org/10.1117/12.379968.

17. Y. Kang, Z. Song, X. Jiang, X. Yin, L. Fang, J. Gao, Y. Su, F. Zhao, "Quantum Dots for Wide Color Gamut Displays from Photoluminescence to Electroluminescence", *Nanoscale Res. Lett.* 12, 154 (2017), DOI: https://doi.org/10.1186/s11671-017-1907-1.

18. N. De Acha, C. Elosua, I. Matias, F. J. Arregui, "Luminescence-Based Optical Sensors Fabricated by Means of the Layer-by-Layer Nano-Assembly Technique", *Sensors* (Basel), vol. 17, no. 12, pp. 2826, Dec. 2017, DOI: https://doi.org/10.3390/s17122826. PMID: 29211050; PMCID: PMC5751518.

19. G. Folpini, et al., "The role of a dark exciton reservoir in the luminescence efficiency of two-dimensional tin iodide perovskites", J. Mater. Chem. C, vol. 8, no. 31, pp. 10889-10896, 2020.

20. B.H. Li, H. Li, H. Di, Z. Xuan, W. Zeng, J.-C. Wang, D.-B. Cheng, C. Zhou, X. Wang, Y. Zhao, J. Zhang, Z. Ren, X. Yang, "Spectroscopic Investigation of the Photoinduced Charge Dynamics in a Mixed-Halide Perovskite", JACS Au, vol. 3, no. 2, pp. 441-448, 2023. DOI:10.1021/jacsau.2c00581.

21. A. Boulesbaa, K. Wang, M. Mahjouri-Samani, M. Tian, A. A. Puretzky, I.

Ivanov, C. M. Rouleau, K. Xiao, B. G. Sumpter, D. B. Geohegan, "Patterning of Two-Dimensional Materials by Laser Direct-Write Lithography", J. Am. Chem. Soc. 138 (44), 14713-14719, 2016. DOI: 10.1021/jacs.6b08883.

Chapter 3

Hot Carrier Dynamics in Thin Film Metal Halide Perovskites

3.1 Introduction

In chapter 1, a brief introduction of the halide perovskites and their structure was provided. Here, the specific perovskite and its importance regarding the physics of hot carrier dynamics has been assessed in order to understand the fundamental properties of metal halide perovskites (MHP) for developing the prospective hot carrier solar cell.

MHP have gained significant attention in recent years due to their remarkable properties and potential applications. These materials have a ABX_3, where 'A' represents a monovalent organic cation, 'B' denotes a divalent metal cation, and 'X' is a halide anion. The elements used in typical materials for photovoltaics (PV) are earth-abundant and have the potential to be synthesized and fabricated at low cost, making perovskites an attractive alternative to traditional semiconductors, particularly for PV applications.

An intriguing property of this group of materials is that they are highly tunable. By changing the composition of the constituent materials, the electrical and optical properties of the halide perovskite structure can be tailored and controlled

[1,2]. One of the most exciting applications of the MHP has been in the field of solar energy. Since their first appearance on the National Renewable Energy Laboratory's solar cell efficiency chart in 2013, the MHP have shown a remarkable increase in solar cell efficiency, with a reported efficiency of 25.5% in 2020 [50]. This increase in efficiency has been attributed to the excellent light absorption properties and charge carrier mobility of these materials. [51-53]

However, the interest in MHP extends beyond conventional solar cell research [3-6]. These materials have also been considered in light emitters, transistors, and flexible electronics, as well as potential space power systems [60]. In advanced concepts PV, early predictions of long hot carrier lifetimes made many in the community consider these systems as a candidate material for hot carrier solar cells [7-12]. This was based on data observed in transient absorption measurements that sparked considerable interest in using MHP as absorbers in hot carrier solar cell architectures [13-15].

Here, a study aimed at understanding the factors underlying the hot carrier cooling rates suggested in previous experiments in the MHP [3,7,8-12,16-20] is presented and discussed. Focus is made on several different perovskite systems that span a wide bandgap energy range and have varying degrees of ionicity, exciton binding energy, and phononic properties [57].

To investigate the factors contributing to the apparent slowed hot carrier cool-

ing rates, complimentary continuous wave temperature-dependent PL and transmission, power-dependent PL, and ultrafast transient absorption spectroscopy (Chapter 4) are all considered. These measurements are discussed briefly in Chapter 2 and together provides considerable information regarding the physical properties of the materials. Here, these measurements are examined with relation to hot carrier dynamics and particularly via the phononic properties, [55] ionicity, [54] and possible polaron interactions [40] in the perovskite studied.

3.2 Temperature Dependent Photoluminescence

Figure 3.1 demonstrates the correlation between temperature-dependent photoluminescence (PL) spectra of four perovskite thin films, namely (a) $FAMAPbSnI_3$, (b) $FAPbI_3$, (c) $FAMAPbI_3$, and (d) $FAPbBr_3$. The figure displays the normalized photoluminescence spectra arranged in waterfall format. The observed shift towards higher energy with increasing temperature in all four MHP shown is typical of these systems and is attributed to the unique bandstructure for these materials specifically the p-like conduction band and s-like valence band nature in these soft systems [21,22].

The introduction of methyl ammonium to $FAPbI_3$ (Figure 3.1 (c)) results in a slight increase in PL emission energy indicating an increase in the effective band gap of $FAMAPbI_3$ with respect to $FAPbI_3$; however, the thermally induced shift

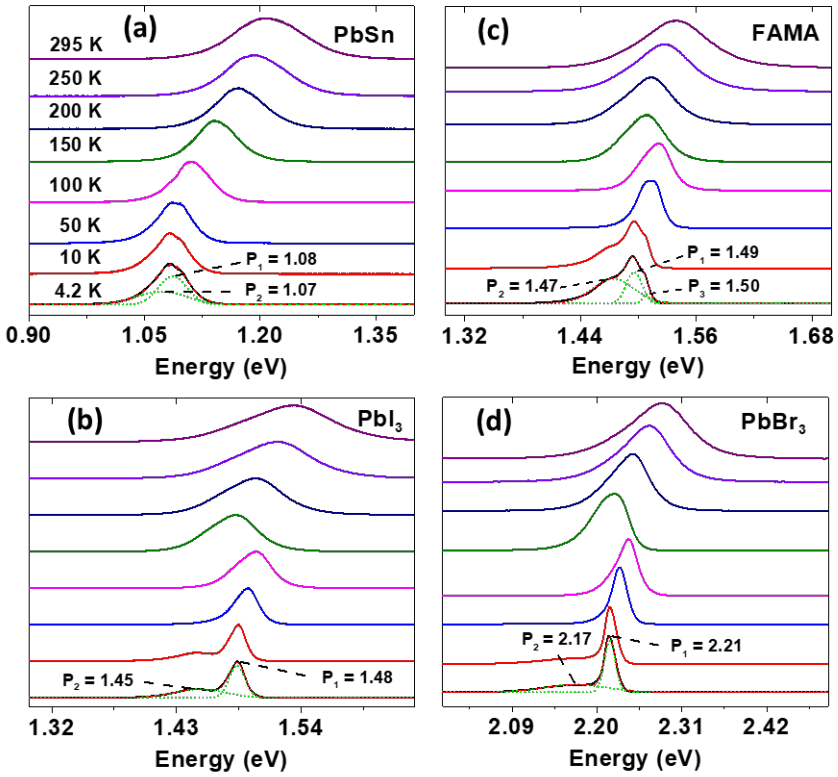


Figure 3.1: Temperature dependent PL from 4.2 to 295 K (color coded offset format) for (a) $FAMAPbSnI_3$, (b) $FAPbI_3$, (c) $FAMAPbI_3$, and (d) $FAPbBr_3$, respectively. Low-temperature features are labeled across all plots.

in emission for all samples remains ≈ 50 meV. Additionally, a detailed analysis of the extracted parameters suggests that the addition of methyl ammonium has negligible impact compared to $FAPbI_3$, implying that the inorganic framework determines the optical characteristics of these thin films therefore, the shift is likely due to PbI_3 in this case [57].

The PL of the systems in Figure 3.1 is dominated by a higher energy peak

(P1) attributed to exciton emission, which is related to the band gap of the materials, along with a lower energy peak (P2), and an asymmetric low energy tail. In general, the MHP are excitonic in nature, which dominate the optical properties of the systems particularly at low temperature but that also manifest themselves at higher temperatures particularly in the high bandgap systems such as $FAMAPbBr_3$ since these have exciton with binding energy (E_B) $> k_BT$ (see Figure 3(d)).

As can be seen in Figure 3.1, the energy separation between the main feature in PL (P1) and the low energy transition (P2) varies in each system. For instance, in the Sn-based $FAMAPbSnI_3$, the $\Delta E_{P1-P2} \sim 10$ meV (P1: 1.08 eV; P2: 1.07 eV) while $FAPbBr_3$ has a ΔE_{P1-P2} of ~ 40 meV (P1 = 2.21 eV; P2 = 2.17 eV). In case of $FAPbI_3$ ΔE_{P1-P2} is ~ 10 meV, much smaller than the equivalent Br system (~ 40 meV). In contrast, $FAMAPbI_3$ has $\Delta E_{P1-P2} \sim 20$ meV and exhibits an additional feature at 1.5 eV (P3), 10 meV higher in energy than the ground state transition P1 (1.49 eV).

The origin of P3 is still unknown, but it is likely due to material segregation, phase modulation, and/or due to the effects of strain. Previous studies have shown that strain and reduced structural symmetry can lead to a relaxation of optical transition selection rules in $FAMAPbI_3$ [23], which can result in additional fine structure in the system, and likely applies to a range of perovskites particularly when there is strain in the system.

Typically, in Pb-based systems, the lower energy peak (P2) is thought to arise from emission either localized states or mediated by defects. If P2 were an intrinsic exciton with a large density of states, it would be expected to dominate the low-temperature photoluminescence (PL) as the lowest energy transition and can be correlated to the excitonic feature seen in absorption (Figure 3.3 (a-c)). However, neither of these characteristics are evident in the insets to Figure(s) 3.3(a-c)), which shows these are related to localized states or defect-mediated states.

The present study suggests that the source of the emitting complex P2 can be attributed to slight variations in the structural configuration of different metal-halide perovskite thin films [22,23]. For example, these variations may result from the formation of slightly different orthorhombic bonds or twist angles that are modulated by temperature [24,25]. These structural variations can arise from different local strain fields, which may therefore lift the band structure degeneracy. Additionally, these structural variations can also result from localized differences in electronegativity and/or the formation of self-trapped excitons or isoelectronic centers [26,61]. Self-trapped excitons result when the crystal structure is distorted or when there are irregularities in the lattice, which localize charge carriers [26]. On the otherhand, isoelectronic centers refer to impurities or localized states that arise from mismatches in atom size within a crystal. These mismatches create an

electronegativity in the material that attracts and localizes charges. Since these centers are inherent to the system, they have a considerable concentration or density of states. Such complexes result in subgap states that reflect the binding of localization energy of the center [25].

A noticeable change in the PL peak towards higher energy and redistribution of charge carriers among the various PL transition can be observed below the phase transition temperature of $\sim$ 150 K in Figure 3.1. At $T > 50$ K, the PL is dominated by a single feature (P1), which is linked to the intrinsic properties of the materials, while P2, which is likely a defect state or extrinsic non-ideality, continues to contribute to the band tail, but with diminishing contribution as T increases. At $T > 150$ K, P2 disappears, which is attributed to the redistribution of charge carriers between states when the localized carriers have sufficient thermal energy to escape and transfer to the dominant transition, P1, which is separated (in this case) by less the $\sim$ 10 meV (150 K). Moreover, above 50 K the linewidth of the PL also increases. This is due to increasing electron-phonon interaction in these strongly polar systems, further screening P2 at higher temperatures.

In case of $FAMAPbSnI_3$ (Figure 3.1 (a)), the presence of different features in the photoluminescence appear closely related to the stability and purity of this MHP, as well as the symmetry of the systems structure. When the $FAMAPbSnI_3$ samples are pristine, the appearance of two features close to the peak of the photoluminescence suggests that the structure of the mixed Pb-Sn alloys may

have better homogeniety and lower intrinsic strain. However, the pronounced linewidth broadening observed in the $FAMAPbSnI_3$ samples in comparison to the pure Pb samples, as depicted in Figure 3.2, is likely attributed to compositional variations [26] and/or phase separation.

It is interesting to note that recent research has shown that temperature-dependent photoluminescence of FASnI3 also displayed similar broadening to that presented here [11], indicating that broad photoluminescence may be an intrinsic characteristic of Sn-based MHP. The different features observed in the photoluminescence are likely caused by variations in the structure of the material, which can be due to degradation-induced strain and oxidation of Sn, local variations in structural symmetry, or electric fields [27-29], which can impact the degeneracy of the bandstructure [21,23,30].

While in Figure 3.1, it can be observed that above the structural phase transition temperature ($T > 150$ K), the energy shift to lower levels is noticeable in the case of the pure Pb-based MHP, which is expected since the band gap is reduced when the materials transition from the orthorhombic to the tetragonal phase. Also, despite the increasing dominance of the P1 transition in the photoluminescence, in all cases (Figure 3.1), the PL still shows evidence of a low-energy Urbach tail [56] and significant broadening at room temperature. This suggests the presence of several subtle and competing complexes at the band edge. The presence of these complexes is particularly noticeable in $FAMAPbSnI_3$, (Figure 3.1

(a)), which further supports the occurrence of alloy fluctuations and segregation in this specific system [27-29].

3.3 Linewidth Analysis of Temperature Dependent Photoluminescence

In this section, the emission and physical properties of metal-halide perovskites are investigated by analyzing the temperature-dependent photoluminescence (TD PL) and evaluating the full-width-at-half-maximum (FWHM) as a function of temperature. By examining the FWHM of this temperature-dependent PL, parameters that describe the electron-phonon and impurity-related interactions can be determined. The PL linewidth broadening as a function of temperature is calculated using [32,33]:

$$\Gamma_{tot}(T) = \Gamma_0 + \Gamma_{LA} + \Gamma_{LO}\left[\exp\left(\frac{E_{LO}}{k_B T}\right) - 1\right] + \Gamma_{imp}\exp\left(-\frac{E_x}{k_B T}\right) \qquad (3.1)$$

This formula takes into account temperature-independent inhomogeneous broadening (Γ_0), broadening due to acoustic phonons (Γ_{LA}), those due to optical phonons (Γ_{LO}), broadening due to ionized impurities scattering (Γ_{imp}), as well as the energy of the optical phonons (E_{LO}) and ionized impurities (E_x)[33].

The most significant parameters (Γ_0, Γ_{LO}, and E_{LO}) are presented in Table I. The contribution of Γ_{LA}, Γ_{imp}, and E_x are observed to be negligible and are

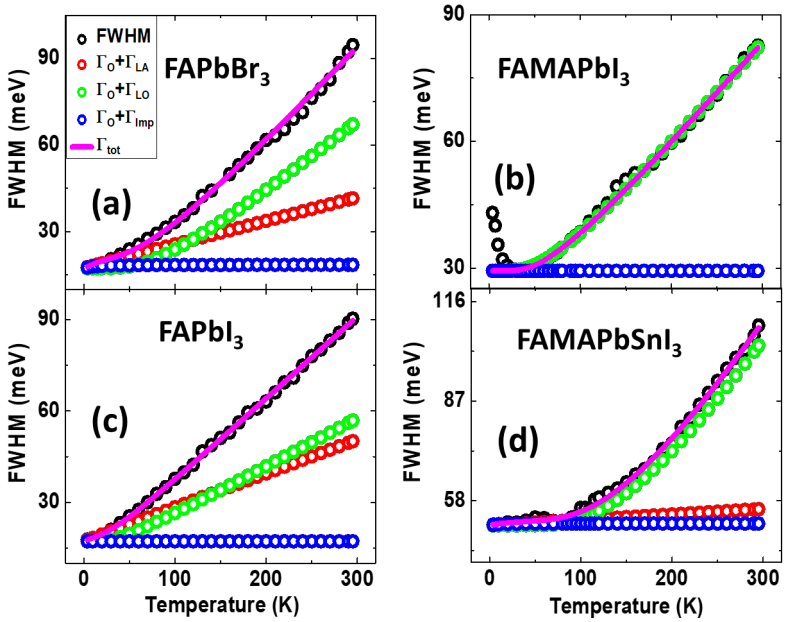


Figure 3.2: (a) Full-Width at Half Maximum (FWHM) values between 4.2 K to 295 K for the four different perovskite thin films: (a) $FAPbBr_3$, (b) $FAMAPbI_3$, (c) $FAPbI_3$, and (d) $FAMAPbSnI_3$. The solid purple line represents the fit to the data, while the contributions of various coupling parameters described in Eq. (3.1) are shown in red for $\Gamma_0 + \Gamma_{LA}$, green for $\Gamma_0 + \Gamma_{LO}$, and blue for $\Gamma_0 + \Gamma_{imp.}$.

therefore not considered here [57]. While this analysis is helpful in terms of identifying trends and qualitative physical behavior, it is important to note that it does not address complications, such as grain boundaries, etc. that could affect phonon propagation and thus influence some of the parameters.

Figure 3.2 shows the experimental FWHM (solid black circles) fit using equation 3.1 (purple solid line). Also shown are the individual contributions of $\Gamma_0 + \Gamma_{LA}$ (red open circles), $\Gamma_0 + \Gamma_{LO}$ (green open circles), and $\Gamma_0 + \Gamma_{imp}$ (blue open

Table 3.1: Extracted broadening parameters from the TDPL shown in Figure 3.1 for the following perovskites:

Perovskite	Γ_0 (meV)	Γ_{LO} (meV)	E_{LO} (meV)
$FAMAPbSnI_3$	51 ± 6	204 ± 20	40 ± 4
$FAPbI_3$	17.2 ± 2	16 ± 4	8.5 ± 4
$FAMAPbI_3$	29.3 ± 9	43 ± 4	15 ± 3
$FAPbBr_3$	17.3 ± 8	59 ± 19	20 ± 10

circles)) as a function of temperature for $FAPbBr_3$, $FAMAPbI_3$, $FAPbI_3$, and $FAMAPbSnI_3$ respectively. Only the dominant peak in the PL (Figure 3.1) - P1 is considered when evaluating the thermal broadening of the PL.

In MHP, the metal cation and halide anion are arranged in a crystal lattice in such a way that they form alternating planes. This structure gives rise to a strong polar nature in these materials [58]. The Fröhlich coefficient, or LO phonon coupling, is a measure of the interaction between the charge carriers and optical phonons in the crystal. As the temperature increases the crystal vibrates and this oscillation in the lattice induces a local electric field that is created via the oscillating dipole moment between the consistent atoms, the amplitude of which increases with temperature. Since MHPs are strongly polar materials such carrier-LO phonon coupling dominants the carrier-lattice interactions and transport in these systems [58].

All the parameters extracted from the FWHM broadening analysis are summarized in Table 3.1. Usually, the carrier thermalization properties, which are of interest in this study, and fundamental carrier mobility of the polar system are determined by the Fröhlich coupling coefficient (Γ_{LO}) and the LO phonon energy (E_{LO}). Here, the E_{LO} reported in Table 3.1 for the systems assessed are consistent with literature values [34,35-37] and increases with the addition of the lighter element Sn in $FAMAPbSnI_3$. When considering the respective Fröhlich coupling coefficients (Γ_{LO}), the Γ_{LO} of $FAPbI_3$ is less than half the strength of the other metal-halide perovskites assessed. This is consistent with the reduced ionicity of PbI relative to PbBr, as reflected in the extracted values of $FAPbI_3$ (16 ± 4 meV) and $FAPbBr_3$ (59 ± 19 meV), respectively.

However, in the case of the Sn-based perovskite there is an (Table 3.1) unexpectedly high value of Γ_0 (51 ± 6 meV), which is over three times larger than that of $FAPbBr_3$ and $FAPbI_3$. This is believed to be caused by Sn oxidation and the resulting strain and defects and therefore the subsequent low-energy tail states that are associated with the difficulty in stabilizing the Sn-based perovskites. As such this large Γ_0 likely does not reflect the intrinsic strength of electron-phonon coupling in these systems [31,38-40].

In evaluating the increase in FWHM above 150 K (Figure 3.2, Table 3.1), the Sn-based perovskite has the smallest increase in linewidth (34 meV), while

the Br-based perovskite has the largest increase (55 meV). Interestingly, the FAMA sample has a slightly lower FWHM at room temperature than the FA sample. While the extracted Γ_0 values for $FAPbBr_3$ and $FAPbI_3$ are consistent with the literature [34-37], the PbBr sample is slightly narrower than previous work [35]. This is attributed to the increased separation between the ground state transition (P1) and the defect state (P2) in $FAPbBr_3$ or ΔE_{p1-p2}, which reduces the convolution of these two transitions and the associated broadening of the dominant emission peak. This is also likely the main reason for the slightly larger Γ_0 in $FAPbI_3$ and $FAMAPbI_3$, which have a smaller E_{p1-p2} (as discussed in Figure 3.1 above) and, therefore, a greater convolution between P1 and P2.

3.4 Transmission

To elucidate a deeper understanding into the nature of the transitions observed in PL for the different systems studied, temperature-dependent transmission spectroscopy is performed to evaluate the absorption profile of the various MHPs assessed. A decrease in the transmission signal is typically linked with absorption from a transition in the materials with the strength of this absorption related to the density of states of the complex, which is therefore dominated by the fundamental band gap of a bulk semiconductor. Smaller effects are observed for defect complexes and impurities that typically are much less dense in concentration [42].

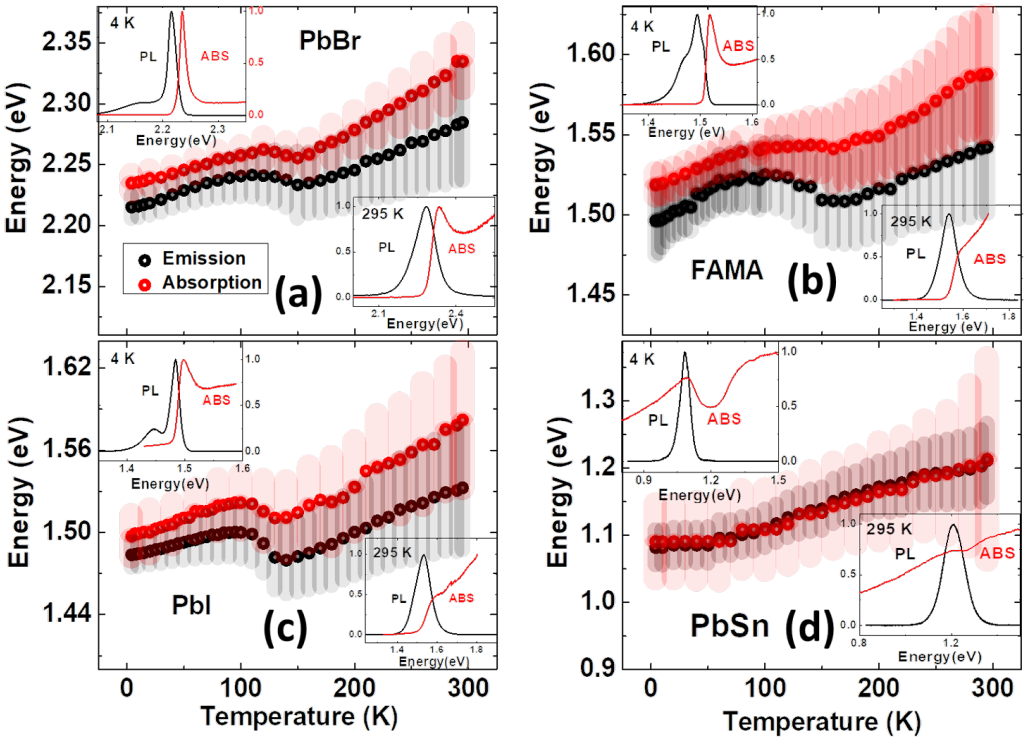


Figure 3.3: Comparison of peak PL energy gap (black circles) and energy from transmission spectra (red circles) for four perovskite thin films: $FAPbBr_3$, $FAMAPbI_3$, $FAPbI_3$, and $FAMAPbSnI_3$, from 4.2 to 295 K. Insets show PL (black) and absorbance (red) spectra at 4 K (upper) and 295 K (lower).

Figure 3.3 shows the results of a comparison of the absorption (transmission) and PL for (a) $FAPbBr_3$, (b) $FAMAPbI_3$, (c) $FAPbI_3$, and (d) $FAMAPbSnI_3$. The red dots indicate the excitonic absorption feature, while the black dots represent the effective band gap of optical transitions from PL. The shaded regions in the figure correspond to the FWHM, which has been extracted using Gaussian and Voigt fitting of the respective spectra. Here, the FWHM can be seen to increase

with increasing temperature, indicating increasing inhomogeneity in the systems at higher temperature. The upper insets of all Figure(s) 3.3 show a comparison of the absorption and PL spectra at 4.2 K, while the lower insets display the comparison at 295 K.

It is important to notice that the excitonic absorption is more visible at low temperatures and the onset of excitonic absorption can be seen to match the peak of the dominant P1 transition in the PL for all the perovskite thin films assessed (Figure 3.1), while the low energy feature P2 is observed to be much weaker than P1, indicating that the density of states of P2 is lower than that of P1 in the pure PbI cases (Figure 3.3 (a), (b), and (c)).

It should be noted that the absorption resonance in $FAPbBr_3$ and $FAMAPbSnI_3$ are evident even at room temperature. However, in the cases of $FAPbI_3$ and $FAMAPbI_3$, the exciton is quenched at $T = 150$ K and the absorption of the continuum is dominant at room temperature. This is consistent with the relative binding energies of the respective systems that are proportional to the first order to the band gap [43,44], and is typical of Wannier-Mott excitons found in polar semiconductors. The Br-based perovskite shows a binding energy comparable to that observed at room temperature, while the I-based samples have a binding energy of ~ 160 K or less, consistent with previous findings [43,45,46].

Specifically, fitting of the excitonic absorption at low temperatures using the

Elliott model [58] introduced in Chapter 2, shows the binding energy of Br based sample to be around the room temperature ($\sim$ 25 meV) while for PbI it is around $<$ 160 K ($\sim$ 12 meV), which is consistent with the quenching of the excitonic feature in the temperature dependent absorption (Figure(s) 3.3) and previous values reported in the literature [16]. However, the Sn- based perovskite show the resonance in the absorption spectra even at room temperature despite the relatively low reported binding energy of 10-15 meV, which we would expect to ionize the exciton at $\sim$ 170 K. While previous studies have reported a wide range of exciton binding energies in metal lead halide perovskites - due to indirect method of exciton binding energy extraction - our results falls well within the range of reported values [47].

A comparison of the emission peak with the absorption for $FAPbBr_3$ with respect to that of $FAPbI_3$ also shows the expected larger exciton binding energy and ionicity of the Br-based systems (20 meV) than that of the I-based materials (12 meV), which illustrates the nature of carrier-phonon interactions of MHP and plays a significant role in their properties, reflected in the relative Stokes shift observed for these systems.

The Stokes shift, which is the difference between the absorption edge and dominant emission peak, for $FAMAPbI_3$ (Figure 3.3 (c)) is unexpectedly large at 20 meV when compared to the $FAPbI_3$ perovskite, which has the same inorganic framework. This is attributed to the fine structure around the band edge and the

contribution to the linewidth of the PL that likely screens the true bandgap of $FAMAPbI_3$. In Figure(s) 3.3 as the temperature increases, the Stokes shift of (a) $FAPbI_3$ increases to 50 meV at 295 K. For (b) $FAMAPbI_3$ and (c) $FAPbBr_3$, the low-temperature Stokes shifts remain constant until $\sim$ 150 K, and then they also increase to $\sim$ 50 meV at 295 K.

In conventional III-V systems, a Stokes shift usually indicates the presence of localization and a perturbation in the emission related the relative binding energy of the complex responsible. This is reflected by the difference (reduced energy) in emission as compared to the free carrier emission/absorption at the continuum. While this also occurs in the metal halide perovskite systems, additional and significant contributions to the Stokes are also caused by changes in the lattice structure and the formation polarons that lead to a decrease in the energy of emitted light. In Figure 3.3, as the temperature increases the Stokes shift also increases suggesting that the Fröhlich interaction in the systems studied is temperature-dependent and becomes stronger at higher temperatures. This phenomenon has been observed by many groups studying the MHP and have been related to the temperature dependence of the dielectric constant and Fröhlich coupling, which are influenced by the dynamic nature of the lattice in these soft materials [48].

The Sn-based perovskite studied here, $FAMAPbSnI_3$ exhibits several interesting characteristics one of which is the (lack of any) difference between the

peak PL emission and absorption edge across all temperatures (see Figure 3(d)). Examining the insets to Figure 3(d), the emission and absorption spectra at 4.2 K and 295 K, respectively, overlap significantly. This apparent overlap is attributed to the disorder and inhomogeneous nature of this system that screens the true Stokes shift in these Sn-based samples.

Evidence of the disorder in these samples is seen by the strong low-energy tail observed in the absorption spectrum of this material, even at high temperatures. This tail is related to sub-gap free carrier absorption located approximately 100 meV below the band edge. This is consistent with previous work [49] that suggest that shifts in the PL and absorption represent strong subband gap absorption in Sn-based system, which is typically larger than k_BT. This reflects the large p-type doping which is a characteristics of the non-idealities of the system. As such, the relatively large low-temperature FWHM of approximately 70 meV for $FAMAPbSnI_3$ as shown in the shaded area in Figure 3(d) serves to screen the true Stokes shift in this material since it exceeds the binding energy of these systems ($\sim$ 10 – 15 meV [34]).

In the case of the three Pb-based films there is an excitonic feature in the transmission (absorption) that is within 20 meV of the band edge, indicative of the strength of the exciton binding energy in these materials [17]. Additionally, these systems exhibit increased polaron behavior, increasing the relative Stokes shift with increasing temperature as the excitons are ionized and charge carrier–phonon

interaction increases [40].

However, the in the case of the mixed Pb-Sn sample there is a noticeable difference in behavior in Figure 3.3. There is also an absence of any Stokes shift in the optical properties, nor a shift in energy associated with a low-temperature crystal phase transition for the FAMAPbSnI_3 sample. The below-band-gap absorption, clearly visible in the upper 4.2 K inset $\sim$ 100 meV below the band edge in this sample. These properties are clear evidence of strong inhomogeneity and disorder in the Sn-based samples that dominate the behavior of the PbSn film in CW measurements. To further understand the dynamics of these films and compare and contrast the trends across these four systems assessed transient absorption measurements were performed and are discussed in Chapter 4.

3.5 Conclusion

Analysis of the temperature-dependent (4 - 295 K) PL and transmission spectra have been conducted on several complementary metal-halide perovskite systems, varying the A, B and/or X compositions to determine their effect on the properties of these materials. Low-temperature results revealed subtle underlying changes that are often obscured at room temperature in the MHPs. Specifically, replacing the organic cation formamidinium (FA) with formamidinium-methylammonium (FAMA) in lead iodide (PbI_3) perovskite resulted in a more complex low-temperature spectrum for the samples that contained FAMA. The

overall Stokes shift of FA- and FAMA- systems was similar and consistent with that of the $PbBr_3$ system at room temperature. The details of the difference in the PL and absorption are the result of different processes, governed by the interaction strength of LO phonons (Γ_{LO}), phonon energy E_{LO}, the exciton binding energy and availablity of free carriers.

The only exception to the expected behavior was the Sn-based $FAMAPbSnI_3$ sample, which showed a lack of Stokes shift, large FWHM and subgap PL. The apparent lack of Stokes shift is attributed to the rather large low-temperature broadening Γ_0 associated with the increased inhomogeneities from Sn^{4+} and the presence of a large unintentional background doping, which is a characteristic of these systems.

3.6 References

1. D. B. Mitzi, Synthesis, structure, and properties of organicinorganic perovskites and related materials, in Progress in Inorganic Chemistry (Wiley, New York, 1999), pp. 1–121.

2. S. A. Kulkarni, T. Baikie, P. P. Boix, N. Yantara, N. Mathews, and S. Mhaisalkar, J. Mater. Chem. A 2, 9221 (2014).

3. F. Deschler, M. Price, S. Pathak, L. E. Klintberg, D.-D. Jarausch, R. Higler, S. Hüttner, T. Leijtens, S. D. Stranks, H. J. Snaith, M. Atatüre, R. T. Phillips, and R. H. Friend, J. Phys. Chem. Lett. 5, 1421 (2014).

4. Z.-K. Tan, R. S. Moghaddam, M. L. Lai, P. Docampo, R. Higler, F. Deschler, M. Price, A. Sadhanala, L. M. Pazos, D. Credgington, F. Hanusch, T. Bein, H. J. Snaith, and R. H. Friend, Nat. Nanotechnol. 9, 687 (2014).

5. S. D. Stranks and H. J. Snaith, Nat. Nanotechnol. 10, 391 (2015).

6. H. Deng, X. Yang, D. Dong, B. Li, D. Yang, S. Yuan, K. Qiao, Y.-B. Cheng, J. Tang, and H. Song, Nano Lett. 15, 7963 (2015).

7. G. Xing, N. Mathews, S. Sun, S. S. Lim, Y. M. Lam, M. Grätzel, S. Mhaisalkar, and T. C. Sum, Science 342, 344 (2013).

8. M. B. Price, J. Butkus, T. C. Jellicoe, A. Sadhanala, A. Briane, J. E. Halpert, K. Broch, J. M. Hodgkiss, R. H. Friend, and F. Deschler, Nat. Commun. 6, 8420 (2015).

9. J. M. Frost, L. D. Whalley, and A. Walsh, ACS Energy Lett. 2, 2647 (2017).

10. J. Fu, Q. Xu, G. Han, B. Wu, C. H. A. Huan, M. L. Leek, and T. C. Sum, Nat. Commun. 8, 1300 (2017).

11. H.-H. Fang, S. Adjokatse, S. Shao, J. Even, and M. A. Loi, Nat. Commun. 9, 243 (2018).

12. J. Tong, Z. Song, D. H. Kim, X. Chen, C. Chen, A. F. Palmstrom, P. F. Ndione, M. O. Reese, S. P. Dunfield, O. G. Reid, J. Liu, F. Zhang, S. P. Harvey, Z. Li, S. T. Christensen, G. Teeter, D. Zhao, M. M. Al-Jassim, M. F. A. M. van Hest, M. C. Beard, S. E. Shaheen, J. J. Berry, Y. Yan, and K. Zhu, Science 364, 475 (2019).

13. Z. Guo, Y. Wan, M. Yang, J. Snaider, K. Zhu, and L. Huang, Science 356, 59 (2017).

14. M. Li, J. Fu, Q. Xu, and T. C. Sum, Adv. Mater. 31, 1802486 (2019).

15. J. W. M. Lim, D. Giovanni, M. Righetto, M. Feng, S. G. Mhaisalkar, N. Mathews, and T. C. Sum, J. Phys. Chem. Lett. 11, 2743 (2020).

16. J. S. Manser and P. V. Kamat, Nat. Photonics 8, 737 (2014).

17. Y. Yang, D. P. Ostrowski, R. M. France, K. Zhu, J. van de Lagemaat, J. M. Luther, and M. C. Beard, Nat. Photonics 10, 53 (2015).

18. B. Anand, S. Sampat, E. O. Danilov, W. Peng, S. M. Rupich, Y. J. Chabal, Y. N. Gartstein, and A. V. Malko, Phys. Rev. B 93, 161205(R) (2016).

19. J. Yang, X. Wen, H. Xia, R. Sheng, Q. Ma, J. Kim, P. Tapping, T. Harada, T.W. Kee, F. Huang, Y.-B. Cheng, M. Green, A. Ho Baillie, S. Huang, S. Shrestha, R. Patterson, and G. Conibeer, Nat. Commun. 8, 14120 (2017).

20. T. R. Hopper, A. Gorodetsky, J. M. Frost, C. Müller, R. Lovrincic, and A. A. Bakulin, ACS Energy Lett. 3, 2199 (2018).

21. Y. H. Chang, C. H. Park, and K. Matsuishi, J. Korean Phys. Soc. 44, 889 (2004).

22. M. R. Filip, C. Verdi, and F. Giustino, J. Phys. Chem. C 119, 25209 (2015).

23. J. C. Brauer, D. Tsokkou, S. Sanchez, N. Droseros, B. Roose, E.Mosconi, X. Hua, M. Stolterfoht, D. Neher, U. Steiner, F. De Angelis, A. Abate, and N. Banerji, J. Chem. Phys. 152, 104703 (2020).

24. J. Neugebauer and C. G. Van de Walle, Phys. Rev. B 51, 10568 (1995).

25. Y. Jiao, S. Yi, H.Wang, B. Li, W. Hao, L. Pan, Y. Shi, X. Li, P. Liu, H. Zhang, C. Gao, J. Zhao, and J. Lu, Adv. Funct. Mater. 31, 2006243 (2021).

26. W. P. D.Wong, J. Yin, B. Chaudhary, X. Y. Chin, D. Cortecchia, S.-Z. A. Lo, A. C. Grimsdale, O. F. Mohammed, G. Lanzani, and C. Soci, ACS Materials Lett. 2, 20 (2020).

27. M. T. Klug, R. L. Milot, J. B. Patel, T. Green, H. C. Sansom, M. D. Farrar, A. J. Ramadan, S. Martani, Z. Wang, B. Wenger, J. M. Ball, L. Langshaw,

A. Petrozza, M. B. Johnston, L. M. Herz, and H. J. Snaith, Energy Environ. Sci. 13, 1776 (2020).

28. L. E. Mundt, J. Tong, A. F. Palmstrom, S. P. Dunfield, K. Zhu, J. J. Berry, L. T. Schelhas, and E. L. Ratcliff, ACS Energy Lett. 5, 3344 (2020).

29. R. Prasanna, T. Leijtens, S. P. Dunfield, J. A. Raiford, E. J. Wolf, S. A. Swifter, J. Werner, G. E. Eperon, C. de Paula, A. F. Palmstrom, C. C. Boyd, M. F. A. M. van Hest, S. F. Bent, G. Teeter, J. J. Berry, and M. D. McGehee, Nature Energy 4, 939 (2019).

30. F. Brivio, A. B. Walker, and A. Walsh, APL Mater. 1, 042111 (2013).

31. C. C. Stoumpos, C. D. Malliakas, and M. G. Kanatzidis, Inorg. Chem. 52, 9019 (2013).

32. J. Lee, E. S. Koteles, and M. O. Vassell, Phys. Rev. B 33, 5512 (1986).

33. J. V. D. Veliadis, J. B. Khurgin, Y. J. Ding, A. G. Cui, and D. S. Katzer, Phys. Rev. B 50, 4463 (1994).

34. A. D. Wright, C. Verdi, R. L. Milot, G. E. Eperon, M. A. Pérez Osorio, H. J. Snaith, F. Giustino, M. B. Johnston, and L. M. Herz, Nat. Commun. 7, 11755 (2016).

35. L. M. Herz, Annu. Rev. Phys. Chem. 67, 65 (2016).

36. C. M. Iaru, J. J. Geuchies, P. M. Koenraad, D. Vanmaekelbergh, and A. Y. Silov, ACS Nano 11, 11024 (2017).

37. J. Huang, Y. Yuan, Y. Shao, and Y. Yan, Nat. Rev. Mater. 2, 17042 (2017).

38. N. K. Noel, S. D. Stranks, A. Abate, C. Wehrenfennig, S. Guarnera, A.-A. Haghighirad, A. Sadhanala, G. E. Eperon, S. K. Pathak,M. B. Johnston, A. Petrozza, L. M. Herz, and H. J. Snaith, Energy Environ. Sci. 7, 3061 (2014).

39. F. Hao, C. C. Stoumpos, D. H. Cao, R. P. H. Chang, and M. G. Kanatzidis, Nat. Photonics 8, 489 (2014).

40. E. S. Parrott, R. L. Milot, T. Stergiopoulos, H. J. Snaith, M. B. Johnston, and L. M. Herz, J. Phys. Chem. Lett. 7, 1321 (2016).

41. R. F. Moral, J. C. Germino, L. G. Bonato, D. B. Almeida, E. M. Therézio, T. D. Z. Atvars, S. D. Stranks, R. A. Nome, and A. F. Nogueira, Adv. Opt. Mater. 8, 2001431 (2020).

42. H. Esmaielpour, V. R. Whiteside, S. Sourabh, G. E. Eperon, J. T. Precht, M. C. Beard, H. Lu, B. K. Durant, and I. R. Sellers, J. Phys. Chem. C 124, 9496 (2020).

43. A. Miyata, A. Mitioglu, P. Plochocka, O. Portugall, J. T.-W. Wang, S. D. Stranks, H. J. Snaith, and R. J. Nicholas, Nat. Phys. 11, 582 (2015).

44. K. Galkowski, A. Mitioglu, A. Miyata, P. Plochocka, O. Portugall, G. E. Eperon, J. T.-W. Wang, T. Stergiopoulos, S. D. Stranks, H. J. Snaith, and R. J. Nicholas, Energy Environ. Sci. 9, 962 (2016).

45. R. J. Elliott, Phys. Rev. 108, 1384 (1957).

46. J. Even, L. Pedesseau, and C. Katan, J. Phys. Chem. C 118, 11566 (2014).

47. M. Konstantakou and T. Stergiopoulos, J. Mater. Chem. A 5, 11518 (2017).

48. Y. Guo, O. Yaffe, T. Hull, J. Owen, D. Reichman, and L. Brus, Nat. Commun. 10, 1175 (2019).

49. J. Wong, S. T. Omelchenko, and H. A. Atwater, ACS Energy Lett. 6, 52 (2021).

50. G. Nazir, S.-Y. Lee, J.-H. Lee, A. Rehman, J.-K. Lee, S. I. Seok, and S.-J. Park, "Stabilization of Perovskite Solar Cells: Recent Developments and Future Perspectives", Adv. Mater., vol. 34, 2204380, 2022.

51. M. Chen, Y. T. Zou, L. Z. Wu, Q. Pan, D. Yang, H. C. Hu, Y. S. Tan, Q. X. Zhong, Y. Xu, H. Y. Liu, B. Q. Sun, and Q. Zhang, "Solvothermal synthesis of high-quality all-inorganic cesium lead halide perovskite nanocrystals: from nanocube to ultrathin nanowire," Adv. Funct. Mater. 27, 1701121 (2017).

52. G. C. Xing, N. Mathews, S. Y. Sun, S. S. Lim, Y. M. Lam, M. Grätzel, S. Mhaisalkar, and T. C. Sum, "Long-range balanced electron- and hole-transport lengths in organic-inorganic CH3NH3PbI3," Science 342, 344–347 (2013).

53. J. Burschka, N. Pellet, S.-J. Moon, R. Humphry-Baker, P. Gao, M. K.

Nazeeruddin, and M. Grätzel, "Sequential deposition as a route to high-performance perovskite-sensitized solar cells," Nature 499, 316–319 (2013).

54. Y. Wang, et al., "Ionic behavior of organic–inorganic metal halide perovskite based metal-oxide-semiconductor capacitors", Physical Chemistry Chemical Physics, vol. 19, no. 20, pp. 13002-13009, 2017.

55. J. I. Pankove, "Optical Processes in Semiconductors," Dover Publications, Inc., New York, 1975. (Unabridged republication of the work originally published by Prentice-Hall, Inc., 1971).

56. N. Falsini, G. Roini, A. Ristori, N. Calisi, F. Biccari, and A. Vinattieri, "Analysis of the Urbach tail in cesium lead halide perovskites", Journal of Applied Physics, vol. 131, 010902, 2022. https://doi.org/10.1063/5.0076712

57. S. Sourabh, V. R. Whiteside, I. R. Sellers, Y. Zhai, K. Wang, M. C. Beard, V. Yeddu, M. T. Bamidele, and D. Y. Kim, Phys. Rev. Mater. 5, 095402 (2021).

58. D'Innocenzo, V. (2015). Photophysics of 3D lead halide perovskite semiconductors: Light absorption and Luminescence [Ph.D., Politecnico di Milano, Dipartimento di Fisica]

59. Yang, Y., Ostrowski, D., France, R. et al. Observation of a hot-phonon bottleneck in lead-iodide perovskites. Nature Photon 10, 53–59 (2016). https://doi.org/10.1038/nphoton.2015.213

60. C.R. Brown, et al., "Potential of High-Stability Perovskite Solar Cells for Low-Intensity–Low-Temperature (LILT) Outer Planetary Space Missions", ACS Applied Energy Materials, vol. 2, no. 1, pp. 814-821, 2019.

61. C. R. Brown, N. J. Estes, V. R. Whiteside, B.Wang, K. Hossain, T. D. Golding, M. Leroux, M. Al Khalfioui, J. G. Tischler, C. T. Ellis, E. R. Glaser, and I. R. Sellers, RSC Adv. 7, 25353 (2017)

Chapter 4

Ultrafast Transient Absorption: Thin film metal halide perovskites

4.1 Introduction

In Chapter 3, we observed that the four material systems analyzed displayed differences in optical properties, such as exciton binding energy, electron-phonon coupling strength, ionicity, and polaronic nature, based on continuous wave (CW) absorption and temperature-dependent photoluminescence measurements. In this chapter, we will address a more fundamental question: why do perovskites exhibit slow thermalization? To understand this phenomenon, we will employ transient absorption (TA) measurements (see Chapter 2, section 2.5), which are a powerful tool for assessing carrier dynamics in semiconductors [1,6] and will be used here to further elucidate the properties of the four materials assessed under steady-state conditions in Chapter 3.

Recent transient absorption (TA) studies have indicated that metal halide perovskites exhibit slower rates of hot carrier cooling [2] compared to GaAs under similar excitation conditions [4,6]. An example of this observation is illustrated in Figure 4.1.

A typical TA spectrum is shown and described in Figure 4.1, and is used to describe features typically observed with regard to metal halide perovskites

(MHPs).A TA spectrum can display several characteristic features that describe system dynamics but can be broadly split into three distinct regions:

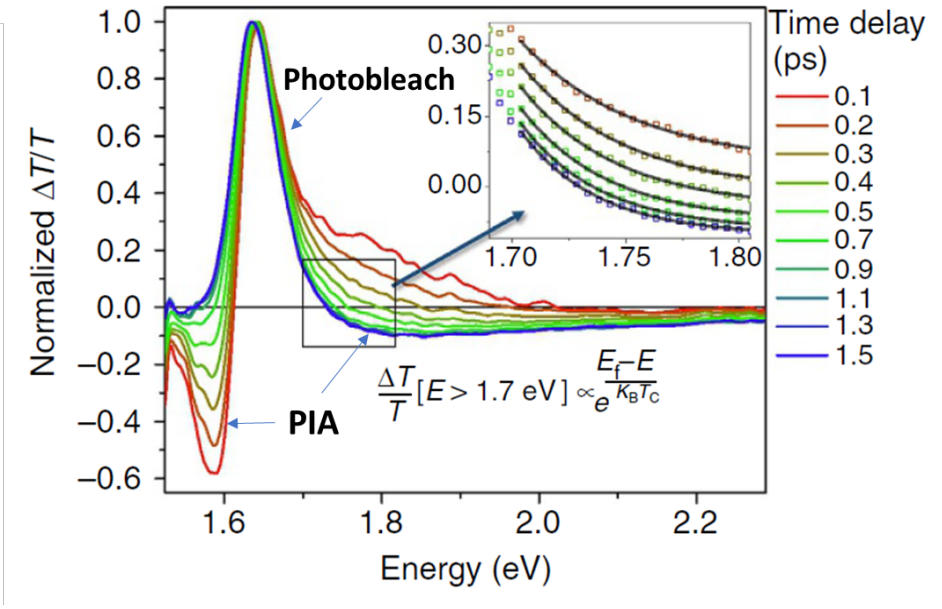


Figure 4.1: Typical Normalized TA spectra of $CH_3NH_3PbI_3$ excited with a 2.25 eV pump pulse. Inset: Cooling rates were determined using a global fit of the high-energy tail (between E = 1.7 and 1.85 eV) of each timeslice to a Boltzmann distribution.[2]

The first region, known as photoinduced absorption (PIA $\sim$ 1.6 eV), appears here at short times ($\sim <$ 1.3-1.5 ps) for photon energies less than the band gap. This effect arises due to the exciton Stark shift and broadening [1]. When light is absorbed by a metal-halide perovskite, excitons are generated. Although excitons are neutral particles, they are composed of an electron-hole pair that is bound together by the Coulomb interaction, which are influenced by external electric

fields provided by the absorbed light. This in turn affects the energy levels of the excitons, causing them to shift and broaden. This is known as the "optical Stark effect" and can cause an increase in absorption in the energy range just below the band gap, inducing a photoinduced absorption (PIA) effect.

The second region, known as photobleach region (positive transmission signal in Figure 4.1), occurs due to a reduction (or bleach) in absorption as the result of state filling at the band-edge by photogenerated carriers. This removes access to unoccupied states and can result in slight increase in the optical band gap known as a Moss-Burstein shift [6]. This photobleaching is observed in the TA spectrum as a dip in absorption (or peak in transmission signal) (Figure 4.1) at the exciton energy [6].

The third region is located at high energies as indicated by the PIA > 1.7 eV in Figure 4.1, and is characterized by a decrease in the photo bleach as carriers cool at longer time scales ($\sim$ 1.5 ps). In this region, features similar to PIA from the high energy tail are dominated by the contribution or a change upon photoexcitation of the material's refractive index, which changes (significantly in the MHP perovskites) due to the high free carrier absorption at longer delay times that results in a dynamic change in the materials dielectric constant [1,6].

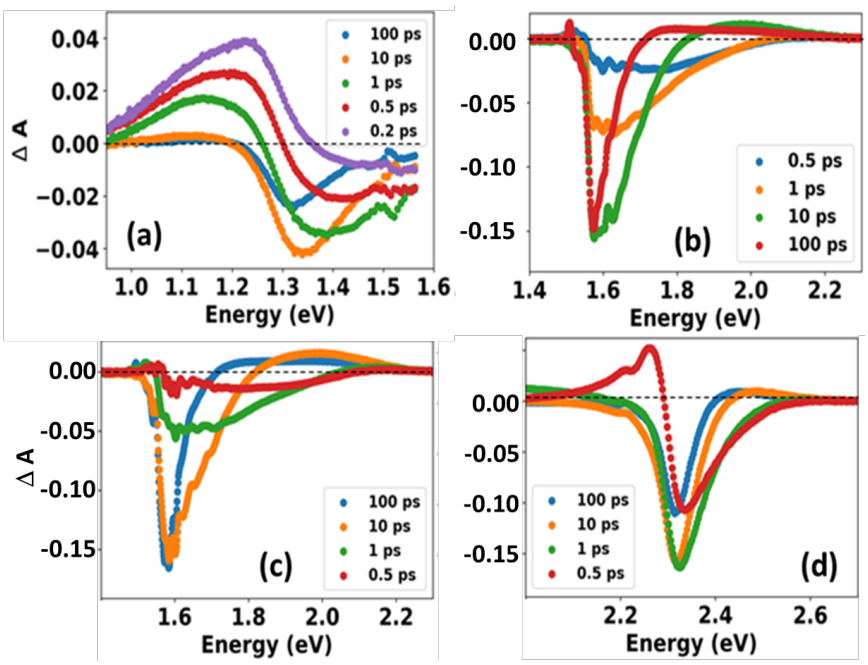


Figure 4.2: The transient absorption measurement of ΔA as a function of energy at room temperature for delay times ranging from 0.2/0.5 to 100 ps (color coded) for four types of perovskite thin films: (a) $FAMAPbSnI_3$, (b) $FAPbI_3$, (c) $FAMAPbI_3$, and (d) $FAPbBr_3$. [32]

4.2 Experimental Result and Discussion

Upon initial observation of the TA spectra depicted in Figure 4.2 for $FAMAPbSnI_3$ (a), $FAPbI_3$ (b), $FAMAPbI_3$ (c), and $FAPbBr_3$ (d), notable distinctions are apparent. All four films display low energy photoinduced absorption at very short time delays (< 1 ps) and exciton/band-gap photobleaching. Also, a high energy photoinduced absorption like feature within 250 meV of the photobleach minima is present in all four samples, except the Sn based perovskite. The extent and intensity of bleach at short delay times vary significantly across the samples, with the I-containing films (Figure 4.2 (b,c)) displaying more significant bleach when

compared to the Br film (Figure 4.2 (d)).

Additionally, a blueshift in energy is apparent at the maximum intensity of the exciton bleach energy in all samples as shown in Figures 4.2 (a) to 4(d). At $\sim$ 0.5 ps, a low energy PIA occurs, which is limited in the two I - films (PbI and FAMA), due to the detector cut off. All the non Sn-based samples exhibit the onset of a Moss-Burstein shifted photo bleach, which evolves and redshifts within a few picoseconds ($< 10ps$) to reach an energy state, which is the convolution of excitonic absorption and fundamental bandgap. In the case of PbSn film (Figure 4.2 (a)), it takes more time to reach the stable energy position. Furthermore, all the Pb only (Figure 4.2 (b)-(d)) films exhibit a high energy PIA region within a few picoseconds (2 - 5 ps), which depends on carrier density and can be attributed to band-gap renormalization and a decreasing Moss-Burstein shift as delay time increases (t $>$ 5 ps), i.e. the effective band gap decreases. The PbSn film (Figure 4.2 (a)) does not display a high energy PIA region, unlike the other films (Figure 4.2 (b)-(d)). However, the signal for the PbSn film extends a further 250 meV away from the photo bleach minima at higher energy for the transients recorded after 10 ps and 100 ps, while in the case of the Sn-free films, this higher energy region displays high apparent PIA.

The most noticeable feature among all the samples is that the sample with Sn shows the strongest low energy PIA (Figure 4.25 (a)), which is consistent with the onset of subgap absorption observed in the transmission measurements (Chapter

3 - Section 3.4). Also, the exciton energy observed in transmission/absorption (Chapter 3 - Section 3.4) does not match the TA bleach ($\sim$ 1.33 eV) but the low energy PIA ($\sim$ 1.2 eV), while for all other pure Pb-based samples, the excitonic absorption feature contributes majorly to the TA photobleach (for example $FAPbI_3$).

TA, while providing considerable information with respect to carrier dynamics and redistribution, also allow the high-energy hot carrier relaxation to be probed. In such analysis, the formation of a Maxwell-Boltzmann distribution is assumed after rapid carrier-carrier interaction ($<$ 1-2 ps) [1,11], and the carrier temperature extracted at energies larger than the absorber band gap the generalized Planck's equation:

$$-\Delta A(E) = A_0(E)\left[\exp\left(-\frac{E}{k_B T_c}\right)\right] \tag{4.1}$$

where ΔA is the change in transient absorption, $A_0(E)$ is the absorptivity as a function of energy, k_B is Boltzmann's constant, and T_c represents the carrier temperature which can be determined by a linear fit of the high energy tail of the transient absorption spectra.

The TA effects, such as PIA and photobleaches discussed earlier (Figure 4.2), exhibit varying dependencies on time and carrier density. Therefore, it is crucial to analyze TA spectra with care when assessing the hot carrier dynamics as they comprise a complicated convolution of different processes, as discussed in recent

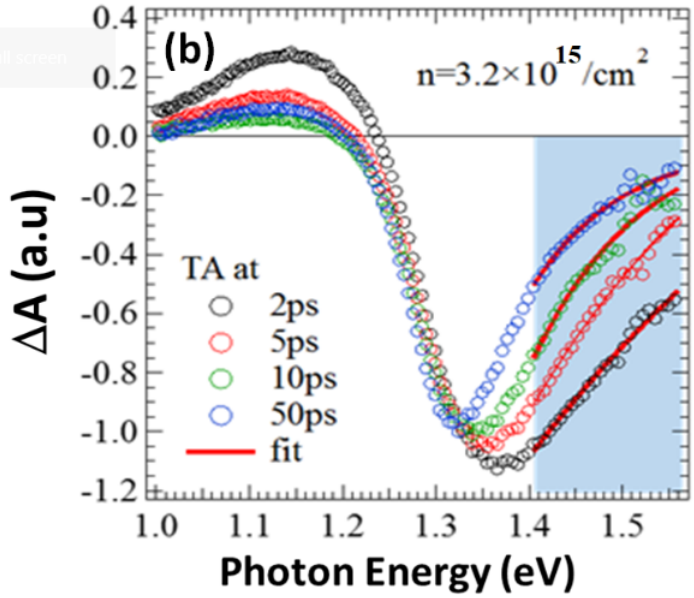


Figure 4.3: Hot carrier extraction in PbSn sample. The high-energy tails of TA curves at different time delays are analyzed using equation 4.1 to determine the hot carrier temperature.

studies by Yang *et al.*[6] and Lim *et al.*[5] However, these complexities are most prominent near the band edge, and hence the high energy tail provides a good qualitative estimation of the hot carrier dynamics.

In Figure 4.4, the time evolution of hot carrier temperatures for $FAPbI_3$, $FAMAPbI_3$, and $FAPbBr_3$ films is compared. These temperatures are extracted using Equation 4.1, as demonstrated in Figure 4.3, for the samples depicted in Figures 4.2 (b-d). Sn case is different and hence has been shown seperately (Figure 4.6 (d)). The dynamics are plotted on a logarithmic scale (Figure 4.6 (d)), starting from 1 ps, which represents the time frame where a global Maxwell-Boltzmann distribution is established.

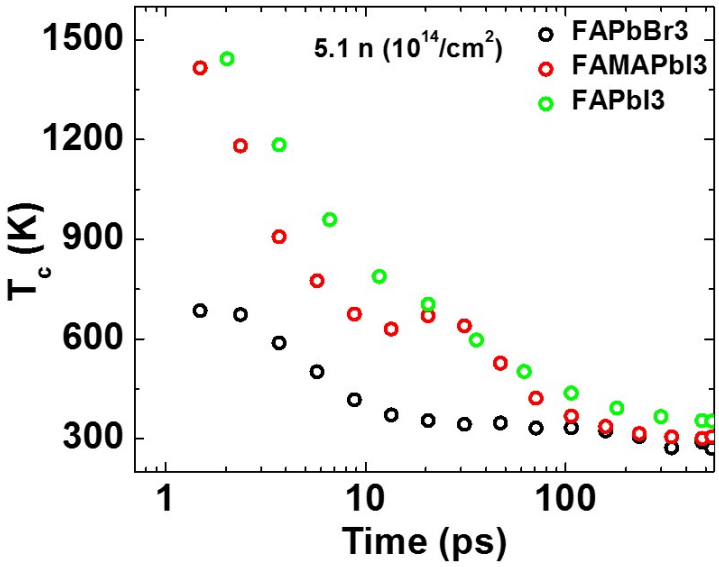


Figure 4.4: Variation of T_c with delay time at room temperature for three different perovskite thin films, namely $FAPbBr_3$ (black), $FAMAPbI_3$ (red), and $FAPbI_3$ (green).

When looking at systems containing lead iodide (PbI_3) with two different cations, FA and FAMA (Figure 4.2 (b,c)), the process of hot carrier cooling to equilibrium temperature (at 300 K) is quite similar. This is because both systems have a similar structure and energy gap, which leads to the creation of hot carriers with roughly the same excess energy when they are excited by a high-energy (400 nm) laser at the beginning of the process. On the other hand, $FAPbBr_3$ has a lower starting temperature for its carriers because it has a larger energy gap compared to the PbI_3 systems, which means less excess energy is created in the system upon ecitation

In all cases in Figure 4.4, for $t < 1\ ps$, the carrier distribution rapidly evolves

into a Maxwell-Boltzmann distribution via strong carrier-carrier interaction, resulting in a nonequilibrium hot carrier distribution ($T_c > T_L$). This is followed by Fröhlich coupling and hot LO phonon generation/emission $t > 1$ ps. This initial carrier-LO phonon interaction leads to a rapid carrier thermalization in the 1 - 10 ps timescale. In the MHPs this has been shown to be followed by a much slower thermalization rate typically on the 10-1000 ps timescale at higher excitation densities ($> 10^{13}$ cm^{-2}) [2,3,5,6], including in the pure-Pb and Sn-based perovskites studied here (as seen in Figure 4.4 and Figure 4.6 (d), respectively).

In Figure 4.5, it can be observed that the relaxation rate of $FAPbBr_3$ is greater than that of PbI_3 systems. This can be attributed to the increased ionicity of $PbBr_3$, which leads to stronger electron-phonon interaction for Br- based systems and, therefore, faster carrier relaxation [8]. While the initial thermalization of hot carriers in MHPs (and polar semiconductors, in general) is generally accepted to be the result of carrier-LO phonon interaction, the longer-lived regime ($t > 10$ ps) is less well understood. Recently, this was attributed to carrier heating via Auger processes [4] due to the high carrier concentrations required to produce this effect and inhibited Klemens processes [33].

However, since no significant effect is observed for different E_{ex}, E_g [53], or E_{LO}, when comparing the sample assessed here, which would be expected if Auger processes or decoupled optical to acoustic processes were dominant, an alternative explanation is proposed [32].

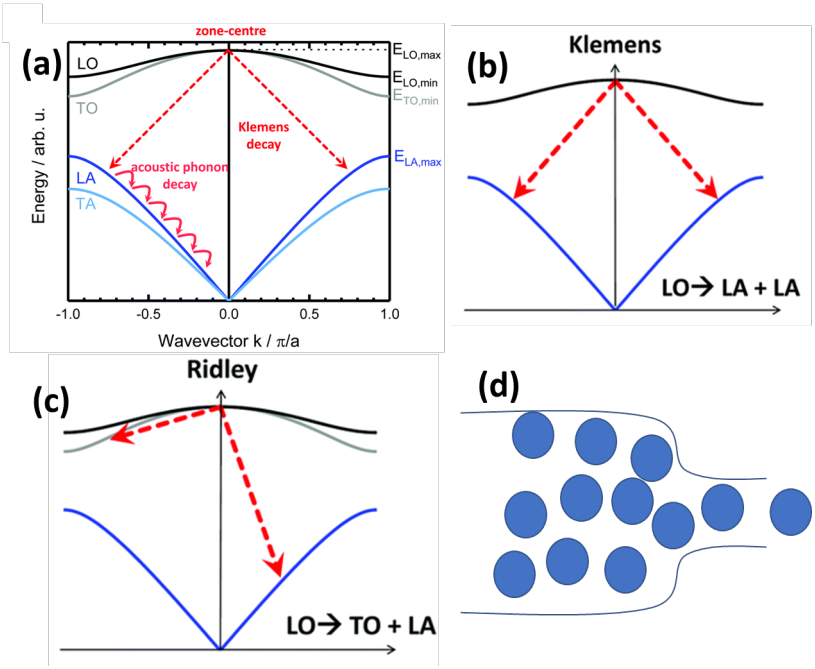


Figure 4.5: Schematic of various phonon decay channels: (a), (b), and (c) have been reproduced from [33]. (a,b) showcases the decay of the LO phonon through the Klemens route into 2 LA phonons. (c) illustrates both the Ridley (TA+LO) and Klemens routes of the LO phonon decay channel. Additionally, (d) presents a schematic representation of the phonon bottleneck effect resulting from the low thermal conductivity in the perovskite proposed here.

The thermalization of hot carriers and the dissipation of their energy via the emission of optical and acoustic phonons are described in Figure 4.5. Shortly after hot carrier generation, Fröhlich interactions occurs and hot LO phonons are generated at very short timescales ($t \sim 1$ ps). These non-equilibrium hot LO phonons then dissipate their excess energy via the emission of multiple longitudinal acoustic phonons, $t < 10$ ps (LA) via either the Klemens (LO = 2LA) [16] or

Ridley (LO = TO + LA) [17] process creating hot LA phonons. The LA phonons further dissipate the energy (heat) into the cold acoustic phonon bath, which is then transferred away via thermal conductivity.

Figure 4.5 shows the carrier relaxation mechanisms and phonon decay channels for traditional III-V semiconductors [25]. According to a previous study, the slowed thermalization of carriers in metal-halide perovskites may result from the decoupling of the dominant Klemens mechanism (Figure 4.5 (a,b)), [3] while the Ridley channel (Figure 4.5 (c)) remains strong due to the mixing of the transverse optical (TO) and longitudinal optical (LO) modes in the band structure. Thus, Ridley processes would be expected to dominate the dissipation of hot LO phonons in the absence of Klemens processes, facilitating the thermalization of hot carriers in the perovskites, in this case. However, an alternative explanation suggests that, although hot LO phonons can effectively couple to acoustic phonons via the Ridley mechanism [17], the dissipation of hot longitudinal acoustic (LA) phonons is hindered by the low thermal conductivity of halide perovskites [18-21]. This process is further supported by other recent work that suggests that the reabsorption of hot acoustic phonons can account for the slowed carrier cooling in metal-halide perovskites when the dissipation of hot acoustic modes is inhibited [7], this process is schematically shown in Figure 4.5 (d). The low thermal conductivity narrows the acoustic channel decay creating a bottleneck that results in slow thermalization due to the inhibited dissipation of heat from hot acoustic bath.

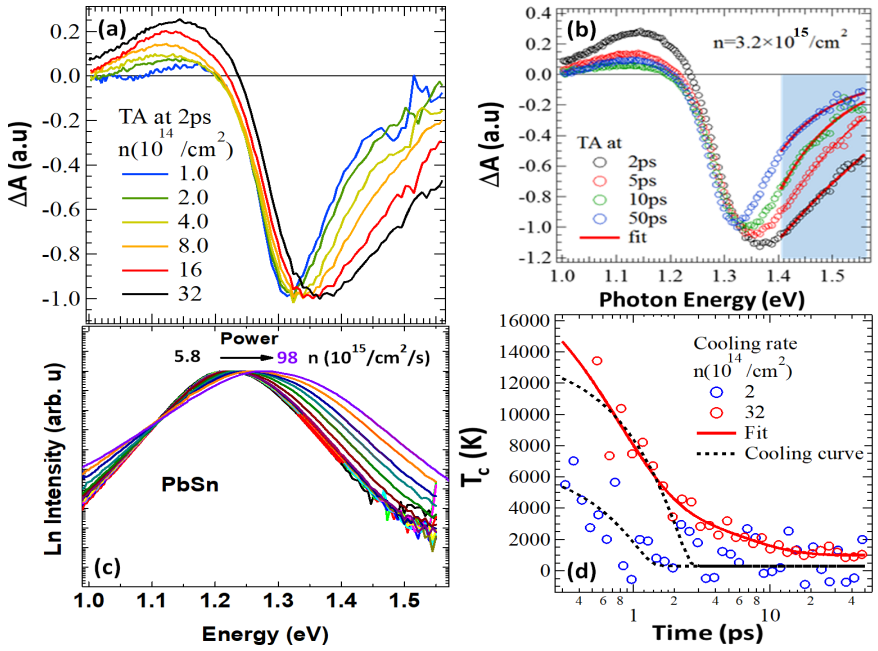


Figure 4.6: (a) $FAMAPbSnI_3$ transient absorption spectra of ΔA as a function of energy at room temperature for delay times ranging from 2 to 50 ps. (b) Carrier density dependence of $FAMAPbSnI_3$ room temperature transient absorption spectra for a delay time of 2 ps. (c) Room temperature CW carrier density dependence for $FAMAPbSnI_3$. (d) Cooling rate curves for carrier densities of 2 and 32 $\times$ 10^{14} cm^{-2} for $FAMAPbSnI_3$.

Recently, such hot acoustic phonon bottlenecks have also been used to explain slowed carrier thermalization in III-V nanowires [22,23] and InAs/AlAsSb quantum wells [24,25], where low thermal conductivity localizes acoustic phonons at the interfaces. This same mechanism could also be potentially invoked in the metal-halide perovskites at grain boundaries and regions of crystal phase mismatch, which are known to be prevalent in these systems [34].

Since the properties of the $FAMAPbSnI_3$ films are distinct from the other systems studied, their excitation-dependent TA are shown separately from the PbI-based systems in Figure 4.6 (a). In this case, the ground state bleach is centered at ~ 1.31 eV for the lowest excitation density of $n \sim 10^{14}$ cm^{-2}. As the excitation power increases, the ground bleach shifts to higher energy due to the increasing contribution of hot carriers and a growing low energy PIA. This PIA is linked to subgap impurity-related absorption in these nominally p-type perovskites[10] that increases at higher excitation densities ($\sim 10^{15}$ cm^{-2}).

The power dependent PL is presented in Figure 4.6 (c). The data can be correlated to the high-power TA (Figure 4.6 (a)), providing further insight into the emission and absorption profiles in $FAMAPbSnI_3$ under high intensity photoexcitation. At low power, the PL peak at 295 K is centered at approximately 1.2 eV, with a long low-energy tail. The origin of this PL peak at low power and temperature was discussed with respect to the transition P2 (Figure 3.1, Chapter 3), which has been attributed to the finite contribution of extrinsic low energy complexes due to local strain, regions of self-trapped excitons and/or isoelectronic centers, and was discussed previously with respect to Sn-oxidation [12,13,26]. As is evident in Figure 4.6 (c), as the power is increased, defect states are filled with and eventually saturated by photogenerated carriers, and the PL shifts to higher energy where it is then dominated by the intrinsic ground state exciton at approximately 1.33 eV. With further increasing power ($n > 10^{15}$ cm^{-2})) the PL shifts to higher energy and broadens, consistent with the shift of the quasi-Fermi

level into the valence band and the contribution of the p-type acceptors. This behavior is evident in several other intentionally doped n- and p-type semiconductors where high levels of unintentional impurities are evident [9,27,28]. In such cases, when evaluating PL for hot carriers, care must be taken, as this broadening reflects not only the presence of hot carriers but also the convolution of effects due to the background doping distribution and impurities. Typically, carrier temperatures for photoluminescence spectra are extracted from a linear fit of the photoluminescence using the equation (4.2):

$$I_{PL}(E) = \frac{A(E)E^2}{4\pi^2\hbar^3c^2}\left[\frac{1}{\exp\left(\frac{E-\Delta\mu}{k_BT_c}\right)-1}\right] \tag{4.2}$$

where, I_{PL} is the PL intensity, A(E) is the absorptivity as a function of energy, k_B is Boltzmann's constant, $\hbar$ is the reduced Planck's constant, c is the speed of light, T_c represents the carrier temperature, and μ is the chemical potential. T_c can be extracted from the slope of the natural logarithm of the PL spectrum. However, this requires that A(E) is constant over the portion of the spectral region to be fit, demonstrating the problem with PL spectra that change or evolve with increasing excitation, as discussed above.

Indeed, this has led to considerable discussion in the III-V community with respect to the determination of carrier temperatures in PL where full fitting of the PL spectra are often used to minimize such issues [11, 29-31]. Nonetheless, the hot carrier dynamics have been assessed from the high-energy tails of the

ground state bleach in the TA spectrum (Figure 4.6 (b)), since this represents a qualitative picture of high-energy "hot carrier" relaxation to the ground state in the Γ valley of the system.

In order to provide more detail on the subtle distinctions in the nature and origin of the carrier dynamic in the $FAMAPbSnI_3$ film, the time evolution of the TA at fixed exciton carrier density of $n = 3.2 \times 10^{15}$ cm^{-2} is shown in Figure 4.6 (b). These traces map the absorption and dynamics of the carrier distribution after

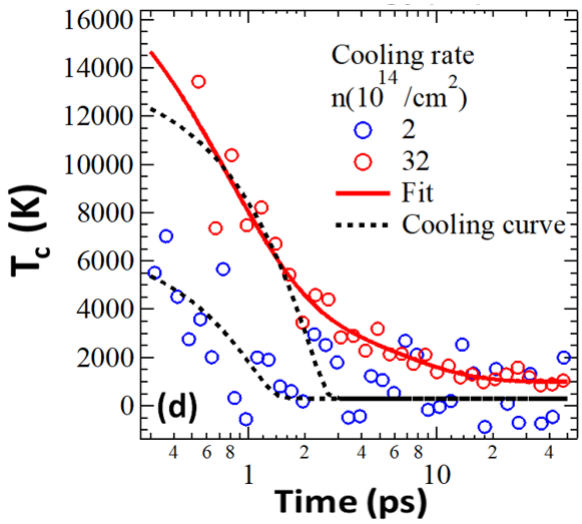


Figure 4.7: Carrier cooling rate curves for carrier densities of 2 and 32 $\times 10^{14}$ cm^{-2} for $FAMAPbSnI_3$.

a nonequilibrium hot carrier distribution has formed. At 2 ps (black open circles), the TA exhibits a strong PIA at low energy (1.0–1.25 eV) below the band gap of the system, which corresponds to the photo bleach minima at ≈1.3 eV at delay times > 50 ps. As time increases from 2 ps to 50 ps, the PIA decreases, along with an associated reduction in the position (redshift) and intensity of the photo bleach

(Figure 4.6 (b)). Again, the subgap absorption at t $<$ 50 ps is caused by free carrier absorption and unintentional p-type doping in this Sn based system, as evidenced by the subgap CW absorption and temperature dependent absorption shown in the inset to Figure 3.3(d) (Chapter 3) [10,15]. This type of absorption occurs when free carriers in the valence band transition to unoccupied Fermi-level states in the gap, in addition to conventional absorption across the band gap between the occupied and unoccupied valence and conduction bands. Upon photoexcitation at t $>$ 50 ps, photogenerated electrons occupy levels available in the gap created by Sn vacancies, which decreases the absorption edge to the Fermi-level position lowering the effective optical band gap.

Figure 4.7 shows carrier temperatures extracted from Figure 4.3 using equation 4.1 as a function of time at various extraction power densities ($n = 2 \times 10^{14}$ cm^{-2} to $n = 32 \times 10^{15}$ cm^{-2}). The carrier temperature is seen to increase with increasing excitation laser fluence due to the onset of a hot LO phonon bottleneck, whereby a large hot LO phonon density is inefficiently dispersed by the finite acoustic phonons in the system. [32] In the case of the metal halide perovskites, this effect is further exacerbated by the low thermal conductivity of these systems, which we suggest results in an acoustic phonon bottleneck at longer times. [32]

Our data indicates that the evidence suggests that an LA bottleneck, rather than an LO bottleneck, is dominant here, as shown by the systematic and rapid decrease in carrier temperature at $t < 2$ ps in Figure 4.7. This appears as a general

property of metal-halide perovskites seen across the literature [4,6,32]. Specifically, no clear trend is seen across these systems (nor in the literature) that relates carrier thermalization to the bandgap, exciton binding energy and/or phonon energy of any perovskite under study. This indicates that carrier relaxation in these materials does not follow the simple LO phonon decay process driven by Klemens or Ridley relaxation common to other polar semiconductors, but appears to be dominated or inhibited by thermal conductivity of the perovskites, in general.

4.3 Conclusion

Observations from continuous wave (CW) measurements from Chapter 3 are corroborated with the results obtained through transient absorption (TA) measurements. In the case of the Pb-based films, they display a photobleach due to the convolution of an excitonic feature and a high-energy photoinduced absorption (PIA) region, both situated within 20 meV of the bandgap. Contrarily, the behavior of the Sn-based film diverges significantly from the Pb-based films in both CW and TA, exhibiting an atypical low-energy PIA and an absence of high-energy PIA. The pronounced low-energy PIA in $FAMAPbSnI_3$ can be ascribed to the sub-bandgap absorption caused by impurity states and the unintentional p-type background inherent to these Sn-based systems, as also supported by CW transmission/absorption measurements (Chapter 3).

The absence of a distinct dependency of hot carrier relaxation on E_{ex}, E_{LO}, and/or Γ_{LO} implies a more generalized property for thermalization in the metal-halide perovskites. This slow cooling behavior is rather attributed to the low thermal conductivity of perovskites, which restricts the dissipation of the hot acoustic phonon bath via. low thermal conductivity. Consequently, a phonon bottleneck emerges, hindering the dissipation of hot LO phonons and, in turn, the hot carriers in the system. This phenomenon appears to account for the prolonged carrier relaxation observed across all perovskite systems.

4.4 References

1. G. Xing, N. Mathews, S. Sun, S. S. Lim, Y. M. Lam, M. Grätzel, S. Mhaisalkar, and T. C. Sum, Science 342, 344 (2013).

2. M. B. Price, J. Butkus, T. C. Jellicoe, A. Sadhanala, A. Briane, J. E. Halpert, K. Broch, J. M. Hodgkiss, R. H. Friend, and F. Deschler, Nat. Commun. 6, 8420 (2015).

3. J. M. Frost, L. D. Whalley, and A. Walsh, ACS Energy Lett. 2, 2647 (2017).

4. J. Fu, Q. Xu, G. Han, B. Wu, C. H. A. Huan, M. L. Leek, and T. C. Sum, Nat. Commun. 8, 1300 (2017).

5. M. Li, J. Fu, Q. Xu, and T. C. Sum, Adv. Mater. 31, 1802486 (2019).

6. J. S. Manser and P. V. Kamat, Nat. Photonics 8, 737 (2014).

7. J. Yang, X. Wen, H. Xia, R. Sheng, Q. Ma, J. Kim, P. Tapping, T. Harada, T.W. Kee, F. Huang, Y.-B. Cheng, M. Green, A. Ho Baillie, S. Huang, S. Shrestha, R. Patterson, and G. Conibeer, Nat. Commun. 8, 14120 (2017).

8. T. R. Hopper, A. Gorodetsky, J. M. Frost, C. Müller, R. Lovrincic, and A. A. Bakulin, ACS Energy Lett. 3, 2199 (2018).

9. C. R. Brown, N. J. Estes, V. R. Whiteside, B.Wang, K. Hossain, T. D. Golding, M. Leroux, M. Al Khalfioui, J. G. Tischler, C. T. Ellis, E. R. Glaser, and I. R. Sellers, RSC Adv. 7, 25353 (2017).

10. M. T. Klug, R. L. Milot, J. B. Patel, T. Green, H. C. Sansom, M. D. Farrar, A. J. Ramadan, S. Martani, Z. Wang, B. Wenger, J. M. Ball, L. Langshaw, A. Petrozza, M. B. Johnston, L. M. Herz, and H. J. Snaith, Energy Environ. Sci. 13, 1776 (2020).

11. H. Esmaielpour, V. R. Whiteside, L. C. Hirst, J. G. Tischler, C. T. Ellis, M. P. Lumb, D. V. Forbes, R. J. Walters, and I. R. Sellers, Progress in Photovoltaics: Research and Applications 25, 782 (2017).

12. N. K. Noel, S. D. Stranks, A. Abate, C. Wehrenfennig, S. Guarnera, A.-A. Haghighirad, A. Sadhanala, G. E. Eperon, S. K. Pathak,M. B. Johnston, A. Petrozza, L. M. Herz, and H. J. Snaith, Energy Environ. Sci. 7, 3061 (2014).

13. F. Hao, C. C. Stoumpos, D. H. Cao, R. P. H. Chang, and M. G. Kanatzidis, Nat. Photonics 8, 489 (2014).

14. Y. Yang, M. Yang, Z. Li, R. Crisp, K. Zhu, and M. C. Beard, J. Phys. Chem. Lett. 6, 4688 (2015).

15. T. Leijtens, R. Prasanna, A. Gold-Parker, M. F. Toney, and M. D. McGehee, ACS Energy Lett. 2, 2159 (2017).

16. P. G. Klemens, Phys. Rev. 148, 845 (1966).

17. B. K. Ridley, J. Phys.: Condens. Matter 8, L511 (1996).

18. A. Pisoni, J. Ja´cimovi´c, O. S. Bariši´c, M. Spina, R. Gaál, L. Forró, and E. Horváth, J. Phys. Chem. Lett. 5, 2488 (2014).

19. R. Heiderhoff, T. Haeger, N. Pourdavoud, T. Hu,M. Al-Khafaji, A. Mayer, Y. Chen, H.-C. Scheer, and T. Riedl, J. Phys. Chem. C 121, 28306 (2017).

20. T. Ye, X. Wang, X. Li, A. Q. Yan, S. Ramakrishna, and J. Xu, J. Mater. Chem. C 5, 1255 (2017).

21. N. Onoda-Yamamuro, T. Matsuo, and H. Suga, J. Phys. Chem. Solids 51, 1383 (1990).

22. C. K. Yong, J. Wong-Leung, H. J. Joyce, J. Lloyd-Hughes, Q. Gao, H. H. Tan, C. Jagadish, M. B. Johnston, and L. M. Herz, Nano Lett. 13, 4280 (2013).

23. I.-J. Chen, S. Limpert, W. Metaferia, C. Thelander, L. Samuelson, F. Capasso, A. M. Burke, and H. Linke, Nano Lett. 20, 4064 (2020).

24. H. Esmaielpour, V. R. Whiteside, J. Tang, S. Vijeyaragunathan, T. D. Mishima, S. Cairns, M. B. Santos, B. Wang, and I. R. Sellers, Progress in Photovoltaics: Research and Applications 24, 591 (2016).

25. H. Esmaielpour, V. R. Whiteside, C. Piyathilaka, S. Vijeyaragunathan, T. Mou, B. Wang, T. D. Mishima, N. J. Ekins-Daukes, M. B. Santos, A. D. Bristow, and I. R. Sellers, Sci. Rep. 8, 12473 (2018).

26. F. Hao, C. C. Stoumpos, R. P. H. Chang, and M. G. Kanatzidis, J. Am. Chem. Soc. 136, 8094 (2014).

27. S. Kurtz, J. F. Geisz, D. J. Friedman,W. K. Metzger, R. R. King, and N. H. Karam, J. Appl. Phys. 95, 2505 (2004).

28. E.M. Pavelescu, J. Wagner, H.-P. Komsa, T. T. Rantala, M. Dumitrescu, and M. Pessa, J. Appl. Phys. 98, 083524 (2005).

29. A. Le Bris, L. Lombez, S. Laribi, G. Boissier, P. Christol, and J. F. Guillemoles, Energy Environ. Sci. 5, 6225 (2012).

30. L. C. Hirst, H. Fujii, Y. Wang, M. Sugiyama, and N. J. Ekins Daukes, IEEE Journal of Photovoltaics 4, 244 (2014).

31. F. Gibelli, L. Lombez, and J.-F. Guillemoles, J. Phys.: Condens. Matter 29, 06LT02 (2017).

32. S. Sourabh, V. R. Whiteside, I. R. Sellers, Y. Zhai, K. Wang, M. C. Beard, V. Yeddu, M. T. Bamidele, and D. Y. Kim, Phys. Rev. Mater. 5, 095402

(2021).

33. S. Kahmann and M.A. Loi, "Hot carrier solar cells and the potential of perovskites for breaking the Shockley–Queisser limit", Journal of Materials Chemistry C, vol. 7, no. 9, pp. 2471-2486, 2019.

34. P. Fassl, et al., "Effect of Crystal Grain Orientation on the Rate of Ionic Transport in Perovskite Polycrystalline Thin Films", ACS Applied Materials & Interfaces, vol. 11, no. 2, pp. 2490-2499, 2019.

Chapter 5

Evidence of Hot Carriers in Metal Halide Perovskite Solar Cells

5.1 Introduction

The research community is facing significant challenges due to the rising global demand for energy and the need for sustainable implementation of green technologies. The challenge for the photovoltaics community is to develop new materials and increase the power conversion efficiency of photovoltaic systems while reducing operational costs. Metal halide perovskite solar cells have gained significant interest due to their facile fabrication and the potential for large-scale roll-to-roll manufacturing protocols. In less than a decade, these materials have achieved solar cell power conversion efficiencies over $> 25\%$, surpassing those of thin film or multi-crystalline silicon [1]. Moreover, perovskite-based tandems have recently also outperformed single junction GaAs solar cells [2].

Despite facing challenges such as poor stability, low yield, and reproducibility concerns, significant progress has been made in stabilizing the ABX_3 structure of perovskites, increasing the lifetime of these systems. Indeed, perovskite solar cells have been demonstrated operation for over 1000 working hours in ambient conditions for both Pb [3] and Pb-Sn [4] based systems.

To improve the stability of perovskite absorbers, a significant innovation has been the fine tuning of their chemical compositions. This includes alloying on both the A-cation and the X-halide anion sites, such as in the so-called FAMACs systems [5] or triple halide perovskites, which are under development for tandem structures [6]. Such alloying optimizes the structural tolerance factor and has been shown to effectively improve the stability of materials.[7]

While perovskite systems have become more compositionally complex than early systems such as $MAPbI_3$ or $FAPbI_3$. [51], these combinations of double or triple cations and/or halides have been shown to produce more thermodynamically and crystallographically pure, which inhibits parasitic or irreversible halide segregation and disorder [7-10]. These advances have allowed perovskite films and devices to withstand extreme thermal cycling [11] and high temperatures, as well as inhibit UV degradation [6]. Recent studies have also suggested the presence of long-lived hot carriers in perovskites [12-17], indicating their potential in advanced concept photovoltaics, such as hot carrier solar cells. [52-54]

Moreover, the photovoltaic response of $FA_{0.8}Cs_{0.2}PbI_{2.4}Br_{0.6}Cl_{0.02}$ solar cells have now also been shown to exhibit hot carriers under practical operational conditions, further supporting the potential of these systems for hot carrier devices [55].

5.2 Result and Discussions

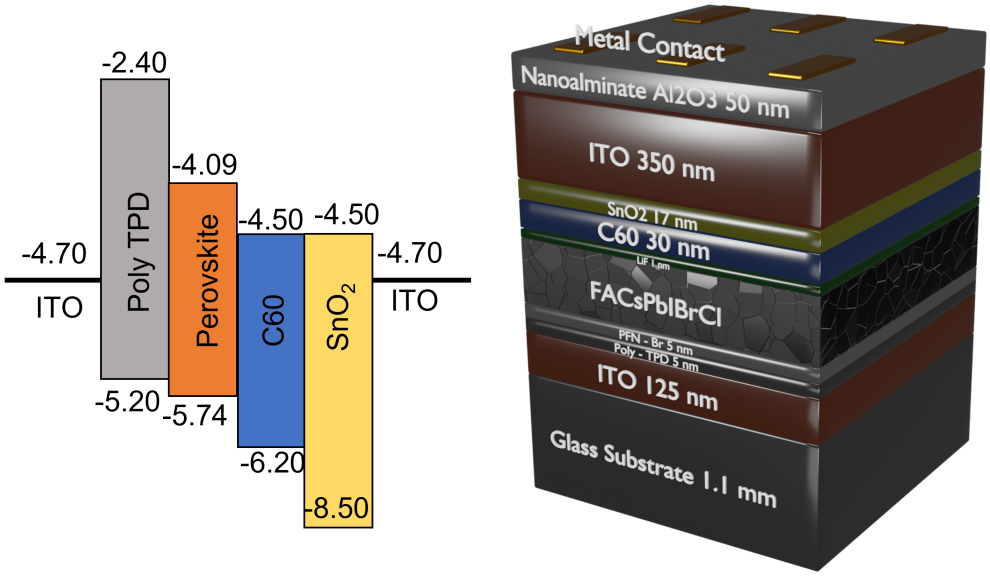


Figure 5.1: Schematic of the band offsets (left) and device structure (right) for the double cation/triple halide perovskite solar cell investigated in this work [55].

Figure 5.1 shows (a) the energy band alignment and (b) a schematic of the device studied here. The devices provided by Swift Solar consist of a 200 nm spin-coated $FA_{0.8}Cs_{0.2}PbI_{2.4}Br_{0.6}Cl_{0.02}$ absorber layer integrated into a device structure consisting of an ITO front contact, a PolyTPD (poly(N,N-bis-4-butylphenyl-N,N-bisphenyl)- benzidine) hole transport layer with a PFN-Br (poly[(9,9-bis(3-(N,N-dimethylamino)propyl)- 2,7-fluorene)-alt-2,7-(9,9- dioctylfluorene)]dibromide) in-terface layer. The back of the device includes, ZTO/SnO2 and C60 electron transport layers with a LiF interfacial layer for passivation, followed by an ITO back-contact. The devices were completed with a 50 nm

TiO_2/Al_2O_3-based multilayer encapsulant to improve the atmospheric stability.

The current density–voltage (J-V) responses of the devices were initially evaluated

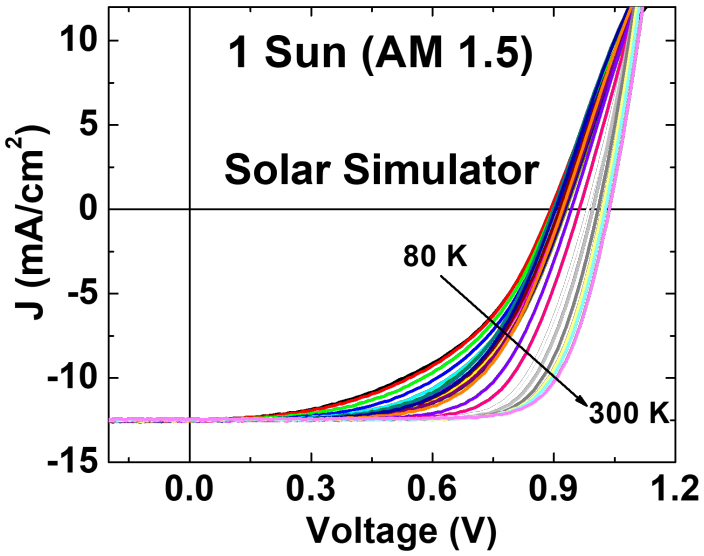


Figure 5.2: Temperature-dependent J-V plots under 1 sun AM 1.5G illumination between 80 K and 300 K. At lower temperatures, a loss of FF is evident due to limited carrier extraction.

under 1-sun AM 1.5G illumination (Figure 5.2). The devices were tested from 80 K to 300 K, and an increase in the fill factor was observed as the temperature was increased, which can be attributed to the decreasing effect of the parasitic barrier at higher temperatures. The parasitic barrier emerges as a result of a mismatch of the material properties at the heterojunction interfaces, resulting in poor charge extraction [29]. At high temperatures, thermionic emission improves and circumvents the poor extraction due to the parasitic barrier and improves the charge extraction, resulting in the improvement of FF at higher temperatures.

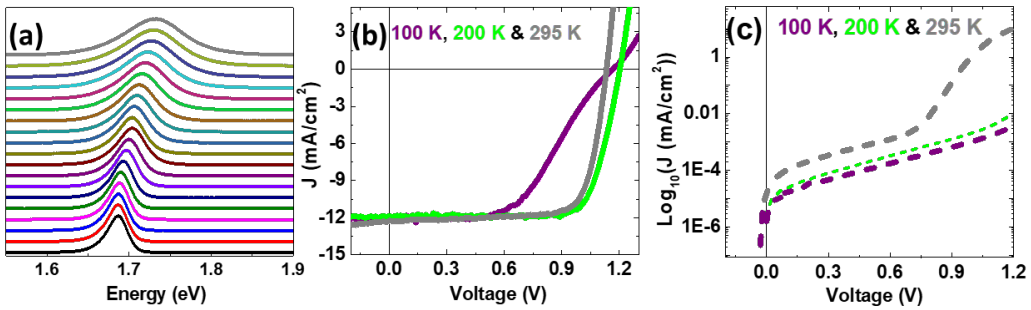


Figure 5.3: (a) Normalized waterfall plot of temperature dependent photoluminescence from 4 K to 295 K. (b) Comparison of the low power (1-sun AM 1.5G equivalent) monochromatic (532 nm excitation) current density – voltage responses at 100 K (purple), 200 K (green), and 295 K (gray) along with their respective (c) dark JVs (same color code).

Here, the presence of hot carriers and the role of halide segregation and materials decomposition are assessed using simultaneous current-density voltage (J-V) and photoluminescence (PL) measurements. The simultaneous measurements were conducted from 4 K to 295 K using a Janis closed cycle cryostat system in a systematic manner. A 532 nm laser with power densities ranging from 20 mW/cm^2 to 8000 mW/cm^2 (equivalent to 0.2 to 80 suns under AM 1.5G) was used as the excitation source.

The normalized temperature-dependent photoluminescence (PL) spectra for a representative $FA_{0.8}Cs_{0.2}PbI_{2.4}Br_{0.6}Cl_{0.02}$ solar cell is shown in Figure 5.3 (a) measured between 4.2 K (bottom line - color) and 295 K (top line – color). As the temperature is increased, there was a noticeable blueshift in the peak emission

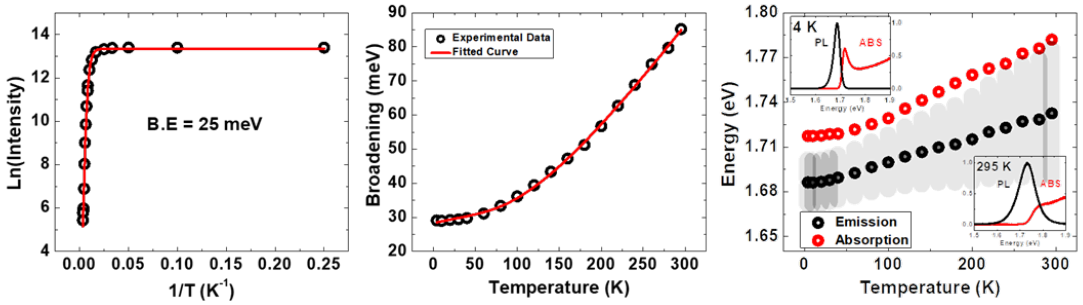


Figure 5.4: (a) Arrhenius analysis and the (b) FWHM extracted from the temperature-dependent photoluminescence, and (c) a comparison of the temperature-dependent PL peak energy and the absorption edge observed in transmission spectroscopy used to determine the Stokes shift in these systems. The insets to (c) show the temperature-dependent emission and absorption at 4 K (upper inset) and 295 K (lower inset).

energy, which (as discussed in Chapter 3, section 3.2) shows the well-known blueshift observed in the perovskites that is related to the unique bandstructure of these materials [19].

In addition to this blueshift, as the temperature increases, there is also significant broadening of the PL spectra. This is a consequence of the polar nature of these materials that mediates strong electron-LO phonon coupling [18, 20-22] in these systems, as established widely in the community. [23-25]. These data will be discussed further below with respect to Figure 5.4. In addition to assessing the PL properties with respect to temperature, simultaneous J-V measurements were also performed under laser excitation at the same conditions to those used for the TD PL. An assortment of these TD J-V measurements are shown in Figure 5.3

(b) for $T = 100$ K, 200 K, and 295 K. The associated dark J-V are also presented on a log scale in Figure 5.3 (c).

At low temperatures, $T < 200$ K a strong inflection is observed in the light J-V curves, which is also reflected in very low dark currents at the same temperatures (Figure 5.3 c). This reduced performance at lower temperatures is attributed to a mismatch in the band gaps of the various layers in the structure at low temperatures, which creates parasitic barriers to minority carrier extraction in these devices, as well as reduced transport or conductivity in the electron and hole transport layers in the device (see Figure 5.1) [27].

The phonon mediated broadening of the PL linewidth for the samples studied here are shown in Figure 5.4(b), which shows the FHWM extracted from the TD PL. This FWHM is observed to increase from $\sim$ 30 meV at 4.2 K to $\sim$ 80 meV at room temperature [14, 23, 26]. Figure 5.4 (a) shows Arrhenius analysis of the temperature-dependent photoluminescence between 4.2 K to 300 K (black open circles) fit to equation (red line) [58]:

$$I(T) = \frac{I_o}{1 + A \cdot \exp\left(-\frac{E_x}{k \cdot T}\right)} \tag{5.1}$$

Here, *I(T)* is the PL intensity as a function of temperature (T), I_o is the peak

intensity at 0 K, A is the pre-exponential factor, E_x is the binding energy of exciton (in eV), k is the Boltzmann constant (8.617 x 10^{-5} eV/K), T is the absolute temperature in Kelvin (K). From this analysis, a binding energy of $\sim$ 25 meV was extracted, which is consistent of the value determined by others for these systems in the literature [56] and reflects the quenching of the PL at higher temperature close to 300 K. Figure 5.4 (c) shows a comparison of peak PL energy (black open circles) and the absorption edge (red open circles) extracted from TDPL and TD transmission measurements, respectively. The inset in Figure 5.4 (c) shows the relative PL (black) and absorption (red) at 4K (upper left) and 295 K (lower right). The shaded regions in (c) shows the extent of the inhomogeneous overlap between PL and absorption, which is increases at higher temperatures. This increasing inhomogeneity is once again a manifestation of the extent of broadening in the system due to phonons and the strong polar nature of these systems.

The Figure 5.5 shows the complete set of J-V spectra from 4.2 K to 295 K. The J-V at 100 K (solid purple line) is dominated by a strong s-shaped inflection, as discussed above, indicating the presence of a parasitic barrier to minority charge carrier extraction [27].

While this s-shape behavior has been observed previously in perovskite solar cells [27] the effects of the parasitic barriers to carrier extraction in PL is less well studied. Here, it is shown that when carriers are "blocked" or "trapped" at

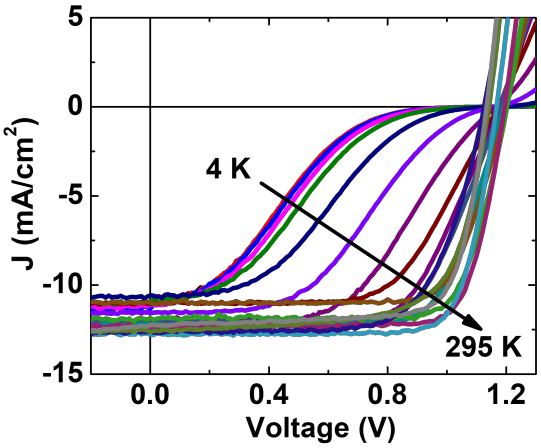


Figure 5.5: Monochromatic J-V plot from 4 K to 295 K, under 532 nm laser excitation at 1-sun AM 1.5G equivalence. The lower temperature shows s-shape behavior due to parasitic barriers existing at the heterojunction interfaces as also illustrated in Figure 5.3 (b).

interfaces – such as at low temperature - strong emission is observed from the solar cells (PL intensity), which reduces the photovoltaic performance the devices but does not increase non-radiative losses significantly [5,11,28,29].

When the temperature is increased to 200 K (solid green line – Figure 5.3 (b)) and further to 295 K (solid gray line – Figure 5.3 (b)) there is an improvement in the fill factor and a decrease in the series resistance. The dark J-V also improves at $T > 200$ K (Figure 5.3 (c)). These changes suggest that minority carrier collection and transport improve at higher temperatures and that the efficiency of perovskite solar cells is well matched to the operational conditions of terrestrial PV.

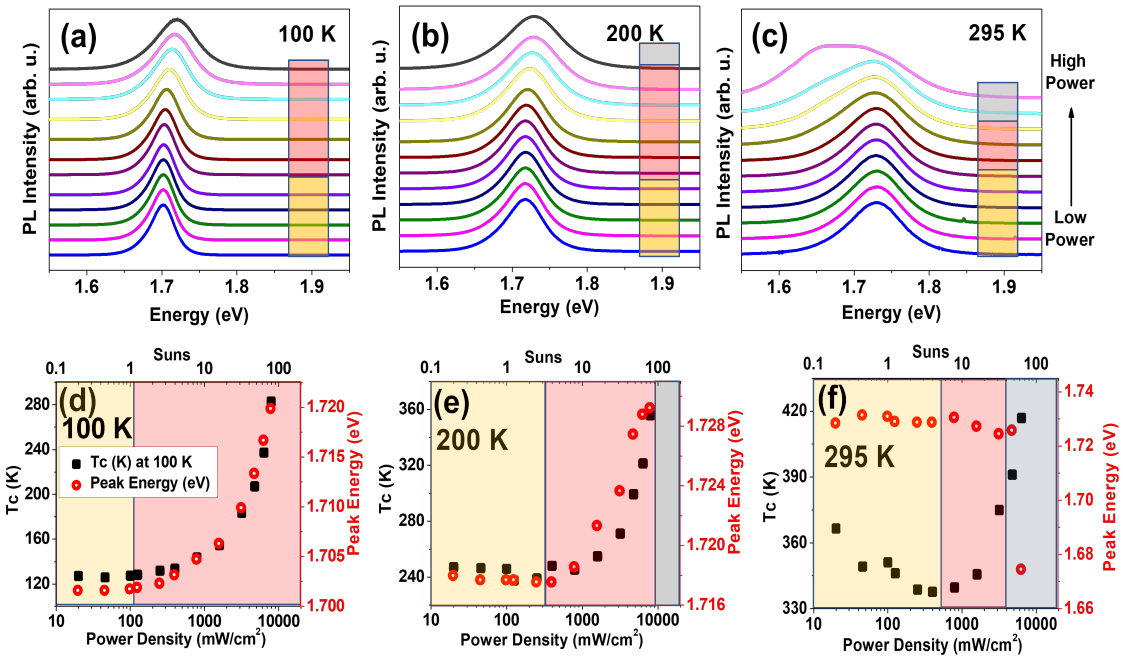


Figure 5.6: The PD PL spectra at 100 K, 200 K and 295 K, labeled as (a), (b), and (c), respectively and a comparison between T_c (solid black squares) and the peak energy (open red circles) are presented in (d), (e), and (f) at same three temperatures, respectively. The shaded regions represent the region of equilibrium (yellow), non-equilibrium (red), and the regime in which decomposition begins to occur (gray).

In order to better understand the role of lattice temperature on the operating conditions of the solar cell, and the role and presence of hot carriers in the system, simultaneous power dependent (PD) PL and J-V were performed at 100 K, 200 K, and 295 K. Figure(s) 5.6 (a), (b), and (c) show the normalized PD PL at 100 K, 200 K, and 295 K, respectively.

At 100 K (Figure 5.6 (a)) as the power increases from 20 mW/cm^2 to 8000 mW/cm^2 (0.2-sun to 80 suns equivalent at AM 1.5G) the PL blue shifts and broadens, indicating an increase in heat in the system. A slight shift is also still visible at 200 K (Figure 5.6 (b)), despite the screening of this shift due to increased contribution of LO-phonon mediated broadening. The shift of the peak PL energy is more apparent when plotted as a function of power as shown in Figure(s) 5.6 (d) and (e) (open red circles) for 100 K and 200 K, respectively.

Figure 5.6(c) shows the normalized PL at 295 K, which is found to be or the order three orders of magnitude lower as compared to 100 K (and two orders lower at 200 K, not shown for brevity [55]. This is due to a combination of the ionization of excitons at room temperature and the efficient transport and extraction of carriers at higher temperatures as the band offsets and thermal energy become optimum for PV operation [30]. At 295 K, there is also a notice change in the PL spectra particularly at higher laser fluence. This is attributed to halide segregation and possibly the onset of a phase transition at higher photoexcitation levels, Figures 5.6 (d), (e), and (f) present a comparison of the peak energy extracted from the PD PL at 100 K, 200 K, and 295 K, with the T_c obtained from the continuous wave (CW) PL slope using the generalized Planck equation:

$$\ln(I_{\mathrm{PL}}(E)) = \ln(\varepsilon(E)) - \frac{E}{k_B T_c} \tag{5.2}$$

(ϵ) is the effective emissivity, which is related to the absorptivity of the system, E is the energy and T_c is the carrier temperature [57]

This method of evaluating hot carriers in steady-state measurements, developed by the III-V photovoltaic community [32-35], has been recently applied in different forms to study perovskites in transient absorption [14, 36] and steady-state CW PL measurements [15, 16, 36].

Here, we use a simple linear fit of the high-energy slope to extract the T_c, while also accounting for the contribution of phonon broadening [36, 37] to reveal the qualitative trend in carrier heating [38]. This is then supported by analysis of the simultaneous PD J-V (Figures 5.8) to confirm the presence of hot carriers in the devices. It is important to mention that such analysis can only be performed on PL if it is not affected by excessive inhomogeneity and PL shape is not changing dramatically with power - as is the case with the PL at 295 K [24, 39, 40]. This precaution prevents erroneous results that would invalidate the use of the generalized Planck's equation, as previously described [39], which is discussed further with respect to the 295 K measurements below.

Figure 5.6 (d) presents a comparison of the T_c and the peak energy at 100 K, extracted from the data in Figure 5.6 (a). At this temperature the phonon broadening is minimized, and the PV operation of the devices is strongly perturbed by parasitic barriers to carrier extraction (see Figure 5.5)

At excitation powers below 100 mW/cm^2 the T_c extracted from the PL remains constant, and the system is considered to be in equilibrium (yellow-shaded region), with both photogenerated carriers and lattice having a temperature of $\sim$ 100 K [37, 41].

However, when the excitation power increases from 100 mW/cm^2 to 8000 mW/cm^2, T_c increases (solid black squares) from 100 K to 280 K. This temperature increase can be attributed to either lattice heating or the presence of hot carriers in the device. As we discuss below in the J-V measurements, we attribute this temperature rise predominantly to the presence of hot carriers, which dominate at lower temperatures. Additionally, while the extracted T_c increases with increasing laser fluence, there is also a simultaneous increase in the peak PL energy (open red circles) (Figure 5.6 (d)). The temperature of 200 K (Figure 5.6 (b,e)) serves as a transitional point between 100 K and 295 K. At this temperature, low powers exhibit behavior similar to that observed at 100 K, with T_c increasing from an equilibrium temperature of approximately 200 K at powers below 400 mW/cm^2 (yellow shaded region) to 360 K (pink shaded region) at approximately 6300 mW/cm^2. However, higher fluences lead to the threshold for halide segregation (as shown in the gray in Figure 5.6 (b)). The regime is more prevalent at 295 K, due to the higher thermal energy of the lattice. In this regime described by the gray shading, perovskite decomposition and halide segregation cause the PL to broaden and results in a reduction of the peak PL energy (Figure 5.6 (f)) [10,

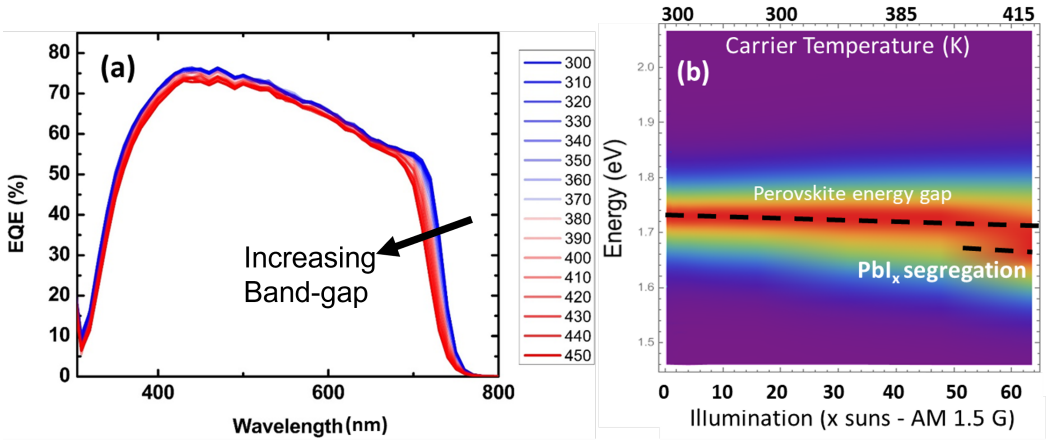


Figure 5.7: (a) The EQE of the device, with increasing bandgap as a function of temperature. The trend do not show any indication of phase transition; (b) Power-dependent PL heat map, indicating a non-abrupt shift and the existence of two peaks (dotted line) after 50 suns, indicating possible phase segregation rather than phase transition.

42] along with the appearance of a second longer energy peak, which eventually dominates at higher powers as halide segregation results in the generation PbI_3 rich regions [8, 42].

While a structural phase transition cannot be discounted, the temperature-dependent bandgap in EQE and Heat map indicates the possibility of phase segregation rather than a phase transition. The EQE (Figure 5.7 (a)) is also a measurement of the band gap of the material. While the PL in Figure 5.6 (c) shows the change in the PL trend, the EQE shows the monotonous increase in the bandgap as a function of temperature (Figure 5.7(a)). Usually, a phase transition shows a decrease in the perovskite bandgap at the critical temperature as it is associated with the structural change in the material, while it is not the case

with phase segregation. Hence the monotonic increase in the bandgap from EQE suggests phase segregation. Another evidence is the heat map of the PL (Figure 5.7 (b)), where two peaks after 400 K (or 50 suns power) temperature are clearly visible. In the case of phase transition, an abrupt change in the peak position is common while in the case of phase segregation, the continuous formation of separate MX domains in the metal halide perovskites (with AMX_3 structure) a rather shows a smooth transition, as shown in Figure 5.7 (b), thus supporting the phase segregation in this case. The effect of segregation can be seen in Figure 5.6 (f), which shows a comparison of T_c and the peak PL energy at a lattice temperature of 295 K. While again, at 295 K, the phonon-mediated broadening of the PL masks any shift in the peak PL energy with increasing fluence, and at the highest powers, the dominated PL peak transitions from an equilibrium regime (yellow region) directly to one dominated by halide segregation (gray region), screening any potential effects due to hot carriers (red region). This is further supported by the PL line shape for this temperature range and power regime shown in Figure 5.6(c), and the reduction of the peak PL energy evident in Figure 5.6(f).

Again, the considerable changes seen in the PL linewidth at higher powers make it challenging to determine a realistic T_c at 295 K due to the several factors that broaden the PL. Although the previous discussion suggests that the system undergoes heating at high fluence, the origin of this heat and the impact of increased lattice heating versus the effects of photo-excited non-equilibrium "hot

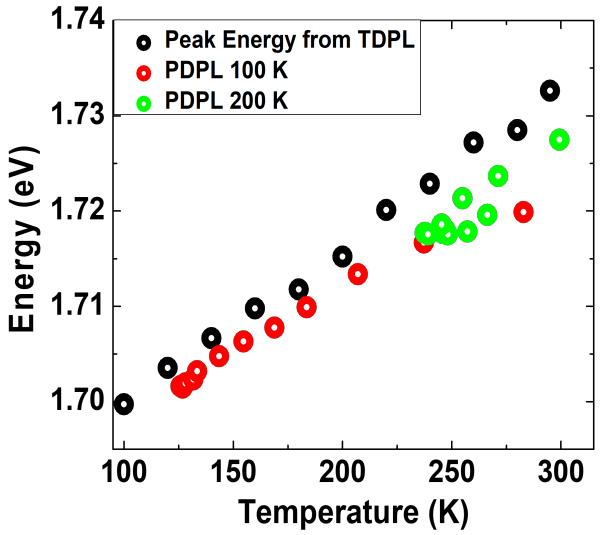


Figure 5.8: Comparison of the temperature dependence of the peak PL energy with the shift in PL energy as a function of laser irradiance at the 100 K (open red circles) and 200 K (open green circles).

carriers" require further investigation.

In Figure 5.6 (d), (e), and (f), the extracted T_c rises along with a blue shift in the peak PL energy, indicating that the system is heating, but it does not reveal any information on the nature of the increased thermal energy in the system. This can be seen in Figure 5.8 which compares the temperature dependence of the PL with the shift in the PL peak energy from power dependence measurements at the equilibrium lattice temperature of 100 K and 200 K. It is apparent that the high power excitation from the laser increases the temperature of sample by $\sim$ 125 K (from 100 K to $\sim$ 225 K) and 75 K (from 200 K to $\sim$ 275 K), at 100 K and 200 K respectively.

A simple explanation for the increased temperature seen with increasing power, which matches the effects of lattice heating somewhat (Figure 5.8) is that the low thermal conductivity in perovskites limits heat dissipation [18]. However, the J-V responses measured simultaneously with the PL indicate that the effects are less obvious than those derived from simple arguments of inhibited heat dissipation in these measurements.

Figure 5.3 (b) shows that increasing the device's temperature under 1-sun AM 1.5G equivalent excitation improves the FF and PV response of the solar cell by increasing carrier extraction in the heterostructure architecture. [27] However, when examining the J-V response of the device as a function of laser fluence at 100 K, 200 K, and 295 K, as shown in Figures 3(a), (c), and (e), respectively, the J-V response exhibits slightly different behavior compared to that with increasing (equilibrium) lattice temperature (Figure 5.3 (b)), which is considered further below.

Figure 5.9 (a) presents the power-dependent J-V response at 100 K, and Figure 5.9 (b) shows the same data normalized with respect to J_{sc} (V = 0) to evaluate the impact of increasing power on the shape of the J-V response, following the analysis of Dimmock *et al.* [47]. The J-V responses are plotted with respect to the three regimes described in Figure 5.6 for the associated PL. Specifically, the solid lines in the J-V data represent the equilibrium temperature region, while the

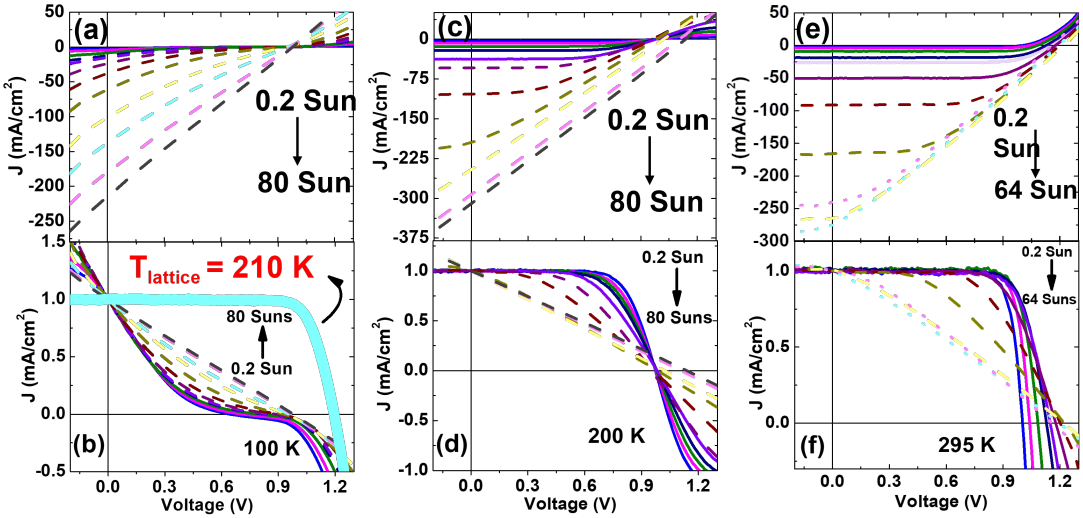


Figure 5.9: Power-dependent J-V curves at various temperatures (a) 100 K, (c) 200 K, and (e) 295 K under incident light intensities from 0.2 to 67-80 Suns. Corresponding Normalized J-V curves with respect to J_{sc} - in (b), (d), and (f), emphasizing J-V behavior changes with fluence. Ohmic like J-V characteristics across all 3 temperatures imply that the behavior is not merely due to lattice heating, as the differences between the heated system at $\sim$ 210 K (dotted line) and lattice-heated sample $\sim$ 210 K (cyan solid) indicated in (b).

dashed and dotted lines represent the non-equilibrium and decomposition onset regimes, respectively.

Once again, Figure 5.9 (a) displays the non-ideality of the system at lower temperatures [3, 29]. This is amplified in the normalized J-V data at 100 K shown in Figure 5.9 (b). It is also apparent that as the laser fluence increases, the diode rectification is removed, the FF decreases, and the device becomes more resistive

with a substantial increase in J_{sc} (Figure 5.9 (a)). The magnitude of J_{sc} scales with the laser fluence as is especially obvious in Figure 5.9 (a) where phononic effects are low and inhibited carrier extraction are at a maximum. Moreover, here, with increased laser fluence the saturation of the photocurrent that would reflect the absorbed photon flux and infinite shunt resistance of conventional PV operation (Figure 5.9 (b)) is absent. The transition to a linear resistive-like J-V response observed at higher powers in Figures 5(a) and (b) – coupled with the presence of carrier heating in the PL - indicates the presence of a non-equilibrium hot carrier population [47].

Additional evidence that the J-V is dominated by non-equilibrium carrier extraction (hot photocurrent - rather than simple lattice heating) is provided by the significant difference in the equilibrium J-V response at 210 K as compared to the equivalent 100 K PD J-V ($\sim$ 4700 mW/cm^2 = 47 Suns), which is the PD J-V with a carrier temperature determined from equation 5.2 that matches the temperature in which the FF is recovered in Figure 5.5. The comparison is made directly in Figure 5.9 (b). The equilibrium J-V at 210 K (solid cyan line) exhibits a typical photovoltaic response with a J_{sc} of approximately 12 mA/cm^2. In contrast, the high-power PD J-V with an effective temperature of 207 K (dashed cyan) shows a photoconductive-like response and a large J_{sc} of approximately 320 mA/cm^2.

The device behavior at higher power and low temperature (100 K) is indicative

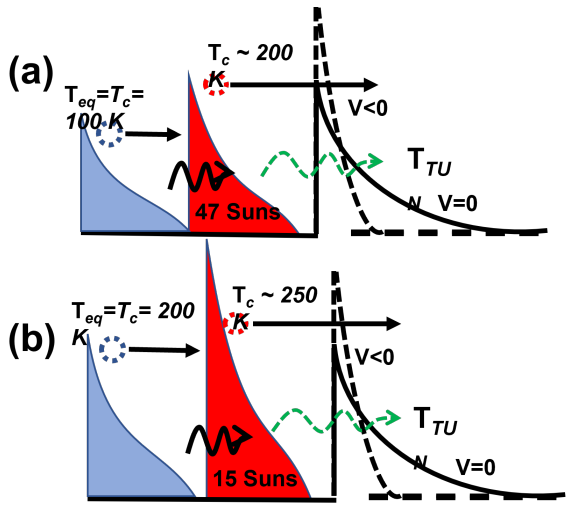


Figure 5.10: Schematic of (a) Equilibrium (Teq, blue) and hot carrier (T_c, red) distributions excited at a power of 4700 mW/cm^2 ($\approx$ 47x suns) at 100 K with $T_c \approx 200$ K. The parasitic barrier is depicted at V = 0 (solid) and V < 0 (dashed). Thermionic emission is illustrated by a solid black arrow, and tunneling is represented by a dotted green arrow. (b) The same mechanisms are shown for $T_{eq} = 200$ K.

of the generation and subsequent extraction of a hot carrier distribution, the tail of which exceeds the parasitic barrier and/or heterointerface [47]. In such a system, as the bias is increased in the negative direction, the extraction of the hot carriers via thermionic emission begins to compete with direct tunneling as the potential barrier narrows. In this regime, the slope of the J-V represents the resistance to minority carrier extraction from the carrier distribution, in general, and the limited role of the heterostructure in producing diode-like rectification, which is eliminated at high laser fluence, resulting in ballistic-like behavior.

A schematic illustration of the proposed role of such a parasitic barrier and the transport and collection of equilibrium and non-equilibrium carrier population in such a system with various powers and as a function of temperature is illustrated in Figure 5.10. The electron Fermi distribution at 100 K (blue) and 200 K (red) are shown to the left of a potential barrier shown in black with an applied bias of V = 0 V (solid line) and in reverse bias (dotted line) for the suggested protocol provided in Figure 5.10. At 100 K, the carrier distribution encounters a large potential barrier until substantial reverse bias is applied when breakdown would occur. However, in the case of the hot carrier distribution (red $\sim$ 47 suns), there exists a significant tail above the barrier that enhances thermionic emission (TE) resulting in greater carrier extraction. As the reverse bias narrows the barrier, TTE competes with direct tunneling (TUN).

Increasing the lattice temperature from 100 K to 200 K facilitates carrier transport through the device by increasing thermal energy, as well as reducing the contribution of parasitic resistances and non-ideal heterointerfaces within the solar cell architecture [55]. Despite the improved PV functionality of the solar cells at 200 K, evidence of parasitic heterointerfaces are evident in a high series resistance at low powers ($P < 250$ mW/cm^2) - Figure 5.9 (c). Evidence of a photoconductive response and the presence of hot carriers is also observed in Figure 5.9 (d) at $P > 1000$ mW/cm^2 (dashed lines) and the corresponding PL (Figure 5.6 (b)).

In Figure 5.10 (b), it is shown that the higher thermal energy at 200 K reduces

the effect of the barrier to carrier transport compared to 100 K. The rectifying properties of the solar cell are limited by the direct transport of hot carriers across the heterojunction, which restricts the effect of the electric field in modulating carriers at the interface and therefore remove the diode like behavior in the devices. Although the extract hot carrier type (electron and/or hole) creating this effect or indeed which interface is responsible requires further study, these measurements confirm that non-equilibrium carriers persist in perovskites at high fluences, even at levels achievable in practical concentrator PV systems [6].

In the protocol proposed, at higher laser powers, hot carriers are extracted by thermionic emission, but these carriers cool down in the non-optimized contacts. This means the voltages evident here (Figure 5.11 (d), (e) and (f)) are lower than expected for ideal hot carrier solar cell (HCSC) operation [48,49] and continue to be defined by the perovskite absorber bandgap, despite the appearance of hot photocurrents observed in the devices assessed.

At 295 K, perovskite solar cells operate with high efficiency under 1-sun conditions [3]. The majority and minority carrier transport under such operation in these heterostructure based devices is dominated by diffusion across the perovskite absorber, and the extraction and rectification of carriers at high field regions at the heterointerfaces between the perovskite and the electron and hole transporting layers [50]. Under these optimum conditions the PL intensity is low. This is mainly due to the efficient extraction of carriers from the devices under these conditions.

At higher powers – as has been discussed above – the PL begins to demonstrate evidence of halide segregation, with the presence of a structural phase transition not fully discounted when high temperatures are produced under large fluences at 295 K. This, therefore, makes the discussion of hot carrier effects in PL difficult at ambient temperatures. However, if the PD J-V data are considered in Figure 5.10 (f) there is evidence of loss of rectification at high powers even at 295 K when the laser power is increased above 600 mW/cm^2, which is equivalent to about 6X-suns. [47].

Once again it is important to note, that although the devices presented show evidence of hot carrier effects via the extraction of hot photocurrent, they do not result in increased efficiency or nor can this be considered evidence for the realization a hot carrier solar cell (HCSC) [48]. The structures are not designed to extract hot carriers selectively, and the absorber band gap sets the operation of these solar cells, particularly V_{oc}. Figure 5.11, provides more evidence to support the presence of hot carriers and their impact on solar cell operation. Here, the PV parameters including V_{oc} and J_{sc} extracted from the PD J-V responses at 100 K (Figure 5.11 (d), 200 K (Figure 5.11 (e)) and 300 K (Figure 5.11 (f)) are directly to those of the integrated PL and energy (Figure 5.11 ((a),(b),(c))).

Figures 5.11 (a) and 5.11 (d) compare the power dependence of the PL and PV parameters at 100 K, respectively. As expected, the PL intensity increases with increasing laser fluence. However, at $P > 1600$ mW/cm^2 ($\sim$ 16X suns) in Figure 5.11, there is a significant drop in PL intensity, while the peak PL energy continues

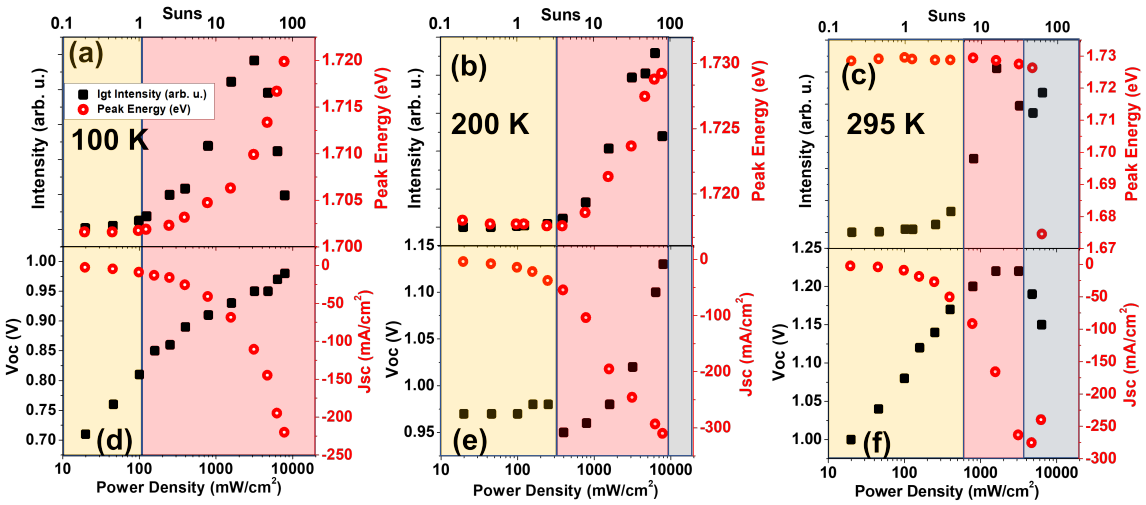


Figure 5.11: Comparison of peak energy and intensity from power-dependent PL (a-c) with V_{oc} and J_{sc} from power-dependent JV characteristics measurements (d-f) as a function of laser fluence. Regions corresponding to equilibrium (yellow), hot carrier (red), and phase segregation (grey) are highlighted, showcasing the variations in J_{sc}, V_{oc}, intensity, and peak energy in each region

to blue shift. This drop in PL intensity is attributed to the thermionic emission of non-equilibrium hot carriers and the increased extraction of this photogenerated carrier distribution generated at higher fluences. This hypothesis is supported by a simultaneous increase in J_{sc} at the same high powers and the exponential dependence of the photocurrent at $P > 1600$ mW/cm^2 [5, 29] as the tail of the hot carrier distribution exceeds the parasitic barriers in the structures (see Figure 5.10 (a)).

The effect of increasing light intensity on the V_{oc} (solid black squares) at 100

K is shown in Figure 5.11(d). In the low power regime ($P < 1600$ mW/cm^2), V_{oc} rises from approximately 0.7 V to 0.9 V, which represents a standard response of a solar cell to increased light excitation. The band offset is not optimized at low temperatures, leading to the formation of a parasitic barrier. However, as the fluence increases (from very low power), the excited charge carrier density begins to passivate extrinsic features, such as trap states that stem from the parasitic barrier effects at the device interfaces. This results in an enhancement of the effective V_{oc}. At the highest power ($P \approx 8000$ mW/cm^2, or ∼80X suns), when all parasitic states are passivated, V_{oc} reaches ~ 1 V, consistent with the absorber bandgap.

The same correlation between non-equilibrium carrier generation and thermionic extraction, and increasing V_{oc} along with the simultaneous quenching of PL at higher powers is also seen at 200 K. These data are shown in Figure(s) 5(b) and (e). At the highest power, the thermal energy of the photogenerated carriers (k_BT) reduces the effective energy of the potential barriers seen by these charges in the devices, and results in improved carrier extraction at 200 K. This results in increasing J_{sc} and reduced PL intensity at 200 K, with respect to (for example) $T < 200$ K. At 295 K, we can differentiate the effects due to non-equilibrium hot carriers (observed at lower temperatures) and effects due to decomposition of the perovskite, specifically halide segregation and potential structural changes.

In Figure 5.11(c), it is observed that laser fluence has less significant or apparent impact on the peak PL energy, although a slight decrease in energy is evident at

$P > 800$ mW/cm^2. This decrease is linked to an increase in the *integrated* PL intensity (solid black squares). When these effects are compared with the PL spectra at 295 K shown in Figure 5.6(c), it is evident that the emission comes from a broadening of the PL, and the increasing inhomogeneity of these perovskites at this temperature at higher powers [1, 2]. These effects begin to dominate the PL spectrum and reduce the "effective" band gap for emission as the contribution of halide inclusions and decomposition increases, which is evident at high fluence in Figure 5.11(c) (open red circles).

This change from equilibrium behavior (yellow shaded) to a regime where material decomposition dominates (gray shaded) is also visible in the PV parameters at 295 K at higher fluence in Figure 5.11(f). At lower fluences, both V_{oc} and J_{sc} increase simultaneously with an increased photon flux, as expected in a PV device. However, as the power exceeds ~ 3100 mW/cm^2, the inhomogeneity in the system - visible in the PL spectra result in a simultaneous reduction in both V_{oc} and J_{sc} (Figures 5.11 (f)). This reduction in the PV parameters reflects the increased role of defects and non-radiative channels as halide segregation progresses under high laser fluence at 295 K.

Although the degradation of the perovskite film makes it challenging to definitively assess hot carriers at high powers in ambient conditions, these data enable us to distinguish different regimes of operation under various conditions of photoexcitation intensity and temperature in the devices assessed. This provides some confidence in the conclusions presented, since regimes dominated by halide segregation and the known effects of photo-induced degradation of perovskites

[31] have been evaluated under conditions that are independent of the regime in which evidence of non-equilibrium carriers are clearly present. Furthermore this occurs or is dominant where $T \sim 100$ K.

In summary, in this Chapter evidence of hot carrier effects in double cation-triple halide perovskite - $FA_{0.8}Cs_{0.2}PbI_{2.4}Br_{0.6}Cl_{0.02}$ solar cells is comprehensively assessed and presented using a suite of complementary experimental techniques.

Simultaneous evidence of hot carriers is presented in these devices in both PL and J-V measurements at a range of temperatures, and are especially evident at 100 K, when parasitic barriers to carrier extraction are evident and the effects of phonons are minimized. These experiments enable for example - halide segregation or device degradation under high light exposure to be differentiated from non-equilibrium carrier dynamics. This study also reveals that the thermionic emission of hot carriers and therefore the presence of a non-equilibrium carrier distribution in the operation of perovskite solar cells are quite different from those seen with simple equilibrium heating of the structure. Specifically, in the presence of hot carriers, large unsaturated photocurrents are observed at high powers when the non-equilibrium carrier distribution exceeds the heterostructure barriers that control carrier transport and rectification in these solar cell architectures.

While these findings support earlier measurements indicating slowed hot carrier thermalization in perovskites and the presence of hot carrier effects in solar cell

operation, they do not (importantly) show increased power conversion efficiency or successful demonstration a hot carrier solar cell. Indeed, although hot carrier extraction is evident as an increase in photocurrent, these carriers cool down in the contacts resulting in a voltage (V_{oc}) determined by the perovskite absorber bandgap, rather than a selectively extracted hot carrier distribution.

5.3 References

1. H. Min, et al., "Perovskite solar cells with atomically coherent interlayers on SnO2 electrodes", Nature, vol. 598, no. 7881, pp. 444-450, 2021.

2. M. Jošt, et al., "Perovskite/CIGS Tandem Solar Cells: From Certified 24.2% toward 30% and Beyond", ACS Energy Letters, vol. 7, no. 4, pp. 1298-1307, 2022.

3. J. A. Christians, et al., "Tailored interfaces of unencapsulated perovskite solar cells for > 1,000 hour operational stability", Nature Energy, vol. 3, no. 1, pp. 68-74, 2018.

4. J. Tong, et al., "Carrier control in Sn–Pb perovskites via 2D cation engineering for all-perovskite tandem solar cells with improved efficiency and stability", Nature Energy, vol. 7, no. 7, pp. 642-651, 2022.

5. C.R. Brown, et al., "Potential of High-Stability Perovskite Solar Cells for Low-Intensity–Low-Temperature (LILT) Outer Planetary Space Missions", ACS Applied Energy Materials, vol. 2, no. 1, pp. 814-821, 2019.

6. J. Xu, et al., Triple-halide wide–band gap perovskites with suppressed phase segregation for efficient tandems. Science, 2020. 367(6482): p. 1097-1104.

7. K.A. Bush, et al., "Compositional Engineering for Efficient Wide Band Gap Perovskites with Improved Stability to Photoinduced Phase Segregation", ACS Energy Letters, vol. 3, no. 2, pp. 428-435, 2018.

8. A.J. Knight, et al., "Halide Segregation in Mixed-Halide Perovskites: Influence of A-Site Cations", ACS Energy Letters, vol. 6, no. 2, pp. 799-808, 2021.

9. L. E. Mundt, et al., "Mixing Matters: Nanoscale Heterogeneity and Stability in Metal Halide Perovskite Solar Cells", ACS Energy Letters, vol. 7, no. 1, pp. 471-480, 2022.

10. I. M. Pavlovetc, et al., "Suppressing Cation Migration in Triple-Cation Lead Halide Perovskites", ACS Energy Letters, vol. 5, no. 9, pp. 2802-2810, 2020.

11. H. Afshari, "Radiation tolerance, high temperature stability, and self-healing of triple halide perovskite solar cells", in 49th IEEE Photovoltaic Specialists Conference (PVSC 49), Philadelphia, 2022.

12. T.R. Hopper, et al., "Hot Carrier Dynamics in Perovskite Nanocrystal Solids: Role of the Cold Carriers, Nanoconfinement, and the Surface", Nano Letters, vol. 20, no. 4, pp. 2271-2278, 2020.

13. M. Righetto, et al., "Hot carriers perspective on the nature of traps in perovskites", Nature Communications, vol. 11, no. 1, pp. 2712, 2020.

14. Y. Yang, et al., "Observation of a hot-phonon bottleneck in lead-iodide perovskites", Nature Photonics, vol. 10, no. 1, pp. 53-59, 2016.

15. J.W.M. Lim, et al., "Spotlight on Hot Carriers in Halide Perovskite Luminescence", ACS Energy Letters, vol. 7, no. 2, pp. 749-756, 2022.

16. H.H. Fang, et al., "Long-lived hot-carrier light emission and large blue shift in formamidinium tin triiodide perovskites", Nature Communications, vol. 9, no. 1, p. 243, 2018.

17. M. Li, et al., "Slow Hot-Carrier Cooling in Halide Perovskites: Prospects for Hot-Carrier Solar Cells", Advanced Materials, vol. 31, no. 47, pp. 1802486, 2019.

18. S. Sourabh, et al., "Hot carrier redistribution, electron-phonon interaction, and their role in carrier relaxation in thin film metal-halide perovskites", Physical Review Materials, vol. 5, no. 9, 095402, 2021.

19. M.R. Filip, C. Verdi, and F. Giustino, "GW Band Structures and Carrier Effective Masses of CH3NH3PbI3 and Hypothetical Perovskites of the Type APbI3: A = NH4, PH4, AsH4, and SbH4", The Journal of Physical Chemistry C, vol. 119, no. 45, pp. 25209-25219, 2015.

20. D. Ghosh, et al., "Polarons in Halide Perovskites: A Perspective", The Journal of Physical Chemistry Letters, vol. 11, no. 9, pp. 3271-3286, 2020.

21. L.M. Herz, "Charge-Carrier Dynamics in Organic-Inorganic Metal Halide Perovskites", Annual Review of Physical Chemistry, vol. 67, no. 1, pp. 65-89, 2016.

22. A.R. Srimath Kandada and C. Silva, "Exciton Polarons in Two-Dimensional Hybrid Metal-Halide Perovskites", The Journal of Physical Chemistry Letters, vol. 11, no. 9, pp. 3173-3184, 2020.

23. V. D'Innocenzo, et al., "Excitons versus free charges in organo-lead tri-halide perovskites", Nature Communications, vol. 5, no. 1, p. 3586, 2014.

24. H. Esmaielpour, et al., "Enhanced hot electron lifetimes in quantum wells with inhibited phonon coupling", Scientific Reports, vol. 8, no. 1, pp. 12473, 2018.

25. A.D. Wright, et al., "Electron–phonon coupling in hybrid lead halide perovskites", Nature Communications, vol. 7, no. 1, pp. 11755, 2016.

26. X. Chen, et al., "Excitonic Effects in Methylammonium Lead Halide Perovskites", The Journal of Physical Chemistry Letters, vol. 9, no. 10, pp. 2595-2603, 2018.

27. R. Saive, "S-Shaped Current–Voltage Characteristics in Solar Cells: A Review", IEEE Journal of Photovoltaics, vol. 9, no. 6, pp. 1477-1484, 2019.

28. J. Werner, et al., "Improving Low-Bandgap Tin–Lead Perovskite Solar Cells via Contact Engineering and Gas Quench Processing", ACS Energy Letters, vol. 5, no. 4, pp. 1215-1223, 2020.

29. H. Afshari, "Temperature Dependent Carrier Extraction and the Effects of Excitons on Emission and Photovoltaic Performance in CsFAMAPbIBr", ACS Applied Materials and Interfaces, 2022.

30. M. Baranowski and P. Plochocka, "Excitons in Metal-Halide Perovskites", Advanced Energy Materials, vol. 10, no. 26, p. 1903659, 2020.

31. N. Phung, et al., "Photoprotection in metal halide perovskites by ionic defect formation", Joule, 2022.

32. D.-T. Nguyen, et al., "Quantitative experimental assessment of hot carrier-enhanced solar cells at room temperature", Nature Energy, vol. 3, no. 3, pp. 236-242, 2018.

33. H. P. Piyathilaka, et al., "Hot-carrier dynamics in InAs/AlAsSb multiple-quantum wells", Scientific Reports, vol. 11, no. 1, pp. 10483, 2021.

34. H.L. Jean Rodière, Amaury Delamarre, Arthur Le Bris, Sana Laribi, et al., "Hot Carrier Solar Cell: From Simulation to Devices", in 27th European Photovoltaic Solar Energy Conference and Exhibition (EU PVSEC 2012), Frankfurt, Germany, 2012, p. 89.

35. Z. Jehl, et al., "Hot Carrier Extraction Using Energy Selective Contacts and Feedback On The Remaining Distribution", in 2018 IEEE 7th World Conference on Photovoltaic Energy Conversion (WCPEC) (A Joint Conference of 45th IEEE PVSC, 28th PVSEC 34th EU PVSEC), 2018.

36. S. S. Lim, et al., "Hot carrier extraction in CH3NH3PbI3 unveiled by pump-push-probe spectroscopy", Science Advances, vol. 5, no. 11, p. eaax3620.

37. H. Esmaielpour, et al., "Impact of excitation energy on hot carrier properties in InGaAs multi-quantum well structure", Progress in Photovoltaics: Research and Applications, 2022.

38. J.W.M. Lim, et al., "Hot Carriers in Halide Perovskites: How Hot Truly?", The Journal of Physical Chemistry Letters, vol. 11, no. 7, pp. 2743-2750, 2020.

39. H. Esmaielpour, et al., "Effect of occupation of the excited states and phonon broadening on the determination of the hot carrier temperature from continuous wave photoluminescence in InGaAsP quantum well absorbers", Progress in Photovoltaics: Research and Applications, vol. 25, no. 9, pp. 782-790, 2017.

40. H. Esmaielpour, et al., "Hot carrier relaxation and inhibited thermalization in superlattice heterostructures: The potential for phonon management", Applied Physics Letters, vol. 118, no. 21, pp. 213902, 2021.

41. H. Esmaielpour, et al., "Investigation of the spatial distribution of hot carriers in quantum-well structures via hyperspectral luminescence imaging", Journal of Applied Physics, vol. 128, no. 16, 165704, 2020.

42. Z. Chen, et al., "Unified theory for light-induced halide segregation in mixed halide perovskites", Nature Communications, vol. 12, no. 1, p. 2687, 2021.

43. M. C. Brennan, et al., "Light-Induced Anion Phase Segregation in Mixed Halide Perovskites", ACS Energy Letters, vol. 3, no. 1, pp. 204-213, 2018.

44. J. Cho and P.V. Kamat, "Photoinduced Phase Segregation in Mixed Halide Perovskites: Thermodynamic and Kinetic Aspects of Cl–Br Segregation", Advanced Optical Materials, vol. 9, no. 18, article no. 2001440, 2021.

45. S. Meloni, et al., "Ionic polarization-induced current–voltage hysteresis in CH3NH3PbX3 perovskite solar cells", Nature Communications, vol. 7, no. 1, pp. 10334, 2016.

46. C. Eames, et al., "Ionic transport in hybrid lead iodide perovskite solar cells", Nature Communications, vol. 6, no. 1, p. 7497, 2015.

47. J. A. R. Dimmock, et al., "A metallic hot-carrier photovoltaic device", Semiconductor Science and Technology, vol. 34, no. 6, 064001, 2019.

48. R.T. Ross and A.J. Nozik, "Efficiency of hot-carrier solar energy converters", Journal of Applied Physics, vol. 53, no. 5, pp. 3813-3818, 1982.

49. K.F. David, R.W. Vincent, and R.S. Ian, "Pathways to hot carrier solar cells", Journal of Photonics for Energy, vol. 12, no. 2, 022204, 2022.

50. S.P. Dunfield, et al., "From Defects to Degradation: A Mechanistic Understanding of Degradation in Perovskite Solar Cell Devices and Modules", Advanced Energy Materials, vol. 10, no. 26, p. 1904054, 2020.

51. Luis K. Ono, Emilio J. Juarez-Perez, and Yabing Qi ACS Applied Materials Interfaces 2017 9 (36), 30197-30246 DOI: 10.1021/acsami.7b06001.

52. D.K. Ferry, "Hot Carriers in Semiconductors", IOP Publishing, 2021.

53. Y. Takeda, T. Ito, T. Motohiro, D. König, S. Shrestha, and G. Conibeer, "Hot carrier solar cells operating under practical conditions", Journal of Applied Physics, vol. 105, no. 7, 074905, 2009. https://doi.org/10.1063/1.3086447.

54. D. K. Ferry, S. M. Goodnick, V. R. Whiteside, and I. R. Sellers , "Challenges, myths, and opportunities in hot carrier solar cells", Journal of Applied Physics 128, 220903 (2020) https://doi.org/10.1063/5.0028981.

55. S. Sourabh, H. Afshari, V. R. Whiteside, and M.C. Beard, I. R. Sellers " Evidence of Hot Carrier Extraction in Metal Halide Perovskite Solar Cells ", Physical Review X (under review).

56. K. Galkowski, et al., "Determination of the exciton binding energy and effective masses for methylammonium and formamidinium lead tri-halide perovskite semiconductors", Energy & Environmental Science, vol. 9, no. 3, pp. 962-970, 2016.

57. M. Hugues, B. Damilano, J-Y. Duboz, and J. Massies, "Exciton dissociation and hole escape in the thermal photoluminescence quenching of (Ga, In)(N, As) quantum wells", Physical Review B, vol. 75, no. 11, 115337, 2007.

Chapter 6

Dark Exciton Carrier Dynamics and Super Long Lived High Energy States in $(EPEA)_2PbI_4$

6.1 Introduction

Two-dimensional (2D) layered metal halide perovskites continue to attract considerable attention in the field of optoelectronics due to their unique structural, chemical and photophysical properties, which allow their consideration for a number of practical applications [2-12,18]. Unlike traditional 3D metal halide perovskites, 2D Ruddlesden popper perovskites demonstrate a much larger selection of organic cations due to their relaxation of structural constraints (e.g., as dictated by the structural tolerance factor) [32], For 2D Ruddlesden popper films, the tolerance criteria is not required and this allows for a wide range of selection of cations. Also, their crystal structures feature alternating sheets of organic cationic and inorganic anionic layers. This layered structure gives these materials a range of useful properties, including high carrier mobility, tunable band gaps, and strong light-matter interactions. [33]

In recent years, there has been growing interest in developing and optimizing these so called 2D Ruddlesden-Popper systems for use in a variety of optoelectronic devices, such as solar cells [9,10], LED's [8], and photodetectors [27]. A key area of research in this field has been the study of the material parameters that

influence the luminescence efficiency of these materials. By understanding how these parameters affect the photoluminescence (PL) and excitonic properties of 2D perovskites, new strategies may be developed for improving their performance in optoelectronic devices.

A 2D perovskite that has inspired particular interest is the n=1 2D Ruddlesden-Popper lead halide perovskites based on the ethylenediammonium cation, denoted as $(EPEA)_2PbI_4$ when incorporated into a lead halide system. This perovskite is a derivative of the parent material, phenethylammonium Lead Iodide ($PEAPbI_4$), which has been studied extensively [19] and is therefore considered as prototype 2D material [19]. Notably, due to its longer cation chain, $(EPEA)_2PbI_4$ has been shown to exhibit improved stability compared to $PEAPbI_4$ [28]. Since, $(EPEA)_2PbI_4$ shares similar optical properties with $PEAPbI_4$, including a high absorption coefficient, it is a promising candidate for a range of optoelectronic applications where improved stability is preferential.

The well-studied Ruddlesden-Popper perovskite $PEAPbI_4$, has been shown by several groups to exhibit long lived dark excitonic states [13-15,29-31] that have a number of interesting properties. Here, it will be shown that the signatures of such dark states also exist in $(EPEA)_2PbI_4$. These states, which are typically considered detrimental to the device performance, may have potential uses in applications in optoelectronic devices since these dark states act as a reservoir for the excited state population [1]. Understanding the fundamental physics of these

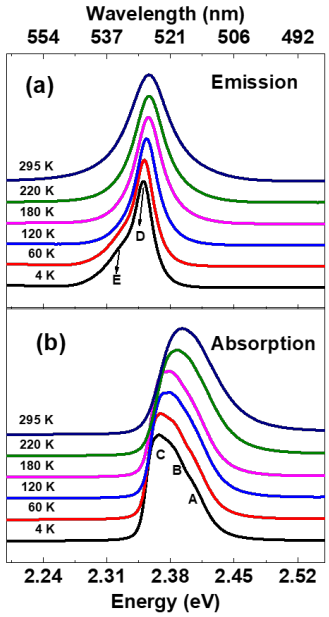


Figure 6.1: Normalized waterfall plot showing (a) the temperature-dependent photoluminescence (PL) emission and (b) absorption spectra for different temperatures, with all the features labeled properly. Features A and B in the absorption spectrum correspond to super long-lived dark energy states, C corresponds to bandgap absorption, while the 'D' in the PL spectrum corresponds to excitonic emission, and E possibly indicates a defect state.

dark excitonic states and how they may be manipulated also has the potential to enable the development of more efficient and effective optoelectronic devices if these states can be circumvented.

In this Chapter evidence for the existence of dark states in $(EPEA)_2PbI_4$ will be presented, and their dynamics evaluated using various optical spectroscopy techniques. These results - experiments offer new insights into the fundamental

physics of $(EPEA)_2PbI_4$.

6.2 Experimental Results and Analysis

Figure 6.1 presents the temperature-dependent PL (TD PL - solid lines) and absorption spectra (dashed lines) of an $(EPEA)_2PbI_4$ between 4 K and 295 K. The temperature-dependent absorption clearly exhibits a blueshift of the bandgap with increasing temperature, as expected [26]. In addition, the absorption spectra also exhibits multiple features at all temperatures. Two distinct features are evident on the high energy side of the CW absorption spectra located at $\sim$ 509 nm (A) and 515 nm (B), in addition to the main peak at 523 nm (C). While the TD PL (Figure 6.1a) does not exhibit any signature of a structural phase transition in the temperature range studied, the low-temperature PL ($T < 100$ K) shows additional features at lower energy (LBE) that are likely related to defects. These are extrinsic in nature, and weaken and disappear at higher temperatures ($T > 100$ K). This is attributed to thermal redistribution of carriers localized in these states that occupies the continuum states at higher temperature [17,20,21].

As expected, with increasing temperature the PL also shows a blueshift (Figure 6.2 - black open circles). At $T > 260$ K the peak energy of the PL also decreases further due to the strong electron-phonon coupling that is mediated by the ionization of excitons at higher temperatures and the formation of polarons in these systems [1,17,22-26]. The formation of polarons is further demonstrated by

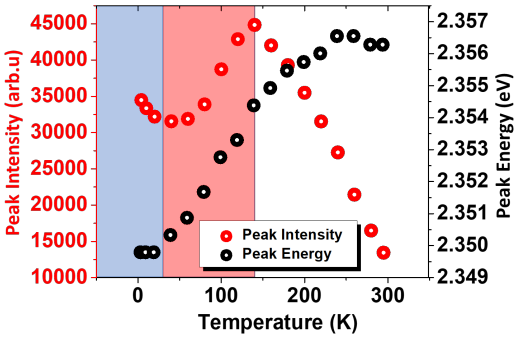


Figure 6.2: Peak intensity (open red circles) and peak energy (open black circles) extracted from temperature-dependent photoluminescence (PL) of the sample. The blue region corresponds to temperatures below 30 K, where the intensity decreases with increasing temperature due to the effect of a low-energy dark exciton. The red region corresponds to temperatures above 30 K, where thermal energy activates non-radiative channels that transfer charge to main excitonic state (radiative), which increases the integrated PL intensity. The white region corresponds to temperatures above 130 K, where the intensity decreases due to increasing electron-phonon coupling.

the clear increase in energy of the absorption and emission spectra (Stokes shift) with increasing temperature in Figure 6.1. This increase in the Stokes shift [34] is well studied in the perovskites, and is intimately related to the soft and dynamic nature of the lattice and polaron formation under photoexcitation [35] in these materials, including $PEAPbI_4$ [11,12,16].

Figure 6.2 shows the peak intensity (red open circles) and peak energy (black

open circles) of the PL as a function of temperature. The general peak profile of the PL appears typical of Ruddlesden Popper systems [1,17]. However, on closer inspection, the peak intensity exhibits three regions of variation with increasing temperature.

The first region, shown in blue in Figure 6.2, corresponds to $T < 30$ K. In this regime, the peak PL intensity decreases with increasing temperature. This behavior has been associated with the formation of a low-energy dark exciton, which is non-radiative in nature [17]. The reduced intensity between 4 K $< T >$ 30 K is initially consistent with a constant peak energy, before the PL energy begins to increase and the intensity reaches a minima at $T \sim 30$ K. This behavior suggests that the decrease in intensity at $T < 30$ K is due to a decrease in the probability of radiative recombination [1,17], and/or the redistribution of carriers to less localized states in the system as has been observed in several systems in which materials inhomogeneities are present [36-38].

In the second regime, between 30 K $< T >$ 130 K, shown as the red shaded region in Figure 6.2, k_BT is sufficient to ionize carriers trapped in localized states and defects, such that charges are redistributed into the continuum states in the system, which is then dominated by intrinsic excitons due to the extremely high binding energies that result in these materials due to their 2D nature [35]. As such the peak PL intensity increases (Figure 6.2 - open red circles).

The third region, shown in white in Figure 6.2, corresponds to $T > 130$ K. In this region, the intensity decreases with increasing temperature. This behavior is typical of lead halide perovskites (and semiconductors, in general) and is due to increasing electron- phonon coupling and the activation of non-radiative processes at higher temperatures [22-25].

To further probe the nature and behavior of the carrier dynamics across the regimes described in Figure 6.1 power-dependent transient absorption spectroscopy TA was performed. TA provides more detailed information about the photogenerated carriers and excited state dynamics of a system. By measuring the absorption of a probe pulse as a function of time, it is possible to infer the rate at which carriers redistribute amongst the states and insights into the energy transfer pathways within the sample.

Here, a Helios system that incorporated an ultrafast femtosecond transient absorption spectrometer was employed. For excitation, the 442 nm output from OPA (2 KHz, Apollo- Y, Ultrafast systems) was used as the pump beam, while a broadband source was used as probe. All measurements were performed at room temperature as a function of peak power density ranging from $\sim 10^6 \mu W/cm^2$ (corresponding to 7 μW power) to $\sim 10^7 \mu W/cm^2$ (60 μW). Power notation of (7 μW) and (60 μW) will be used in this Chapter for easy reference from here on.

Figure 6.3 (a) presents a comparison of the normalized PL at 4 K (red) with the continuous wave absorption (ABS - black) at room temperature. Figure 6.3

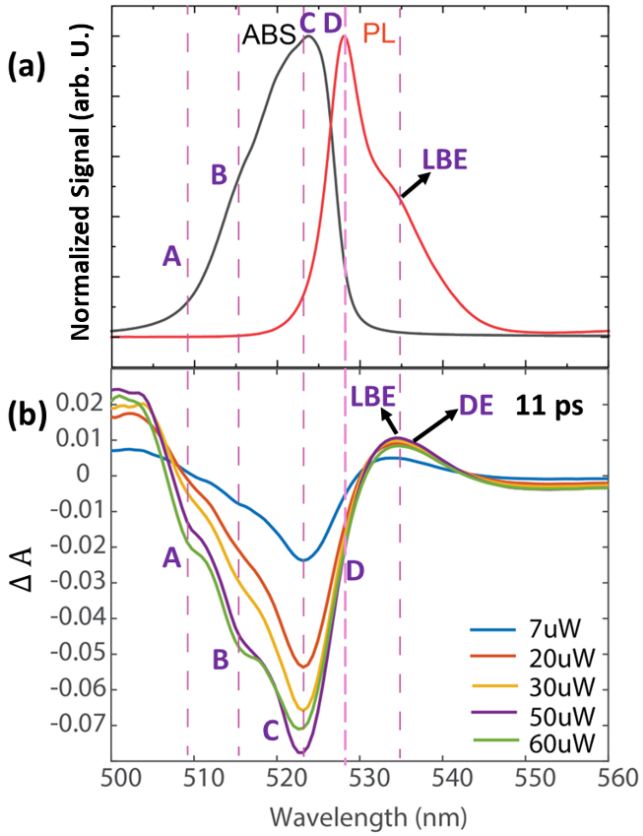


Figure 6.3: (a) Absorption (295 K) and PL spectra (4 K) are compared with the observed features (labeled) seen in TA shown in the lower panel (b). TA spectra (295 K) are presented for 11 ps and different powers (7 μW - 60 μW).

(b) shows TA probed as a function of average excitation powers at $t = 11$ ps, following the excitation (the pump). The features observed in the PL, absorption and TA are shown using the dotted lines for alphabetical labels (A-E).

The PL at 4 K exhibits two features at $\sim$ 528 nm (D) and $\sim$ 533 nm (LBE). The peak at 528 nm (D) is attributed to the intrinsic excitonic peak, while the feature at 533 nm (LBE) is attributed to a localized or defective state, which

is ionized at the higher temperatures. A comparison of the peaks observed in the high-power TA with those evident in the CW PL and ABS (Figure 6.3(a)) allows for the energy and nature of these features to be reconciled and their dynamics assessed and correlated. If the low energy peak at $\sim$ 533 nm (LBE) in the PL in Figure 6.3 (a) is first considered, there is good correspondence to the photo-induced absorption (PIA) feature at the same energy in the TA (Figure 6.3 (b)). This indicates the radiative nature of this defect-related feature and also suggests the presence of a dark state (DE in Figure 6.4), which transfers charge to a nearly degenerate bright state (LBE in Figure 6.4). The nature of this state is not well understood and needs further investigation but is supported by the data, as discussed below. Since, these features have been observed in $PEAPbI_4$ [M], we are more interested in the new features, which are very long lived and appear on the high energy side of the CW and TA absorption in $(EPEA)_2PbI_4$. These are reported here for the first time and are crucial to understanding the dynamics of these soft materials for practical applications.

Figure 6.3 (a) shows the ground state of the intrinsic exciton for $(EPEA)_2PbI_4$ (D at $\sim$ 528 nm) in the PL positioned at the onset of the CW absorption ($\sim$ 523 nm (C)). As shown in Figure 6.3, the absorption peak (Figure 6.3 (a) - C) matches the ground state bleach in TA (Figure 6.3 (b)) shown by the dotted line; however, additional features are also observed in the high-energy tail of the CW absorption that match states also observed in the TA (Figure 6.3 (a) – A,B). A and B are more clearly resolved with increasing power, and time delay (Figure 6.5

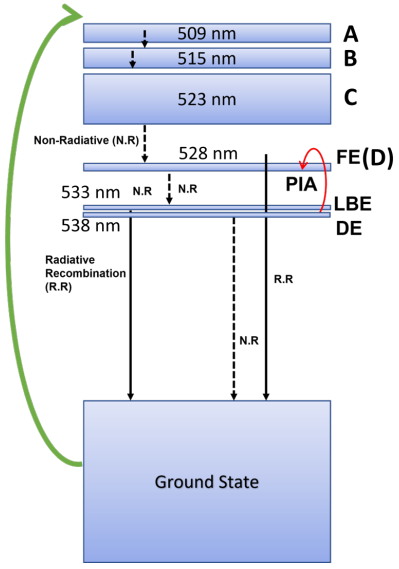


Figure 6.4: The proposed photophysical model effectively describes the results obtained from photoluminescence, absorption, and ultrafast TA measurements. The model includes both radiative (solid lines) and non-radiative pathways (dotted lines), with the activation of charge transfer confirmed by changes in the photoluminescence integrated intensity beyond a certain temperature. This model provides a comprehensive understanding of the photophysical behavior of the system under investigation.

and discussed below). At shorter time delays (or lower powers) the two features A at $\sim$ 509 nm and B at $\sim$ 515 nm are less evident, and are screened by the dominant ground state bleach (C) at $\sim$ 523 nm. As the ground state bleach weakens ('C' in Figure 6.3 (b)), the features A and B become more prevalent. Since these features (A and B) are at higher energy, they are not evident in CW PL. Furthermore, these states are very long-lived as evidenced by the TA signal accumulation before $t = 0$ (Figure 6.5), and there dominance of the TA at very

long times (> 0.5 ms in TA - Figure 6.5). The long lived nature of these states supports their non-radiative nature.

A photophysical model is now presented to qualitatively describe the behavior of $(EPEA)_2PbI_4$ material under photoexcitation. This is shown in Figure 6.4. When the sample is excited at 442 nm, it generates charge carriers that are absorbed into the high energy states A and B. These high-energy states are responsible for the CW absorption, which is shown at 523 nm and corresponds to the material's bandgap.

This model also accounts for the presence of the multiple exciton states, including the excitonic state (FE) that is evident in the photoluminescence (PL) spectra. Additionally, the model considers the presence of two other states; the dark state (DE) and a lower energy bright state (LBE), both at the energy E (Figure 6.3), and their characteristics. Both states are very closely spaced and has been resolved and shown later in Figure 6.7.

The solid lines (Figure 6.4) in the model represent radiative transitions, while the dotted lines indicate the decay from non-radiative pathways. The up arrow (↑) represents absorption, and the curved arrow shows the charge transfer from DE to FE (D), which are activated at $T > 30$ K, and result in an increase in the PL intensity.

The model (Figure 6.4) assumes that the charge transfer from FE (D) to DE is slower compared to the back transfer (DE ← to FE (D)), resulting in an overall charge transfer from DE to FE (D) that enables the increase in the PL intensity. The model also considers the thermalization or relaxation of charge carriers with time. This photophysical model provides a qualitative analysis of the transitions observed in TA (Figure 6.3 (b)) and PL spectra (Figure 6.3 (a)) for $(EPEA)_2PbI_4$.

In Figure 6.5 heat maps for 7 μW and 60 μW power measurements are presented. Figure 6.5 represents the heat map of the TA at for 7 μW (b) & at 60 μW (a), where the X-axis represents wavelength, Y-axis represents the time delay of the probe pulse and Z, the Intensity (magnitude) of the transitions, also shown as a color gradient to the left of figure (a) and (b). Figure 6.5 (c) and (d) shows the time slices of the 3D heat map taken from a and b for both these powers. These time frames are chosen as they sufficiently show the evolution of the transitions. The high energy features (A and B - observed in Figure 6.3) are more evident at high power (Fig 6.5 (a,b)) as the illustrated by the color regions indicated on the heat map. These states appear to accumulate prior to t = 0, indicating their lifetime is comparable to the time interval between excitation pulses ($\sim$ 0.5 ms). The bleaching of these transitions (A and B) and their increase in strength with increasing excitation indicates the activation of these states is strongly related to photoexcitation and the likely – in these soft materials causes perturbation or polarization of the lattice. Here, considering the initial analysis, one possible explanation could be that the properties of these states (A and B) results from

crystal deformation resulting in self-trapping when high-pump powers are applied and large carrier densities interact with the lattice, an effect known to change the dielectric properties of these systems [**39**].

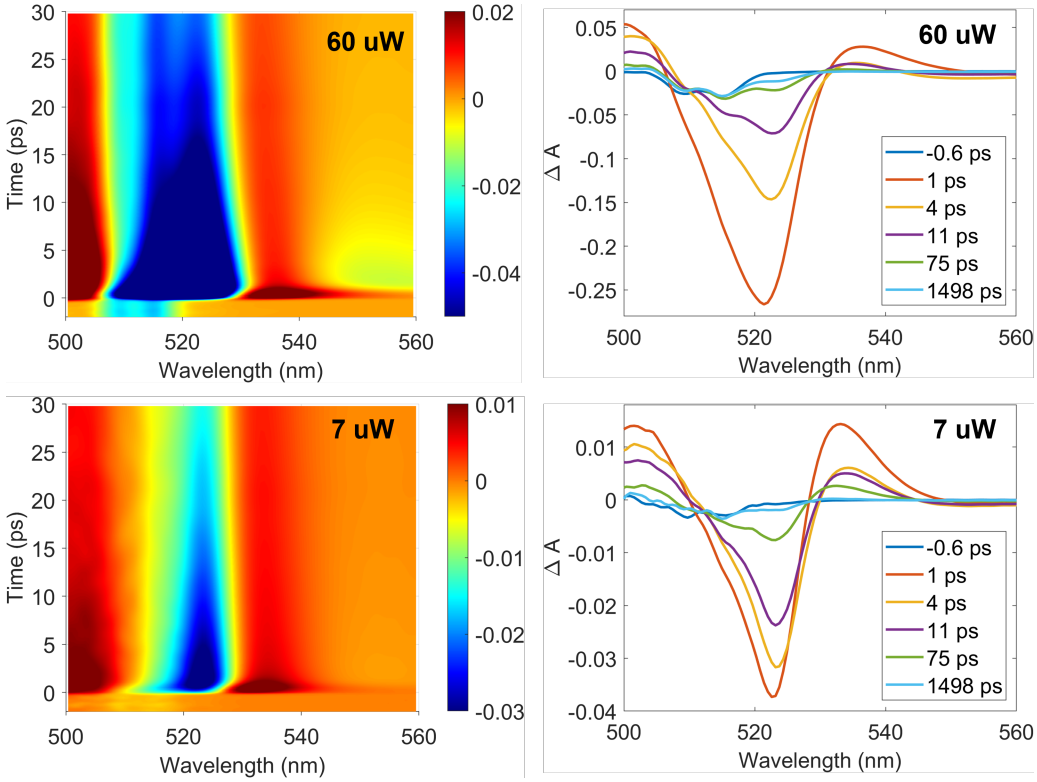


Figure 6.5: Heat map of transient spectra at low power (7 μW) and high power (60 μW) along with their respective transient spectra at different delay times.

At high powers, the features A and B that are attributed to dark states are evident at relatively short time delays ($t \sim <$ 11 ps in Figure 6.5 (b)), which is not the case at lower power (Figure 6.5 (d)). This is likely due to the fact that at higher excitation power, the density of non-radiative centers in the system increases. Indeed, at higher fluences photo degradation is a well known phenomena

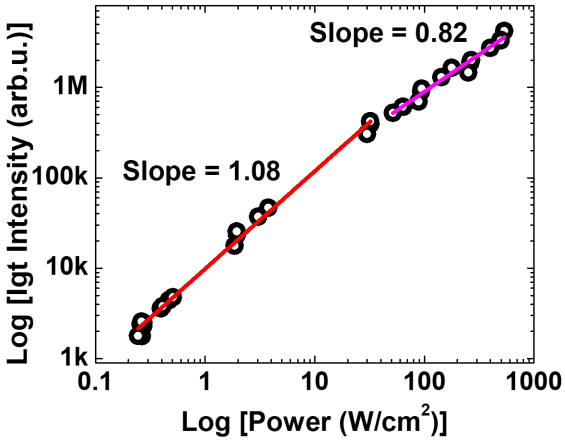


Figure 6.6: The absorption (295 K) and photoluminescence spectra for 4 K, which are used to compare with the observed effects in transient absorption shown in the lower panel. The transient absorption (TA) spectra are presented for 11 ps and different powers.

in the perovskites [40]. This is also supported by the CW power-dependent PL measurements, which show the existence of two distinct transition regions with different power law dependencies, providing evidence for this hypothesis. Figure 6.6 presents the integrated intensity extracted from the power-dependent PL measurements on a logarithmic scale. The data is fit using the power law expression: $I_{PL} = I^{\gamma}$, where I_{PL} represents the PL intensity, and I is the pump fluence. It is noteworthy that as the excitation power density increases, γ decreases from ~ 1 to < 1. A γ value < 1 suggests reduced PL yield, which indicates the prevalence of non-radiative processes [1]. Although the possibility of the Auger process is not discounted here, the presence of features - (A) and (B) in TA suggest the formation of non-radiative recombination centers at higher fluences. Consequently,

we conclude that as the excitation power density increases, the system exhibits an increasing density of non-radiative centers.

As previously discussed (and shown in Figure 6.3), there are two closely spaced

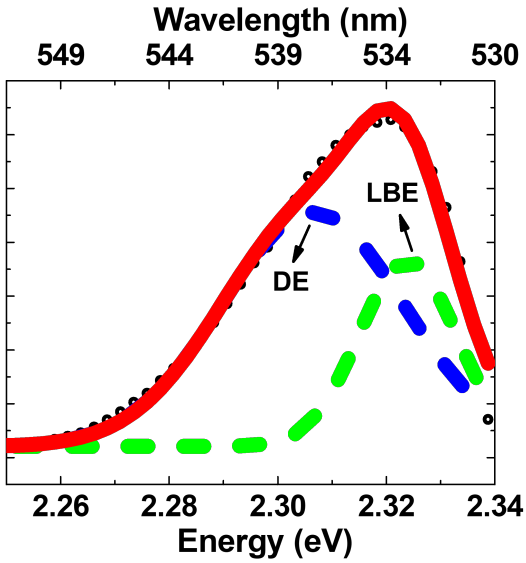


Figure 6.7: Peak fitting analysis using Gaussian distribution for the photoinduced absorption (PIA) of transient absorption (TA) spectra, recorded at 11 ps time under an irradiance of 60 μW (10^7 mW/cm^2). Y-axis is arbitrary positive ΔA. The fitting shows the presence of two distinct peaks at $\sim$ 533 nm (green)(LBE) and $\sim$ 538 nm (blue)(DE). The peak at 533 nm (LBE) is also detected in the photoluminescence (PL) spectrum. The PIA data suggests the existence of two closely spaced peaks.

defect peaks evident in $(EPEA)_2PbI_4$, one bright (LBE) and one dark (DE), located at $\sim$ 533 nm and $\sim$ 538 nm respectively (Figure 6.3 (b)). The origin of these transitions is further supported by the non-Gaussian nature of the PIA, and the convolution of these closely spaced peaks in Figure 6.7. The PIA, supports the

presence of two peaks possibly associated with dark and bright state. Consistent with the analysis reported by Folpini et al. [1].

6.3 Discussion and Conclusion

Here, the presence of DE and LBE states with energy lower than the main excitonic transition (FE) at 528 nm (feature E) is proposed through the analysis of temperature-dependent PL and the TA dynamics. This is consistent with previous research on the related PEA-metal halide, which reported the presence of such dark states [1]. In the system studied in this chapter ($(EPEA)_2PbI_4$), two degenerate or closely spaced states are identified: one dark (DE - non-radiative) and one bright (LBE - radiative) below the main excitonic peak (FE). Though it is deduced here, the exact origin of such states are not yet fully understood and requires further investigation. The DE dominates at $T < 30$ K, while the charge is thermally redistributed to the LBE and FE states $T > 30$ K. Upon free carrier generation and absorption into high-energy states upon photoexcitation, a ground-state bleaching is evident in the TA. The bleach of the TA also displays structure in the form of three energetic transitions at (C) $\sim$ 523 nm, (B) at $\sim$ 515 nm, and (A) at $\sim$ 509 nm. A comparison of the TD PL and TA indicates that (C) at $\sim$ 523 nm is radiative, while the long-lived nature of (A) and (B) indicates they are non-radiative, or dark states.

The TA also shows evidence of two additional long-lived excited states (A) and (B) in the sample at higher powers. A possible scenario is that these states are created due to the interaction of the lattice with the high energy & dense carrier population at high applied pump power. The appearance of these states (A and B) before $t = 0$, (i.e., before the probe pulse arrives) and their enhancement with increasing power, further supports that they are generated by light and crystal interaction. These states are shown in the model introduced in Figure 6.4.

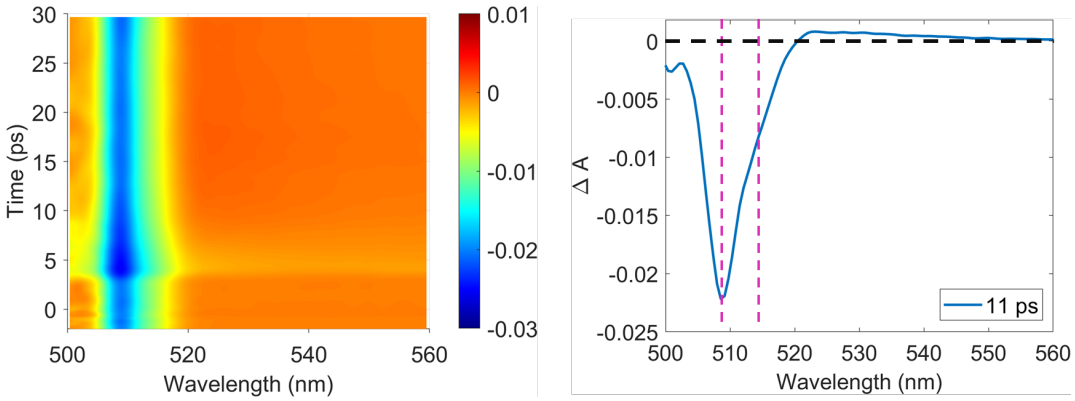


Figure 6.8: Heat map (left) of the $(EPEA)_2PbI_4$ and the transient absorption spectra (right) at 11 ps, measured again after 6 months.

Figure 6.8 shows the TA spectrum of at $t = 11$ ps measured after 6 months under N_2 storage. The excitonic bleach and the PIA feature are no longer visible in these spectra (see Fig 6.5 for a comparison of the pristine samples under the same conditions). This measurements that was excited at a low pump power ($\sim$ 10 μW) is now dominated by the two long-live features previously attributed to dark states in Figure 6.3 (labels (A) and (B)), which were previously *only* evident at high pumping powers (Figure 6.5 (a)). This analysis provides some insight

with respect to the degradation of these EPEA- 2D perovskites, which appears ultimately related to dark states, the origin of which requires more investigation but is likely due to some sort of extrinsic defect that are only lower in density or less dominant in pristine samples (transitions - (A) and (B) in Figure 6.3). However, these complexes provide degradation paths and decrease stability in these systems. This eventually leads to the loss of the radiative properties of the samples over time via exposure to external perturbations such as environmental conditions and/or thermal cycling, and as is evident here at high power optical excitation.

In conclusion, the 2D Ruddlesden Popper perovskite $(EPEA)_2PbI_4$ was investigated using temperature dependent & power dependent PL and TA spectroscopy. This analysis revealed the presence of multiple excitonic complexes in these materials, with signatures of carrier redistribution mediated by power and/or temperature, and the presence of extremely long-lived dark states in TA. Some of these dark transitions ('DE') have been observed by others in related systems [1] while the very long-lived dark states (A & B) are reported here for the first time in $(EPEA)_2PbI_4$. These states appear to be intimately involved in the nature and dynamics of the PL and absorption in $(EPEA)_2PbI_4$.

6.4 References

1. G. Folpini, et al., The role of a dark exciton reservoir in the luminescence efficiency of two-dimensional tin iodide perovskites. Journal of Materials Chemistry C, 2020. 8(31): p. 10889-10896.

2. B. R. Sutherland and E. H. Sargent, Nat. Photonics, 2016, 10, 295.

3. J. Luo, X. Wang, S. Li, J. Liu, Y. Guo, G. Niu, L. Yao, Y. Fu, L. Gao, Q. Dong, C. Zhao, M. Leng, F. Ma, W. Liang, L. Wang, S. Jin, J. Han, L. Zhang, J. Etheridge, J. Wang, Y. Yan, E. H. Sargent and J. Tang, Nature, 2018, 563, 541.

4. B. Zhao, S. Bai, V. Kim, R. Lamboll, R. Shivanna, F. Auras, J. M. Richter, L. Yang, L. Dai, M. Alsari, X. J. She, L. Liang, J. Zhang, S. Lilliu, P. Gao, H. J. Snaith, J. Wang, N. C. Greenham, R. H. Friend and D. Di, Nat. Photonics, 2018, 12, 783.

5. L. Gao, L. N. Quan, F. P. Garcı´a de Arquer, Y. Zhao, R. Munir, A. Proppe, R. Quintero-Bermudez, C. Zou, Z. Yang, M. I. Saidaminov, O. Voznyy, S. Kinge, Z. Lu, S. O. Kelley, A. Amassian, J. Tang and E. H. Sargent, Nat. Photonics, 2020, 14, 227–233.

6. H. Zhang, Y. Wu, Q. Liao, Z. Zhang, Y. Liu, Q. Gao, P. Liu, M. Li, J. Yao and H. Fu, Angew. Chem., 2018, 130, 7874.

7. M. Yuan, L. N. Quan, R. Comin, G. Walters, R. Sabatini, O. Voznyy, S.

Hoogland, Y. Zhao, E. M. Beauregard, P. Kanjanaboos, Z. Lu, D. H. Kim and E. H. Sargent, Nat. Nanotechnol., 2016, 11, 872.

8. L. Cheng, T. Jiang, Y. Cao, C. Yi, N. Wang, W. Huang and J. Wang, Adv. Mater., 2019, 1904163, 1.

9. G. Grancini and M. K. Nazeeruddin, Nat. Rev. Mater., 2019, 4, 4–22.

10. K. T. Cho, G. Grancini, Y. Lee, E. Oveisi, J. Ryu, O. Almora, M. Tschumi, P. A. Schouwink, G. Seo, S. Heo, J. Park, J. Jang, S. Paek, G. Garcia-Belmonte and M. K. Nazeeruddin, Energy Environ. Sci., 2018, 11, 952.

11. A. R. S. Kandada and C. Silva, J. Phys. Chem. Lett., 2020, 11, 3173–3184.

12. S. Neutzner, F. Thouin, D. Cortecchia, A. Petrozza, C. Silva and A. R. Srimath Kandada, Phys. Rev. Mater., 2018, 2, 064605.

13. Z. Gan, X. Wen, C. Zhou, W. Chen, F. Zheng, S. Yang, J. A. Davis, P. C. Tapping, T. W. Kee, H. Zhang and B. Jia, Adv. Opt. Mater., 2019, 7, 1900971.

14. H.-H. Fang, J. Yang, S. Adjokatse, M. E. Kamminga, H. Duim, J. Ye, G. R. Blake, J. Even and M. A. Loi, Adv. Funct. Mater., 2020, 30, 1907979.

15. A. Liu, D. B. Almeida, L. G. Bonato, G. Nagamine, L. F. Zagonel, A. F. Nogueira, L. A. Padilha and S. T. Cundiff, 2020, arXiv:2002.08349 [cond-mat.mtrl-sci].

16. F. Thouin, A. R. Srimath Kandada, D. A. Valverde-Cha´vez, D. Cortecchia, I. Bargigia, A. Petrozza, X. Yang, E. R. Bittner and C. Silva, Chem. Mater., 2019, 31, 7085.

17. M. Kaiser, et al., How free exciton–exciton annihilation lets bound exciton emission dominate the photoluminescence of 2D-perovskites under high-fluence pulsed excitation at cryogenic temperatures. Journal of Applied Physics, 2021. 129(12): p. 123101.

18. F. Zhang, H. Lu, J. Tong, J. J. Berry, M. C. Beard, and K. Zhu, "Advances in two-dimensional organic–inorganic hybrid perovskites," Energy Environ. Sci. 13, 1154–1186 (2020).

19. G. Delport, G. Chehade, F. Lédée, H. Diab, C. Milesi-Brault, G. Trippé-Allard, J. Even, J.-S. Lauret, E. Deleporte, and D. Garrot, "Exciton–exciton annihilation in two-dimensional halide perovskites at room temperature," J. Phys. Chem. Lett. 10, 5153–5159 (2019).

20. N. Kitazawa, M. Aono, and Y. Watanabe, "Temperature-dependent timere-solved photoluminescence of (C6H5C2H4NH3)2PbX4 (X=Br and I)," Mater. Chem. Phys. 134, 875–880 (2012).

21. W. K. Chong, K. Thirumal, D. Giovanni, T. W. Goh, X. Liu, N. Mathews, S. Mhaisalkar, and T. C. Sum, "Dominant factors limiting the optical gain in layered two-dimensional halide perovskite thin films," Phys. Chem. Chem. Phys. 18, 14701–14708 (2016).

22. C. Yu, Z. Chen, J. J. Wang, W. Pfenninger, N. Vockic, J. T. Kenney, and K. Shum, "Temperature dependence of the band gap of perovskite semiconductor compound CsSnI3," J. Appl. Phys. 110, 063526 (2011).

23. S. Wang, J. Ma, W. Li, J. Wang, H. Wang, H. Shen, J. Li, J. Wang, H. Luo, and D. Li, "Temperature-dependent band gap in two-dimensional perovskites: Thermal expansion interaction and electron–phonon interaction," J. Phys. Chem. Lett. 10, 2546–2553 (2019).

24. K. Wei, Z. Xu, R. Chen, X. Zheng, X. Cheng, and T. Jiang, "Temperature dependent excitonic photoluminescence excited by two-photon absorption in perovskite CsPbBr3 quantum dots," Opt. Lett. 41, 3821–3824 (2016).

25. J. Bhosale, A. K. Ramdas, A. Burger, A. Muñoz, A. H. Romero, M. Cardona, R. Lauck, and R. K. Kremer, "Temperature dependence of band gaps in semiconductors: Electron-phonon interaction," Phys. Rev. B 86, 195208 (2012).

26. R. Prasanna, A. Gold-Parker, T. Leijtens, B. Conings, A. Babayigit, H.-G. Boyen, M. F. Toney, and M. D. McGehee, "Band gap tuning via lattice contraction and octahedral tilting in perovskite materials for photovoltaics," J. Am. Chem. Soc. 139, 11117–11124 (2017).

27. Z. Li, E. Hong, X. Zhang, M. Deng, and X. Fang, "The Journal of Physical Chemistry Letters", vol. 13, no. 5, pp. 1215-1225, 2022. DOI: 10.1021/acs.jpclett.1c04225.

28. D. B. Straus, N. Iotov, M. R. Gau, Q. Zhao, P. J. Carroll, and C. R. Kagan, "The Journal of Physical Chemistry Letters", vol. 10, no. 6, pp. 1198-1205, 2019. DOI: 10.1021/acs.jpclett.9b00247.

29. M. Fu, P. Tamarat, H. Huang, J. Even, A. L. Rogach, B. Lounis, Neutral and charged exciton fine structure in single lead halide perovskite nanocrystals revealed by magneto-optical spectroscopy. Nano Lett. 17, 2895–2901 (2017).

30. K. Tanaka, T. Takahashi, T. Kondo, K. Umeda, K. Ema, T. Umebayashi, K. Asai, K. Uchida, N. Miura, Electronic and excitonic structures of inorganic–organic perovskite-type quantum-well crystal (C4H9NH3)2PbBr4. Jpn. J. Appl. Phys. 44, 5923–5932 (2005).

31. Z. Yu, Effective-mass model and magneto-optical properties in hybrid perovskites. Sci. Rep. 6, 28576 (2016).

32. A. Ajayakumar, C. Muthu, A. V. Dev, J. K. Pious, and C. Vijayakumar, Two-Dimensional Halide Perovskites: Approaches to Improve Optoelectronic Properties. Chem Asian J. 2022 Jan 3;17(1):e202101075. doi: 10.1002/asia.202101075. Epub 2021 Nov 23. PMID: 34738734.

33. P.-P. Sun, et al., "High carrier mobility and remarkable photovoltaic performance of two-dimensional Ruddlesden–Popper organic–inorganic metal halides (PA)2(MA)2M3I10 for perovskite solar cell applications", Materials Today, vol. 47, pp. 45-52, 2021.

34. S. Sourabh, et al., "Hot carrier redistribution, electron-phonon interaction,

and their role in carrier relaxation in thin film metal-halide perovskites", Physical Review Materials, vol. 5, no. 9, 095402, 2021.

35. H. Esmaielpour, V. R. Whiteside, S. Sourabh, G. E. Eperon, J. T. Precht, M. C. Beard, H. Lu, B. K. Durant, and I. R. Sellers, J. Phys. Chem. C 124, 9496 (2020).

36. J. Tang, V. R. Whiteside, H. Esmaielpour, S. Vijeyaragunathan, T. D. Mishima, M. B. Santos, and I. R. Sellers , "Effects of localization on hot carriers in InAs/AlAsxSb1–x quantum wells", Appl. Phys. Lett. 106, 061902 (2015) https://doi.org/10.1063/1.4907630.

37. T. Mou, et al., "Role of In in Hydrogenation of N-Related Complexes in GaInNAs". ACS Applied Electronic Materials, 2019. 1(4): p. 461-466.

38. M. Leroux, N. Grandjean, B. Beaumont, G. Nataf, F. Semond, J. Massies, and P. Gibart , "Temperature quenching of photoluminescence intensities in undoped and doped GaN", Journal of Applied Physics 86, 3721-3728 (1999) https://doi.org/10.1063/1.371242.

39. M.J., Hong, et al., Time-Resolved Changes in Dielectric Constant of Metal Halide Perovskites under Illumination. Journal of the American Chemical Society, 2020. 142(47): p. 19799-19803.

40. Z. Chen, G. Brocks, S. Tao, et al., "Unified theory for light-induced halide segregation in mixed halide perovskites", Nat Commun, vol. 12, pp. 2687, 2021.

Chapter 7

Conclusion

7.1 Summary

This thesis significantly enhances our understanding of the fundamental interactions that drive carrier dynamics and hot carrier relaxation in metal halide perovskites for photovoltaic applications. The research presented employs a diverse array of experimental methods, such as temperature-dependent photoluminescence, power-dependent photoluminescence, continuous wave absorption spectroscopy, and ultrafast transient spectroscopy, to examine the behavior of charge carrier interactions and phenomena influencing the dynamics and relaxation of charge carriers in metal halide perovskites. The initial two chapters were dedicated to establishing the foundational concepts and familiarizing the reader with the content of the thesis.

The 3^{rd} and 4^{th} chapter of the thesis focused on hot carrier redistribution, carrier-carrier, and carrier-phonon interaction in metal halide perovskites. The results showed that the slow cooling of carriers in metal-halide perovskites shows little dependence of phonon energy, exciton binding energy, and interaction strength. This led to the proposal that the overall cooling of carriers is dominated by the intrinsic low thermal conductivity of all metal-halide perovskites, which limits the dissipation of acoustic phonons in these systems.

The 5^{th} chapter investigated the evidence of hot carriers in metal halide perovskite devices. The results showed that the competition between hot carrier dynamics and photoinduced halide segregation strongly depends on temperature. At low temperatures, clear evidence of hot carriers was observed via increasing carrier temperatures in the high-energy tail of the photoluminescence coupled with ballistic-like transport in current density-voltage measurements. At room temperature, the broadening of the PL makes it very difficult to observe hot carriers, but the J-V measurements indicate the presence of hot carriers at lower fluences. However, the photoinduced halide segregation begins to occur at higher lattice temperatures or at higher fluence, revealing the soft nature of these materials.

Finally, the 6^{th} chapter focuses on studying the optical properties of a new type of 2D Ruddlesden-Popper perovskite $(EPEA)_2PbI_4$ using temperature and power-dependent photoluminescence and transient absorption spectroscopy. The analysis of this study has shown the presence of multiple excitonic complexes and carrier redistribution mediated by power and/or temperature. Moreover, extremely long-lived dark states in transient absorption are observed, which play a significant role in the photoluminescence and absorption dynamics of $(EPEA)_2PbI_4$. These findings contribute to a deeper comprehension of perovskite materials, which continue to exhibit remarkable potential for optoelectronic applications.

7.2 Future Works

Building on the findings and experiments presented in Chapter 5, our future research plan is focused on the development of a hot carrier solar cell. To realize this goal, the device needs to be optimized, particularly in terms of energy-selective contacts. We intend to collaborate with Swift Solar to design and investigate a more efficient solar cell with an absorber layer thickness of 400 nm.

In addition to device optimization, addressing the issue of halide segregation in FACsPbIBrCl perovskite materials at room temperature is also crucial. Our research plan includes exploring strategies to mitigate photoinduced halide segregation, which will contribute to the development of more stable and efficient devices. By addressing these challenges, we hope to advance the field of hot carrier solar cells and contribute to the development of high-performance, stable, and cost-effective optoelectronic devices based on perovskite materials.

Another possible project is based on the system discussed in the 6th chapter, which focused on the optical properties of a new type of 2D Ruddlesden-Popper perovskite $(EPEA)_2PbI_4$, our future research plan involves collaborating with our partners at OSU to investigate the origins of the long-lived dark states observed in transient absorption. By conducting density functional theory (DFT) calculations, we aim to gain a deeper understanding of the photophysics of these materials.

Additionally, our research plan includes not only the study of this specific family of compounds but also an investigation into other perovskite materials to broaden our understanding of their photophysics. This approach will enable us to determine if the origin of these long-lived states can be attributed to organic cations or the inorganic cage of the perovskites and to ascertain whether this phenomenon is exclusive to one family of perovskites or observed more generally across various perovskite systems.

By following these research directions, we aim to enhance our understanding of perovskite materials and their distinct optical properties and gain insights into the implications of hot carrier temperature extraction from these systems.